ÉCOLE POLYTECHNIQUE

Laboratoire d'Hydrodynamique

Theoretical Modeling of Endothelial Cell Response to Mechanical Cues

Author:
Cécile GOUGET

Supervisor:
Abdul BARAKAT

A thesis submitted for the degree of
Docteur de l'École Polytechnique

Speciality: Mechanics

The defense will take place on the 15th October 2014 in front of:

Denis AUBRY	Rapporteur	École Centrale Paris, Châtenay-Malabry
Daniel ISABEY	Rapporteur	Institut Mondor de Recherche Biomédicale, Créteil
Chaouqi MISBAH	Examinateur	Université Joseph Fourier Grenoble I, Saint-Martin d'Hères
Cécile SYKES	Examinateur	Institut Curie, Paris
Abdul BARAKAT	Directeur de Thèse	École Polytechnique, Palaiseau

Abstract

Theoretical Modeling of Endothelial Cell Response to Mechanical Cues

In blood vessels, the endothelium, a thin monolayer of cells, lies at the interface between the bloodstream and the vascular wall. Dysfunction of endothelial cells is involved in major pathologies. For instance, atherosclerosis develops when the barrier and anti-inflammatory functions of the endothelium are impaired, allowing accumulation of cholesterol and other materials in the arterial wall. In cancer, a key step in the growth of a tumor is its vascularization, a process driven by endothelial cell migration. The mechanical environment of endothelial cells plays a key role in their function and dysfunction. Despite intense research in the field, how mechanotransduction, the conversion of a mechanical cue to a biological signal, occurs in endothelial cells is not completely understood. In this work, we integrate experimental knowledge into theoretical models at the subcellular, cellular and multicellular scales in order to enhance our understanding of endothalial cell mechanotransduction.

Actin stress fibers have been suggested as a good candidate to mediate rapid force transmission within a cell. To test this hypothesis, we develop a model of transmission of a mechanical signal within a cell by describing strains that develop in a network of stress fibers. We find force transmission dynamics consistent with experimental results. Besides, we show that stress fiber organization and external force characteristics play a key role in mechanical signal transmission. This link between the mechanical environment, the stress fiber network topology, and the cell perception of force provides a possible explanation for the colocalization between atherosclerotic lesions and disturbed flow regions, where the stress fiber network is randomly organized.

Endothelial cells are organized in a monolayer, and a further step needs to be taken to understand perception of force by a population of cells. Based on the observation that stress fiber networks of neighboring cells are connected and that this structure is key in cell mechanics, we model strain transmission in a monolayer network of stress fibers. Our results suggest that mimization of strain and of strain variations drives the topology of the stress fiber network. In particular, the isotropic topology typical of regions of disturbed flow protects the network from extreme variations in strain with perturbations in the flow. Our results also show that the strain is polarized in isotropic networks, which could be a mechanism to sense flow force direction.

In a final model, we study how mechanical cues drive the direction of cell migration, a key process in the formation of blood vessels. Cell migration occurs in three steps of protrusion, tension-dependent attachment to the matrix, and detachment of the weakest adhesions. We model the cell and the matrix as elastic materials coupled at the interface where the cell adheres to the matrix. Cell contractility is modeled by application of an active tensile stress at this interface. Adhesions are formed proportionally to the cell resistance to deformation, and then sequentially detached with a force-dependent probability. In agreement with experimental results, we find preferential migration in the direction of higher matrix stiffness. An obstacle in the matrix, such as another cell, is sensed by an increase in the resistance to deformation, so that the cell tends to migrate towards the obstacle. This shows that mechanical cues may be at stake in the formation of new blood vessels.

The models developed in the present work enhance our understanding of cellular mechanotransduction and provide insight into the role that mechanical forces play in the development and progression of atherosclerosis.

Résumé

Réponse des Cellules Endothéliales aux signaux mécaniques

Dans les vaisseaux sanguins, une monocouche de cellules, l'endothélium, est à l'interface entre le sang et la paroi vasculaire. Le dysfonctionnement des cellules endothéliales est impliqué dans des pathologies majeures. Par exemple, l'athérosclérose se développe quand l'endothélium ne remplit plus sa fonction de barrière et laisse passer et s'accumuler des matériaux comme le cholestérol. Un autre exemple est le développement des tumeurs, dont une étape importante est la vascularisation, un processus contrôlé par la migration des cellules endothéliales. L'environnement mécanique des cellules endothéliales joue un rôle majeur dans leur fonctionnement. Le processus de conversion des signaux mécaniques en signaux biologiques, appelé mécanotransduction, n'est cependant pas complètement compris. Dans ce travail, nous développons des modèles théoriques aux échelles subcellulaire, cellulaire, et multicellulaire qui intègrent les connaissances expérimentales.

Les filaments d'actine tendus par les myosines ont été proposés comme médiateurs de la transmission rapide de force à l'intérieur de la cellule. Pour tester cette hypothèse, nous développons un modèle de transmission du signal mécanique à travers un réseau de filaments d'actine. Les résultats montrent une dynamique de transmission cohérente avec les résultats expérimentaux. De plus, ils montrent que l'organisation des filaments et les caractéristiques de la force appliquée jouent un rôle déterminant dans la transmission de la force. Ces résultats expliquent en partie la colocalisation des lésions athérosclérotiques avec les régions d'écoulement perturbé où les filaments d'actine sont organisés de façon isotrope.

Les cellules endothéliales sont organisées en monocouche. Les réseaux de filaments d'actine de cellules voisines sont connectés et jouent un rôle clé dans la mécanique cellulaire. Sur la base de ces observations, nous étendons notre modèle précédent à l'étude du réseau de filaments d'une monocouche de cellules. Nos résultats suggèrent que la topologie du réseau de filaments est adaptée pour minimiser la déformation des cellules. En particulier, un réseau isotrope, typique des régions où l'écoulement varie beaucoup, protège les filaments des variations de déformation extrêmes. Nos résultats montrent aussi que la déformation des réseaux isotropes est polarisée, ce qui pourrait permettre un mécanisme de détection de la direction de la force.

Dans un dernier modèle, nous étudions comment les signaux mécaniques peuvent contrôler la direction de la migration cellulaire, un processus clé dans la formation des vaisseaux sanguins. La migration se fait en trois étapes de protrusion, d'attachement à la matrice, et de détachement des adhésions les plus faibles. Nous modélisons la cellule et la matrice par des matériaux élastiques couplés à l'interface où la cellule est attachée à la matrice. Les adhésions sont distribuées proportionnellement à la résistance à la déformation du couple matrice-cellule, puis détachées séquentiellement selon une probabilité dépendant de la force par adhésion. En accord avec les résultats expérimentaux, nous trouvons que la cellule migre préférentiellement vers les régions où la rigidité de la matrice est plus grande. Un obstacle dans la matrice, comme une autre cellule, est ressentie par une augmentation de la résistance à la déformation, et la cellule migre vers l'obstacle. Les informations mécaniques recueillies par la cellule pourraient ainsi être en jeu dans la formation des vaisseaux sanguins.

Les modèles développés dans ce travail permettent d'améliorer notre compréhension de la transduction des signaux mécaniques par les cellules et du rôle joué par les forces mécaniques dans le développement et la progression de l'athérosclérose.

Acknowledgements

I first want to thank the members of the jury: Denis Aubry and Daniel Isabey for accepting to review this thesis, Chaouqi Misbah and Cécile Sykes for accepting to take on the role of examiners.

Many thanks to Abdul Barakat, my PHD advisor, for the three years we worked together. I have learned a lot, and in particular to work autonomously. Thank you for being always ready to listen, advise, and support me.

I am also grateful to two postdocs in the team, Yongyun Hwang and David Gonzalez-Rodriguez. I thank Yongyun for his valuable help in starting up my first project. I thank David for the many inspiring discussions we had on my projects, and for all the ideas and technical help he gave me.

I had the chance to spend some time in Professor Roger Kamm's laboratory at MIT. I thank him and his team for their warm welcome and for the interesting collaboration that ensued. Indeed, we worked together on the project presented in the fourth chapter of this dissertation.

I thank everybody from LadHyX and from the "Mécanique et Systèmes Vivants" building for making these three years so pleasant and interesting.

Finally, I want to thank my friends and family. In particular, I thank David, Marion, Edwige, Edouard, Thomas and Guillaume for always being present. I thank my mother for her unfailing support and help, and my father for always being up for a chat.

Contents

List of Figures

List of Tables

Symbols

Chapters 2- and 3-specific symbols

$\mathbf{w}$	node displacement	m
w^v	node displacement in the direction transverse to the fiber	m
w^l	node displacement in the direction longitudinal to the fiber	m
ϵ	stress fiber strain	1
$\mathbf{F_{ext}}$	external force vector	N
F_0	external force magnitude	N
θ	external force direction	degrees
R	stress fiber radius	m
L	stress fiber length	m
A	stress fiber cross sectional area	m^2
I	stress fiber second moment of area	m^4
σ_p	stress fiber prestress	Pa
E	stress fiber Young's Modulus	Pa
γ	stress fiber internal viscosity	Pa s
$\mathbf{K}$	stiffness matrix	Pa
$\mathbf{\Gamma}$	damping matrix	Pa s

Chapter 2-specific symbols

α	oscillatory force component	1
β	constant force component	1
δ	angle between the two fibers of the network	degrees
f	oscillatory force frequency	s^{-1}

Chapter 3-specific symbols

k_{adh}	adhesion rigidity	N m^{-1}
α	angle of the hexagonal cell unit	degrees
q	isotropy index	1
f	fiber index	1
Ω	oscillatory force angular frequency	s^{-1}

Chapter 4-specific symbols

$\mathbf{u_m}$	matrix displacement field	m
$\mathbf{u_c}$	cell displacement field	m
$\epsilon_\mathbf{m}$	matrix strain tensor	m
$\epsilon_\mathbf{c}$	cell strain tensor	m
$\sigma_\mathbf{m}$	matrix stress tensor	Pa
$\sigma_\mathbf{c}$	cell stress tensor	Pa
σ_a	active stress tensor	Pa
σ_0	active stress tensor magnitude	Pa
$\mathbf{n}$	normal vector to the cell border	1
R	cell radius	m
h	cylindrical cell height	m
L	distance between the cell and the furthest matrix wall	m
d	distance between the cell and the closest matrix wall	m
E_c	cell Young's modulus	kPa
E_m	matrix Young's modulus	kPa
ν_c	cell Poisson's ratio	1
ν_m	matrix Poisson's ratio	1
E_{app}	apparent stiffness of the matrix	kPa
$n_{adh}(r)$	number of integrin proteins in region r	1
n_{adh}^{tot}	total number of integrin proteins of the cell	1
F_{adh}	force per integrin protein	pN
k	integrin rate of detachment	s^{-1}
$p(t)$	probability to detach in the time interval t	1
p_{first}^a	probability of attachment a to detach first	1

To my grandmother.

Chapter 1

Introduction

1.1 The endothelium and atherosclerosis

The vascular endothelium is the monolayer of cells that lines all blood vessels. Endothelial cells lie at the strategic interface between the bloodstream and the vascular wall (figure 1.1A), and they play a critical role in the physiology and pathology of blood vessels (Cines et al., 1998). As a barrier between the blood and the underlying tissues, the endothelium controls material transport. In regions of inflammation, endothelial cells regulate leukocyte recruitment and transit. As the structure in direct contact with blood, the endothelium is also responsible for preventing thrombosis. In response to acute changes in blood flow, endothelial cells express vasoconstrictors and vasodilators that control vascular wall tone and thus regulate blood pressure. Furthermore, in response to chronic variations in blood flow, endothelial cells trigger vascular wall remodeling, and, in the extreme case of very low blood flow, they undergo apoptosis and induce blood vessel shrinkage. Endothelial cells also drive the formation of new blood vessels, a key process in both vascular wound repair and in tumor growth.

Dysfunction of the endothelium is responsible for major pathologies, including atherosclerosis, the arterial disease that is the leading cause of mortality in developed countries. Atherosclerosis involves the formation of plaques within the walls of medium and large arteries (figure 1.1B). In its advanced stages, atherosclerosis can lead to heart attacks due to plaque rupture and/or blood flow obstruction or to strokes due to the plaque detachment. Atherosclerosis is triggered by sustained endothelial inflammation, which leads to the enhanced transport of macromolecules from the bloodstream into the arterial wall and their accumulation therein. Concomitantly, leukocytes are recruited by the inflamed endothelial cells but ultimately become a part of the atherosclerotic plaques as they differentiate into macrophages and subsequently into foam cells (Faxon et al.,
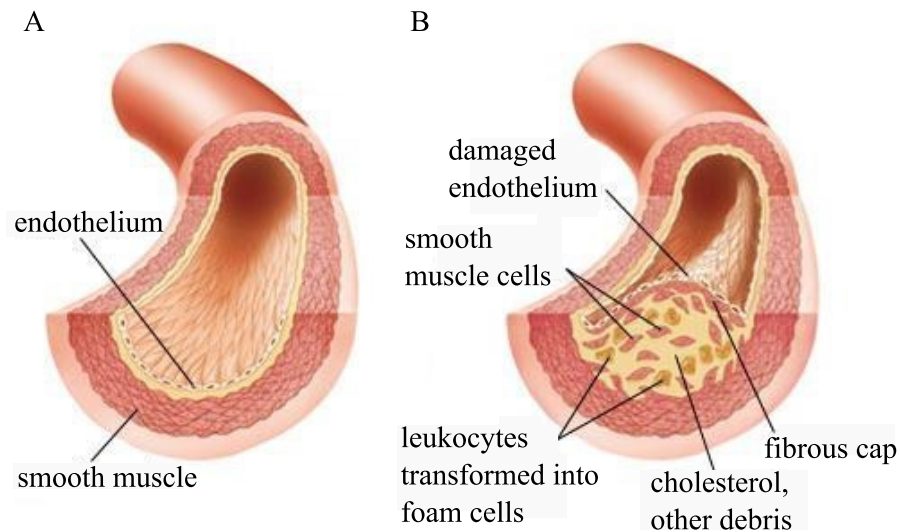
FIGURE 1.1: A. In a normal artery, the arterial wall is made of distinct and concentric layers, with the endothelium at the interface with the blood. B. In an atherosclerotic artery, accumulation of foam cells and other debris lead to the formation of a plaque which may obstruct normal blood flow. Adapted from the Encyclopedia Britannica.

2004, Libby et al., 2011). Thus, a normally functioning endothelium is critical for the health of arteries.

1.2 Role of mechanical forces in endothelial physiology, development and pathology

Over the past decades, mechanical forces have been shown to play a critical role in a wide array of biological processes. An early illustration of this principle was the work of Wolff et al. (1986) who showed that bone remodels to resist increased loading. Since this pioneering work, mechanical cues have been shown to be key regulators of the structure and function of many tissues inclunding the lung (Wirtz and Dobbs, 2000) and the heart, and changes in the mechanical environment and in cellular responses to this environment are involved in several diseases (Jaalouk and Lammerding, 2009). During development, mechanical and chemical cues must be integrated to shape the organism (Ingber, 2006, Patwari and Lee, 2008). For instance, establishment and detection of fluid flows are involved in such fundamental processes as the definition of left-right asymmetry, while cell contraction is necessary to fold tissues into shape (Ingber, 2006, Patwari and Lee, 2008).

By virtue of its position at the interface between the vascular wall and the pulsatile blood flow, the endothelium is constantly subjected to a spatially varying and highly dynamic mechanical stress field. Mechanical forces have been shown to be involved in

all steps of an endothelial cell's life (Davies, 2008, Hahn and Schwartz, 2009). In the mature vascular tree, blood flow subjects vessel walls to pressure and frictional forces that oscillate in time due to the periodic contractions of the heart. Large vessels such as arteries expand and contract with the variations in blood pressure, thus dampening these variations for the downstream smaller and less elastic vessels. Blood pressure and the resulting cyclic stretch drive the contractility of muscle cells that underly the endothelium. In small vessels, an increase in blood pressure triggers smooth muscle cell contraction which leads the vessel to narrow and to maintain a constant blood flow to targeted organs (Hahn and Schwartz, 2009). Although endothelial cells are constantly subjected to pressure due to the transmural pressure difference, the mechanical parameter that is thought to be the primary regulator of endothelial function is shear stress, the frictional force per unit area caused by the flow of viscous blood. Under high shear stress, endothelial cells produce substances such as nitric oxide that drive smooth muscle cell relaxation and vessel dilatation (Di Stefano et al., 1998). On the other hand, low shear stress triggers endothelial cell signals to narrow the arteries, and under very low flow, endothelial cells undergo apoptosis and the vessel may even collapse (Langille et al., 1989). The picture that has emerged is that high shear stress stabilizes vessels and promotes enlargement of their lumens, whereas low flow leads to vessel shrinkage or even vessel collapse (Di Stefano et al., 1998, Langille et al., 1989).

The role of flow in determining the fate of blood vessels is corroborated by data demonstrating the involvement of fluid mechanical shear stress in vasculogenesis, the initial formation of blood vessels, and in angiogenesis, the sprouting of new vessels from existing ones. The cardiovascular system is the first organ to develop in vertebrate empryos. Morphogenesis of blood vessels begins with the formation of a network of small channels lined by endothelial cells. After the primitive heart begins to beat and blood cells enter the circulation, this initial network remodels in the presence of flow to form a branched tree of small and large vessels (Hahn and Schwartz, 2009, Lucitti et al., 2007). Lucitti et al. (2007) showed that the remodeling is not triggered by a change in oxygen or nutrient delivery; however, an increase in the viscosity of the fluid, and hence in wall shear stress, is necessary and sufficient to initiate vascular remodeling. Angiogenesis is critical in tissuer repair, which often requires enhanced blood delivery, and for tumor vascularization. High fluid shear stress promotes the stability of existing vessels and attenuates endothelial cell sprouting, whereas interstitial fluid flow directs migration of endothelial cells to form new vessels (Song and Munn, 2011).

In addition to its role in promoting blood vessel stability and growth in morphogenesis, angiogenesis and normal physiology, fluid shear stress is also involved in the development of pathologies, most notably atherosclerosis. As shown in figure 1.2, atherosclerosis
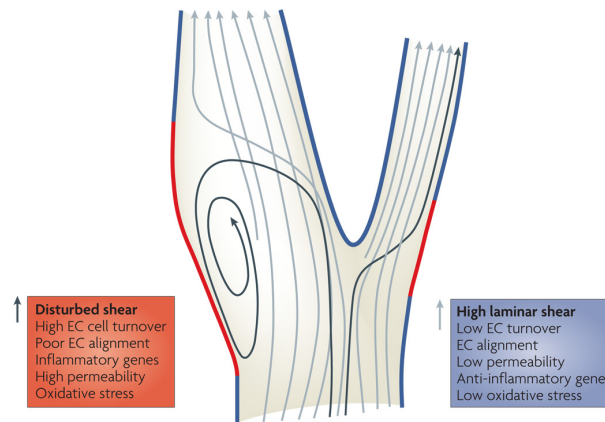
FIGURE 1.2: Schematic of arterial blood flow patterns. In straight regions (blue), endothelial cells are subjected to a high, oscillatory but non-reversing shear stress and their phenotype is protective from atherosclerosis. In regions of curvature or arterial bifurcation (red), blood flow recirculation yields low, reversing shear stress. Under these conditions, inflammation and increase in permeability of the endothlium can lead to the formation of an atherosclerotic lesion. Drawing from Hahn and Schwartz 2009.

develops preferentially in regions of arterial curvature and bifurcation, where recirculation and reattachement of blood flow yield low time-averaged shear stress, high shear stress gradients and/or a significant backflow component (Caro et al., 1969, Malek et al., 1999). Such shear stress profiles have been shown to induce endothelial cell inflammation and to increase endothelial permeability and cholesterol uptake into the arterial wall (Chatzizisis et al., 2007, Hahn and Schwartz, 2009). These observations demonstrate the role of what is termed "disurbed" flow in the development of atherosclerosis.

1.3 Mechanical cues and endothelial cell behavior

We now zoom in on the cellular scale. As suggested by its role in endothelial function, shear stress is a key determinant of endothelial cell structure and function. Because atherosclerosis develops preferentially in regions where shear stress is low with a significant backward component while regions of high non-reversing shear stress remain largely spared (Caro et al., 1969, Malek et al., 1999), endothelial cell behavior is often studied under these two characteristic flow conditions. Henceforth, we refer to regions of low, reversing shear stress as "disturbed" flow regions and to regions of high, non-reversing shear stress as "undisturbed" flow region, a terminology widely used in the literature (Davies, 2008, Hahn and Schwartz, 2009, Malek et al., 1999).

Undisturbed flow has been shown to reduce the rate of endothelial cell proliferation and apoptosis, whereas disturbed flow promotes an increase in cell turnover rate (Levesque et al., 1990, Li et al., 2005). These observations lend support to the idea that undisturbed flow yields a quiescent cellular state that protects against the formation of

atherosclerotic lesions, whereas disturbed flow leads to conditions that are favorable for the development of lesions (Davies, 2008, Hahn and Schwartz, 2009).

Endothelial cells elongate and align in the direction of undisturbed flow, but they remain cuboidal similar to cells in static culture when subjected to disturbed flow (Dewey et al., 1981, Flaherty et al., 1972, Helmlinger et al., 1991, Lum et al., 2000, Wong et al., 1983). These changes in cell morphology also affect cytoskeletal organization (Galbraith et al., 1998). Thus, endothelial cells subjected to undisturbed flow exhibit a highly organized cytoskeletal architecture where the filaments are largely oriented in the flow direction, whereas cells in disturbed flow are associated with an isotropic cytoskeletal organization. Similar to many other cell types, endothelial cell morphology can also be driven by the rigidity of the substrate, and endothelial cells have been shown to go from round to well-spread when substrate rigidity is increased (Yeung et al., 2005).

Undisturbed flow has been shown to promote endothelial cell migration in the direction of flow, but this effect is less clear in the case of disturbed flow (Li et al., 2005). When a monolayer of endothelial cells is scratched, cells migrate from the two sides of the scratch to close the wound. This process is favored when the monolayer is submitted to undisturbed flow (Dewey et al., 1981, Gojova and Barakat, 2005). If endothelial cell migration is sensitive to active forces such as flow shear stress, it is also impacted by substrate stiffness. Similar to other cell types, endothelial cells appear to migrate preferentially towards stiffer regions (Hadjipanayi et al., 2009, Lo et al., 2000).

In regions of disturbed flow, genes associated with vasodilation and vascular wall relaxation are dowregulated whereas genes that code for leukocyte adhesion molecules and growth factors are upregulated (Chatzizisis et al., 2007). Furthermore, stem cell differentiation can be driven by tuning substrate stiffness to match that of the mature target organ (Engler et al., 2006). These results show that mechanical cues have a profound effect on gene expression and protein synthesis.

1.4 How does a cell feel mechanical cues?

1.4.1 Mechanical homeostasis between the cell and its environment

In vivo, cells are either embedded within or sit on the extracellular matrix, a network of fibrous proteins such as collagen, fibronectin, laminin, etc. that are secreted and organized locally by cells, gels of polysaccharides, and interstitial fluid (Alberts et al., 2002). Cells attach to the extracellular matrix via transmembrane proteins, mainly belonging to the integrin family (Hynes, 1987). Integrins bind to specific ligands in

the extracellular matrix and are connected to the cytoskeletal network within the cell (Alberts et al., 2002). They thus provide a physical bridge between the cell and its environment, as pictured in figure 1.3.

Most integrins bind to the actin cytoskeleton via a scaffold of adaptor and regulator proteins (Brakebusch and Fässler, 2003). The molecular motor myosin moves along two actin filaments and slides filaments against one other, thus generating tension at the filament ends, and more globally cellular contraction (Alberts et al., 2002). This contraction is transmitted via the integrins to the extracellular matrix as traction forces (Harris et al., 1980).

Increasing matrix stiffness or application of a force to an integrin have been shown to elicit an increase in cell contraction and adhesion strength (Balaban et al., 2001, Choquet et al., 1997, Wang et al., 2002). These results have led to the concept that cells are in homeostasis with their mechanical environment and constantly probe and adapt to passive (e.g. matrix rigidity) and active (e.g. flow shear stress) mechanical cues sensed at adhesion sites (Moore et al., 2010, Ricca et al., 2013). In this view, cells have been suggested to act as tensegrity structures whose shape results from the balance between actin filaments in tension, microtubules in compression and the substrate on which the cell pulls (Ingber, 1997). When the substrate resistance to pulling is changed or when a force is applied to the tensegrity structure, a new balance must be struck, which may explain results such as dependence of cell morphology on mechanical cues.

1.4.2   Molecular mechanisms of mechanotransduction

Mechanotransduction is the study of the conversion of mechanical signals to biological messages that can induce changes in gene expression and overall cell behavior. Mechanotransduction and subsequent integration of the information remains incompletely understood, and several mechanisms have been proposed, all of which could play a role regulating cell function and dysfunction. Figure 1.3 illustrates some of these different mechanisms.

The search for a mechanism of conversion of mechanical cues to biological signals begins at the cell surface, where the force is applied. Ion channels whose gating profile changes under mechanical load have been identified (Sukharev et al., 2001). Activation of these mechanosensitive ion channels could result from a force-driven change in cell membrane tension or from the relative motion of structures anchored to ion channels, for instance the cytoskeleton and the extracellular matrix (Barakat et al., 2006, Martinac, 2012).
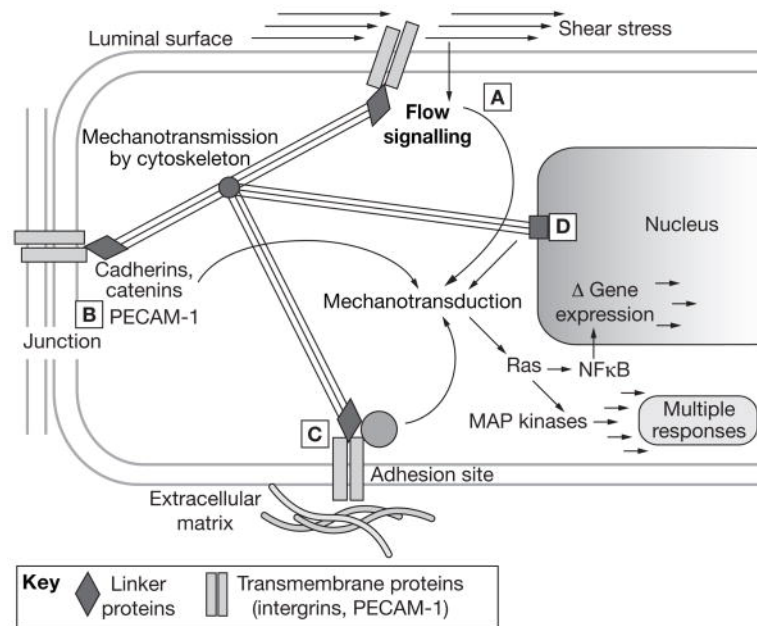
FIGURE 1.3: Cellular mechano-chemical conversion can occur at the cell surface, for instance by a change in mechanosensitive ion channel gating or G-protein activation (A), or via signaling at cell-cell (B) or cell-matrix junctions (C). Mechanical forces may also be transmitted via the cell cytoskeleton to intracellular structures such as the nucleus (D) where they are converted to a chemical signal. Diagram from Davies 2008.

Given their role in physically linking a cell and its extracellular matrix, integrins appear as a legitimate candidate mechanosensor. The formation of a bond between two molecules is described by the energy profile of the interaction, and the difference in energy between the bound and unbound states determines the most stable state and the energy barrier between the states: the higher the barrier, the more difficult the transition. Application of a force to two bound molecules provides energy and usually decreases the energy barrier with the unbound state, thus favoring unbinding (Bell, 1978). However, application of a force can reveal new interaction sites that strengthen the binding. Such bonds are exceptions to the rule, and are referred to as catch bonds. The bond between an integrin and its matrix ligand has been shown to be a catch bond (Balaban et al., 2001). Since mechanical force increases the energy gain associated with binding of integrins to the matrix, more integrins engage into linkage, which is a significant biological event. This process has been shown to be involved in stiffness sensing (Choquet et al., 1997).

Cell–cell adhesions are transmembrane proteins that link cells together. They share many similarities with cell–matrix adhesions, including connection to the cytoskeleton via a scaffold of proteins (Chen et al., 2004). The role of cell–cell adhesions in mechanotransduction is not as well established as the role of cell–matrix adhesions; however, experimental results showing that responsiveness to flow is mediated by a cell–cell adhesion complex (Tzima et al., 2005) has demonstrated that this structure is also involved

in mechanotransduction.

Mechanotransduction has also been shown to occur further within the cell. Integrins link to actin filaments via a scaffold of proteins that is tightly regulated by force (Schiller and Fässler, 2013). Stretching of cells that have been stripped of their membrane leads to increased binding to the cytoskeleton of some of these proteins, such as focal adhesion kinase, p130Cas and paxillin (Sawada and Sheetz, 2002, Tamada et al., 2004). Stretching of another protein, talin, has been shown to induce binding of vinculin to talin (del Rio et al., 2009). Protein conformational changes have also been suggested to expose specific reaction sites, such as phosophorylation sites (Sawada et al., 2006). These results suggest that the mechanical signal is not necessarily converted near the cell membrane, and that uncovering of protein interaction sites and of reaction sites can be induced by forces within the cell. It has thus been suggested that mechanical signals could be directly transmitted by the cytoskeleton to various intracellular sites including the nucleus where they are converted to a chemical signal that regulates cell structure and function (Wang et al., 2009).

1.5   Thesis outline

In this work, we integrate experimental knowledge and mechanical concepts into theoretical models at the subcellular, cellular, and multicellular scales. Our goal is to study if and how the mechanical behavior of structures such as actin stress fibers or the extracellular matrix plays a role in the response of cells to mechanical cues.

Mounting experimental evidence of direct force transmission from the cell surface to intracellular structures such as the nucleus has led to the suggestion that actin stress fibers may mediate force transmission (Na et al., 2008, Wang et al., 2009). Actin stress fibers are bundles of actin filaments and myosin molecular motors that are found in a number of cell types cultured on 2D substrates. Apart from the fact that they connect integrins to intracellular structures and that their integrity is necessary for mechanotransduction at a distance, there is no clear evidence of the role of stress fibers in the transmission of force. In a first model, we study intracellular force transmission by a network of actin stress fibers by describing strains that develop in the stress fibers in response to an externally applied force. We compare the model results with experimental observations to investigate the role of the cell stress fiber network in mechanotransduction.

We then extend this model to study force transmission in a monolayer of cells. In particular, we investigate the role of stress fiber organization and of external force characteristics in the strain experienced by the monolayer. In the specific case of endothelial cells, this approach appears to shed light onto the correlation among disturbed flow, cell morphology, and predisposition to the development of atherosclerosis.

In the final model, we study how mechanical cues drive the direction of endothelial cell migration, a key process in vascular wound healing and in the formation of new blood vessels. Motivated by experimental evidence that cells migrate towards regions of greater stiffness, where adhesions with the matrix are stronger, we propose a model of migration based on the "apparent stiffness" felt by a cell that contracts in a three dimensional matrix.

If validated experimentally, the various models proposed in this work provide an understanding of how actin stress fibers may contribute to force transmission within and among cells and how mechanical factors regulate important aspects of cellular migration.

Chapter 2

Model of Cellular Mechanotransduction via Actin Stress Fiber Networks

This chapter is currently under review in the Journal of Royal Society Interface.

2.1 Introduction

Vascular endothelial cells, the cells that line the inner walls of blood vessels, are constantly subjected to mechanical stresses due to blood flow. These stresses regulate many aspects of cell structure and function and play a role in the development of atherosclerosis (Davies, 2008, Hahn and Schwartz, 2009). In arterial regions of branching and bifurcation where blood flow is disturbed, endothelial cells are generally round with isotropic cytoskeletal organization (Flaherty et al., 1972, Malek et al., 1999, Wong et al., 1983), and they exhibit an inflammatory phenotype that is susceptible to atherosclerosis (Caro et al., 1969, Chatzizisis et al., 2007). In contrast, in regions of undisturbed flow, endothelial cells are elongated and exhibit cellular alignment and cytoskeletal polarization in the primary flow direction (Flaherty et al., 1972, Malek et al., 1999, Wong et al., 1983). These cells are also associated with an anti-inflammatory and atheroprotective phenotype (Davies, 2008). These two different endothelial cell phenotypes can be reproduced in vitro by subjecting the cells to either low or reversing shear stress (a form of disturbed flow) or to high and non-reversing shear stress (representative of undisturbed flow) (Chatzizisis et al., 2007, Dewey et al., 1981, Galbraith et al., 1998, Helmlinger et al., 1991). Despite these observations, the connection between flow-derived

mechanical stresses, endothelial cell cytoskeletal organization (or cell shape), and cellular susceptibility to atherosclerosis remains to be elucidated.

How cells respond to mechanical cues is a subject of intense research interest (Hoffman et al., 2011, Orr et al., 2006). Key questions include how cells sense mechanical stimuli, how mechanical signals are transmitted within cells, and how these signals ultimately regulate gene expression and protein synthesis. Several candidate mechanosensors have been identified including the cell membrane (Haidekker et al., 2000), the glycocalyx (Florian et al., 2003, Tarbell and Pahakis, 2006), mechanosensitive ion channels (Barakat et al., 2006, Sukharev et al., 2001), focal adhesion sites and associated proteins (Choquet et al., 1997, Friedland et al., 2009, Geiger et al., 2009), and cell-cell adhesion complexes (Leckband et al., 2011, Tzima et al., 2005, Yonemura et al., 2010). The principal mechanotransduction mechanisms proposed thus far involve mechano-chemical conversion by one of these structures and subsequent transmission of the resulting chemical signal to target intracellular sites via either reaction-diffusion cascades or molecular translocation. One issue, however, is that these processes are relatively slow. The largest reported diffusion coefficient of proteins in the cytoplasm is ~60 μm^2/s (Costa et al., 2006), which yields a minimum diffusion time across a typical cell length (20 μm) of ~6 s. Translocation of proteins via molecular motors requires comparable transmission times of a few seconds (Ashkin et al., 1990). Recent experiments, however, have demonstrated that a force exerted on the cell surface can induce a biological response across the cell within ~300 ms (Na et al., 2008), a time too short to be explained by either reaction-diffusion cascades or molecular translocation. More specifically, upon application of a force, there is very rapid activation of the mechanosensitive protein Src (Na et al., 2008) as well as displacement of cytoplasmic and nucleolar structures (Hu et al., 2005, 2003). The mechanisms by which very rapid mechanical signal transmission occurs within cells remain to be elucidated.

There is mounting evidence that very rapid mechanical signal transmission requires an intact cytoskeleton (Hu et al., 2005, Na et al., 2008, Wang et al., 2009). A force applied to a network of cytoskeletal fibers is transmitted through the fibers at the elastic wave speed, on the order of 30 m/s (Na et al., 2008). At this speed, the force would be transmitted across a cell in ~1 μs, a virtually instantaneous response compared to any of the time scales discussed above. So, the cytoskeleton provides a pathway for transmitting a mechanical signal virtually instantaneously throughout a cell. Furthermore, the observation that the binding of specific proteins to actin stress fibers depends on the extent of stretch of the fibers (Colombelli et al., 2009, Sawada and Sheetz, 2002) suggests that the role of the cytoskeleton in mechanotransduction may extend beyond rapid force transmission to direct mechano-chemical conversion.

In light of the experimental observation that rapid transmission of mechanical signals in cells depends specifically on prestressed actin stress fibers (Na et al., 2008), Hwang and Barakat proposed a model for mechanical signal transmission through a single, prestressed, viscoelastic stress fiber (Hwang and Barakat, 2012). They showed that when stress fiber viscoelasticity is taken into account, the time scale for stress fiber deformation can be on the order of 1-10 ms, approaching that observed experimentally. They also showed that fiber prestress leads to two very different time scales for signal transmission, depending on whether the force is applied in the longitudinal or transverse direction relative to the fiber, thus potentially allowing the cell to distinguish between these two different directions of force application.

In the present work, we extend the single-fiber model of Hwang and Barakat to study mechanical signal transmission through stress fiber networks. We wish to particularly study the dependence of mechanical signal transmission on the extent of stress fiber alignment in order to explore if different cytoskeletal configurations as seen in elongated versus round endothelial cells transmit mechanical signals differently. We hypothesize that the relevant parameter for mechanical signal transmission through the cytoskeleton is not the force, which is virtually instantaneously transmitted within the cell, but rather the force-induced strain, whose development is delayed due to the viscoelasticity of stress fibers. In this new paradigm, the mechanical signal would induce protein activation not through stress but rather through strain, which has already been proposed as a possible mechanism for protein activation (Han et al., 2004, Sawada and Sheetz, 2002). Our results demonstrate that strain-mediated mechanical signal transmission through actin stress fibers allows a cell to integrate information derived from both the nature of the applied external force and the organization of the stress fiber network. These findings have interesting implications for potential links among arterial flow-induced stresses on endothelial cells, endothelial cell shape, and endothelial cell phenotype.

2.2 Methods

2.2.1 Model of a single stress fiber and simplification

Following the previous work (Hwang and Barakat, 2012, Hwang et al., 2012), we model actin stress fibers as uniformly prestressed viscoelastic filaments that link cell membrane proteins such as integrins/focal adhesions to other focal adhesions or to intracellular structures such as the nucleus. As depicted in figure 2.1A, we consider a stress fiber of length L, cross sectional area A, second moment of area I, density ρ, internal viscosity γ, elastic modulus E, and prestress σ_p. The stress fiber is surrounded

by a cytoplasm of viscosity μ that resists fiber transverse and longitudinal motion with drag coefficients C_v and C_l, respectively. The single stress fiber model of Hwang and Barakat (2012) led to partial differential equations that describe stress fiber movement. The details of these equations are given in Appendix 1.
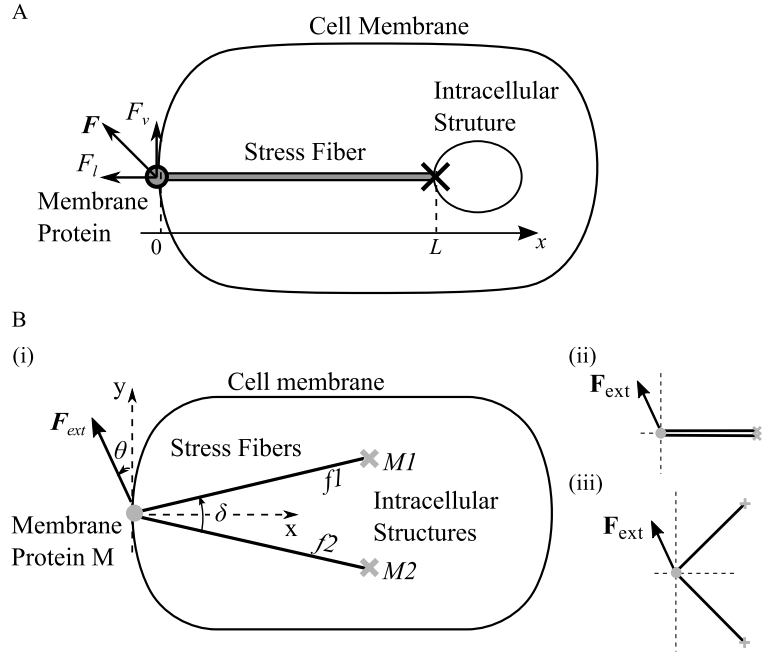
FIGURE 2.1: A. Schematic of an actin stress fiber that directly connects a membrane protein such as an integrin or a focal adhesion at one end to an intracellular structure such as the nucleus at the other end. B. (i) The two-fiber network in the context of the cell: the two fibers are linked at a moving node modeling a membrane protein (filled circle), and they connect to distinct intracellular structures (crosses) at the other end. (ii) Directionally aligned network ($\delta = 0°$). (iii) Isotropically aligned network ($\delta = 90°$).

For the case of multiple stress fibers that we wish to investigate here, it is desirable to explore possible simplifications of this model. In the previous work (Hwang and Barakat, 2012), it was shown that the bending stiffness, cytosolic drag, and inertia terms for transverse motion and the cytosolic drag and inertia terms for longitudinal motion are negligible compared to the other terms. Therefore, the equations of motion (A1.1) and (A1.2) can be simplified as follows:

$$\sigma_p A \frac{\partial^2 w_v}{\partial x^2} - \gamma I \frac{\partial^5 w_v}{\partial x^4 \partial t} + F_v \delta(x) = 0, \qquad (2.1a)$$

$$EA \frac{\partial^2 w_l}{\partial x^2} + \gamma A \frac{\partial^3 w_l}{\partial x^2 \partial t} + F_l \delta(x) = 0. \qquad (2.1b)$$

The fact that stress fiber inertia is negligible suggests that wave perturbations in the deformation field are damped by fiber internal viscosity. In support of this notion, the previous results for a single stress fiber (Hwang and Barakat, 2012) show that force transmission dynamics are indeed dominated by spatially monotonic deformation

of stress fibers. Therefore, the structure of the deformation field does not change significantly in time, and further simplification (see Appendix 2 for details) yields:

$$\frac{\sigma_p A}{L} w_v^{end}(t) + \frac{\gamma I}{L^3} \frac{dw_v^{end}(t)}{dt} = F_v, \tag{2.2a}$$

$$\frac{EA}{L} w_l^{end}(t) + \frac{\gamma A}{L} \frac{dw_l^{end}(t)}{dt} = F_l. \tag{2.2b}$$

Thus, the single stress fiber can be modeled simply as a two dimensional anisotropic Kelvin-Voigt body, in agreement with recent experimental observations (Kumar et al., 2006). To examine the validity of the two ODEs (2.2a) and (2.2b), we compare the results obtained with these ODEs to the results obtained with the full PDE model (Hwang and Barakat, 2012). The ODE model predicts that when a steady transverse forcing F_v is applied to the fiber, the resulting average strain of the fiber is:

$$\epsilon_v \approx -\frac{w_v^{end}(t)}{L} = \frac{F_v}{\sigma_p A} \left(1 - e^{-t/\tau_v}\right), \tag{2.3a}$$

where

$$\tau_v \equiv \frac{\gamma}{\sigma_p} \left(\frac{I}{L^2 A}\right). \tag{2.3b}$$

Similarly, the average strain under axial forcing F_l is:

$$\epsilon_l \approx -\frac{w_l^{end}(t)}{L} = \frac{F_l}{EA} \left(1 - e^{-t/\tau_l}\right), \tag{2.4a}$$

where

$$\tau_l \equiv \frac{E}{\gamma}. \tag{2.4b}$$

The time constants (2.3b) and (2.4b) are consistent with the time scales obtained by dimensional analysis in the previous work (Hwang and Barakat, 2012). Moreover, the time evolution of the mechanical signal dynamics described by (2.3a) and (2.4a) is remarkably similar to the dynamics described by the full PDEs, both for steady and oscillatory forcing. The order of magnitude of the average strain is also well reproduced by the ODEs.

2.2.2 The two-fiber network

In this article, we focus on a network of two stress fibers linking a membrane protein (moving node) to two intracellular sites (two fixed nodes) as represented in figure 2.1B. This network provides a simple model to study the role of cytoskeletal alignment, parametrized by the angle δ between the two fibers. As shown in figure 2.1B, when δ is

small, the two fibers are aligned (panel (ii)), while when $\delta \approx 90°$, there is no preferential direction, and the network is nearly isotropic (panel (iii)). In the context of arteries, the first case describes undisturbed flow regions of the arteries where endothelial stress fibers are highly aligned, whereas the second case describes disturbed flow regions where stress fibers are randomly oriented. Although we limit our study to networks of two stress fibers, it should be noted that the current formulation is sufficiently general and can be applied to any arbitrary network topology.

Given the simplification that inertia and cytoplasmic drag are negligible, the following balance of forces must be enforced at the moving node M:

$$\mathbf{F}_{f1 \to M} + \mathbf{F}_{f2 \to M} + \mathbf{F}_{ext} = \mathbf{0}, \tag{2.5}$$

where $\mathbf{F}_{ext}$ is an external force applied at node M, and $\mathbf{F}_{fi \to M}$ is the force applied to M due to the deformation of fiber fi, where $i = 1$ or $i = 2$. We also note that due to the moment-free nature considered at $M1$ and $M2$ from equation (A1.1c), the entire system is torquefree. Applying ODEs (2.2a) and (2.2b) to the fiber fi yields the components of $\mathbf{F}_{fi \to M}$ transverse and longitudinal to the fiber, $F^v_{fi \to M}$ and $F^l_{fi \to M}$:

$$F^v_{fi \to M} = \frac{\sigma_p A}{L}(w^v_{Mi} - w^v_M) + \frac{\gamma I}{L^3}\frac{d}{dt}(w^v_{Mi} - w^v_M), \tag{2.6a}$$

$$F^l_{fi \to M} = \frac{EA}{L}(w^v_{Mi} - w^l_M) + \frac{\gamma A}{L}\frac{d}{dt}(w^v_{Mi} - w^l_M), \tag{2.6b}$$

where w^l_m and w^v_m are the displacements of node m in the longitudinal and transverse fiber directions, respectively. Since the opposite node in each fiber is a fixed node, $\mathbf{w}_{Mi} = \mathbf{0}$ and the force depends only on $\mathbf{w}_M$. Using these equations into the balance of force (2.5) leads to the following system of linear differential equations of the motion of M:

$$\mathbf{\Gamma}\frac{d\mathbf{w}_M}{dt} = -\mathbf{K}\mathbf{w}_M + \mathbf{F}_{ext}, \tag{2.7a}$$

where $\mathbf{K}$ and $\mathbf{\Gamma}$ are respectively the stiffness and damping matrices:

$$\mathbf{K} = 2\begin{bmatrix} \frac{\sigma_p A}{L}\sin^2(\frac{\delta}{2}) + \frac{EA}{L}\cos^2(\frac{\delta}{2}) & 0 \\ \\ 0 & \frac{\sigma_p A}{L}\sin^2(\frac{\delta}{2}) + \frac{EA}{L}\cos^2(\frac{\delta}{2}) \end{bmatrix}, \tag{2.7b}$$

$$\mathbf{\Gamma} = 2\begin{bmatrix} \frac{\gamma I}{L^3}\sin^2(\delta) + \frac{\gamma A}{L}\cos^2(\delta) & 0 \\ \\ 0 & \frac{\gamma I}{L^3}\cos^2(\delta) + \frac{\gamma A}{L}\sin^2(\delta) \end{bmatrix}, \tag{2.7c}$$

where δ is the angle between the two fibers.

Equations (2.7b) and (2.7c) show that the two axes of symmetry of the two fibers (the x- and y- axes) are the eigen directions of the system: only an external force applied along one of these axes will result in a displacement along the same direction as the force. In this case, equation (2.7a) can be analytically solved, and the displacement of the moving node is:

$$\mathbf{w}_M = \begin{pmatrix} w_M^x \\ w_M^y \end{pmatrix} = \begin{pmatrix} F_{ext}^x/K_{xx}(1 - \exp(-t/\tau_x)) \\ F_{ext}^y/K_{yy}(1 - \exp(-t/\tau_y)) \end{pmatrix}, \tag{2.8}$$

where $\tau_x \equiv \Gamma_{xx}/K_{xx}$, $\tau_y \equiv \Gamma_{yy}/K_{yy}$ and K_{xx}, K_{yy}, Γ_{xx}, and Γ_{yy} are the non−zero entries of the matrices K and Γ defined in (2.7b) and (2.7c). τ_x, τ_y, K_{xx} and K_{yy} are the characteristic times and stiffnesses of the system associated with the eigen directions.

2.3 Results

The model parameter values for the mechanical and geometric properties of stress fibers are derived from literature (Table 2.1).

TABLE 2.1: Force transmission via a stress fiber network: mechanical and geometrical parameters

	Value	Source
R (m)	10^{-7}	Deguchi et al. 2006
		Kumar et al. 2006
A (m^2)	$\pi 10^{-14}$	$A = \pi R^2$
I (m^4)	$\pi/4 \ 10^{-28}$	$I = \int r^2 dA$
ρ (kg/m^3)	10^3	Na et al. 2008
E (Pa)	10^6	Deguchi et al. 2006
		Lu et al. 2008
σ_p (Pa)	$3 \ 10^5$	Deguchi et al. 2006
γ (Pa s)	$4 \ 10^6$	Kumar et al. 2006

To determine the mechanical behavior of the two−fiber network, we compute the effect of a known force on the strain ϵ in the stress fibers defined as:

$$\epsilon(x) = \frac{d\mathbf{w_M}}{dx}. \tag{2.9a}$$

As discussed in the Methods section, the strain is approximately uniform in x along one fiber, so we will only consider the average strain in the fibers:

$$\epsilon = \frac{\mathbf{w_M}}{L}, \tag{2.9b}$$

where $\mathbf{w_M}$ is the displacement vector of the membrane protein. As shown in equations (2.7), the strain depends on the force direction $\theta = \arctan(-F_{ext}^x/F_{ext}^y)$ and on stress fiber alignment as specified by the angle δ.

We consider an external force of magnitude 300 pN. In experiments using magnetic twisting device, a stress of $\sim$20 Pa is applied to beads of diameter $r \approx 4.5$ μm bound to membrane integrins (Hu et al., 2004, Na et al., 2008, Wang and Ingber, 1994). The force applied on the bead is then $F_{bead} \approx 1270$ pN. The adhesion density at the cell surface is typically $d = 0.15$ adhesions$/\mu$m^2 (Davies et al., 1993, 1994). If half the bead is embedded in the membrane, the bead surface area available for binding to membrane proteins is $2\pi r^2$, and the number of cell-bead adhesions would be $\sim 2\pi r^2 d$. This yields a typical force per adhesion of $F_{ext} = F_{bead}/2\pi r^2 d \approx 300$ pN. Finally, we should note that varying the force amplitude does not change the qualitative results as equation (2.7a) is linear.

2.3.1   Mechanical signal transmission in aligned fibers

We begin by examining the case of two perfectly aligned stress fibers ($\delta = 0°$) stimulated either along or orthogonal to the direction of fiber alignment as depicted schematically in figure 2.2A. In response to a constant force of 300 pN applied as a step function, both the transverse and longitudinal strains reach a plateau after an initial transient phase (figure 2.2B). The steady-state transverse strain (plateau value) is approximately three times higher than the steady-state longitudinal strain, and it is attained in only a few milliseconds versus 10 to 20 seconds for the longitudinal strain. These differences in the magnitude of the strains and in the associated dynamics are attributable to the fact that stress fiber prestress is the primary determinant of fiber transverse movement, whereas fiber elasticity is the primary determinant of longitudinal movement ($\sigma_p = E/3$ (Table 2.1)) and are consistent with the previous work on a single stress fiber (Hwang and Barakat, 2012).

To more closely mimic physiological conditions in the arterial system, we examine the response of the two aligned fiber model to an oscillatory forcing of the form:

$$F_{ext} = F_0(\alpha \sin(2\pi ft) + \beta), \tag{2.10}$$

where f is the oscillation frequency, and α and β are coefficients that modulate the amplitude, maximum, and mean of the forcing. In particular, if $\beta > \alpha > 0$, the force does not change sign in time, characteristic of undisturbed flow zones, whereas if $\alpha > \beta > 0$, the force changes sign periodically, a feature typical of disturbed flow regions.
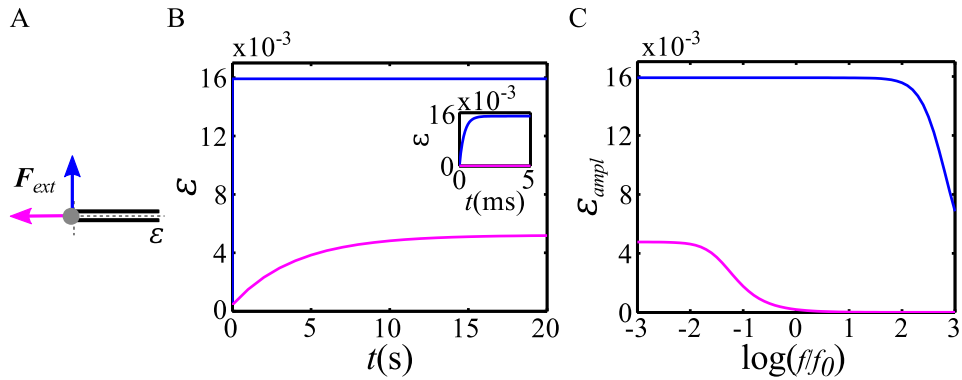
FIGURE 2.2: Signal transmission dynamics in a network of two perfectly aligned stress fibers ($\delta = 0°$) stimulated with an external force in either the transverse direction (blue) or the longitudinal direction (magenta). A. Schematic of the system: we apply an external force F at the membrane end of the fibers, and we track the time evolution of the resulting strain in the fibers. B. Strain as a function of time when a step force of 300 pN is applied. C. Amplitude of strain versus log of frequency for a non-reversing oscillatory forcing ($\alpha = 0.5$, $\beta = 0.75$, $F_0 = 300$ pN). f_0 is a reference frequency taken to be 1 Hz.

We first consider a non-reversing oscillatory forcing ($\alpha = 0.5$, $\beta = 0.75$), typical of undisturbed flow regions in arteries. Since the equations are linear, the resulting strain also oscillates with frequency f. Figure 2.2C shows the amplitude of this strain ϵ_{ampl} as a function of frequency, where ϵ_{ampl} is defined as follows:

$$\epsilon_{ampl} \equiv \max_{[t_0, t_0+1/f]}(\epsilon(t)) - \min_{[t_0, t_0+1/f]}(\epsilon(t)), \tag{2.11}$$

where t_0 is sufficiently large for steady-state to be reached. These results demonstrate that the system of two aligned fibers is a low-pass filter whose cutoff frequency depends on the direction of force application. The cutoff frequency is significantly lower in the longitudinal direction than in the transverse direction. This difference in cutoff frequencies correlates with the time scale of the strain response to a step force (figure 2.2B). Interestingly, under physiological conditions, $f \approx 1$ Hz (heart rate), the longitudinal signal is cut off whereas the transverse signal is not.

Therefore, the results in figures 2.2B and 2.2C show that application of either a step or oscillatory force in a network of two aligned stress fibers leads to drastically different signal transmission dynamics depending on whether the force is exerted along the axis or normal to the axis of fiber alignment. These results are consistent with the previous work on a single stress fiber (Hwang and Barakat, 2012), further demonstrating that the system of ODEs derived here captures the essential features of mechanical signal transmission. We find displacement values $w = \epsilon L$ of the order of 0.1 μm, in good agreement with various experimental results (Hu et al., 2003, 2004, Na et al., 2008).

2.3.2 Effect of fiber alignment on signal transmission efficiency

Figure 2.3 illustrates the dependence of the steady-state longitudinal and transverse strains in the top fiber of the network as a function of fiber alignment (δ) and force direction (θ). Although the figure only shows the strain values in the top fiber for $\delta \in [0, \pi]$ and $\theta \in [0, \pi]$, the strains for all other δ and θ and the strains in the bottom fiber can be readily deduced using symmetry arguments.

FIGURE 2.3: Steady-state strain in the directions longitudinal (A) and transverse (B) to the top fiber as a function of the angle between the fibers, δ, for different force directions - $\theta = 0°$ (solid blue line), $\theta = 45°$ (solid cyan line), $\theta = 90°$ (solid magenta line), $\theta = 135°$ (dashed cyan line), and $\theta = 180°$ (dashed blue line). The insets depict the configurations studied. The grey zones represent the envelope of values of the strain when the force direction spans the entire $[0°, 360°]$ interval. The steady-state strain is defined as the strain at $t \to \infty$ when a force of 300 pN is applied to the fiber in a step manner.

We consider that the steady-state strain in a stress fiber is a measure of the efficiency of mechanical signal transmission in that fiber. The results show that an external force applied in direction θ is transmitted with variable efficiency depending on the fiber alignment angle δ. For instance, at $\theta = 45°$, the longitudinal strain in the top stress fiber is highly sensitive to fiber alignment and even changes sign, going from tension (positive strain) at small δ to compression (negative strain) at large δ (figure 2.3A). Figure 2.3 also shows that for a given stress fiber alignment (fixed δ), transmitted strain ranges from compressive to tensile depending on the direction of the external force. The overall sensitivity of transmission efficiency to force direction is illustrated by the grey zones in figures 2.3A and 2.3B, which represent the envelope of strain values when the force direction spans the entire $[0°, 360°]$ interval. The longitudinal strain (figure 2.3A) is most sensitive to force direction when the fiber organization is isotropic ($\delta = 90°$), whereas transverse strain (figure 2.3B) is more sensitive to force direction when the fibers are aligned ($\delta = 0°$ and $\delta = 180°$). These results show that the extent of stress fiber alignment regulates the efficiency of mechanical signal transmission and the sensitivity

of the stress fibers to the direction of the externally applied force and to changes in force direction.

2.3.3 Effect of fiber alignment on signal transmission dynamics

Experiments suggest that actin stress fibers mediate very rapid transmission of mechanical signals within cells (Na et al., 2008). We wish to explore how stress fiber alignment modulates the dynamics of mechanical signal transmission and how this modulation is affected by the direction of the externally applied forcing. To this end, we compute the characteristic time for strain development in the two-fiber network in both the longitudinal and transverse directions as a function of both the stress fiber alignment angle δ and the angle of force application θ (figure 2.4). For a constant force applied as a step function, the characteristic response time T is defined such that:

$$\epsilon\left(T\right) \leq \frac{1}{\sqrt{2}} \max_{t}\left(\epsilon\left(t\right)\right). \tag{2.12a}$$

For an oscillatory force, T is defined as the cutoff period such that:

$$A\left(\epsilon\left(F_{T}\right)\right) \leq \frac{1}{\sqrt{2}} \max_{\tau}\left(A\left(\epsilon\left(F_{\tau}\right)\right)\right), \tag{2.12b}$$

where F_{τ} is a forcing of frequency $1/\tau$ as defined by equation (2.10) and A is the amplitude function. The cutoff period and the characteristic response time are equivalent as they both characterize the dynamics of the system. Note that when fibers are aligned ($\delta = 0°$ or $\delta = 180°$) and a force is applied along the direction of alignment ($\theta = 0°$ or $\theta = 90°$ respectively), $\epsilon_{tr} = 0$ and the characteristic time cannot be defined. Similarly, when the fibers are aligned and a force is applied orthogonal to the direction of alignment ($\theta = 90°$ or $\theta = 0°$ respectively), $\epsilon_{ax} = 0$ and the corresponding characteristic time cannot be defined. As in figure 2.3, we limit the study to the top fiber and to $\delta \in [0, \pi]$ and $\theta \in [0, \pi]$. Information on the bottom fiber and all other δ and θ values can be obtained from symmetry considerations.

Figure 2.4A indicates that a longitudinal strain can only be transmitted rapidly (grey zone) in the case of highly aligned configurations ($\delta \approx 0°$ or $\delta \approx 180°$) stimulated by a force acting normal to the stress fibers. Fiber alignment is also necessary for rapid transmission of transverse strains (figure 2.4B); however, a broader range of force directions allows these dynamics. As suggested by the stiffness and damping matrices (2.7b) and (2.7c), the x- and y- axes (axes of symmetry of the fibers) are eigen directions of the system, associated with two characteristic times whose interplay drives the dynamics of the system. Figure 2.4 shows that in the case of two aligned fibers, the time scales for signal transmission along the two eigen directions are very different with $\tau_{l} = \tau_{x} \approx 5$ s

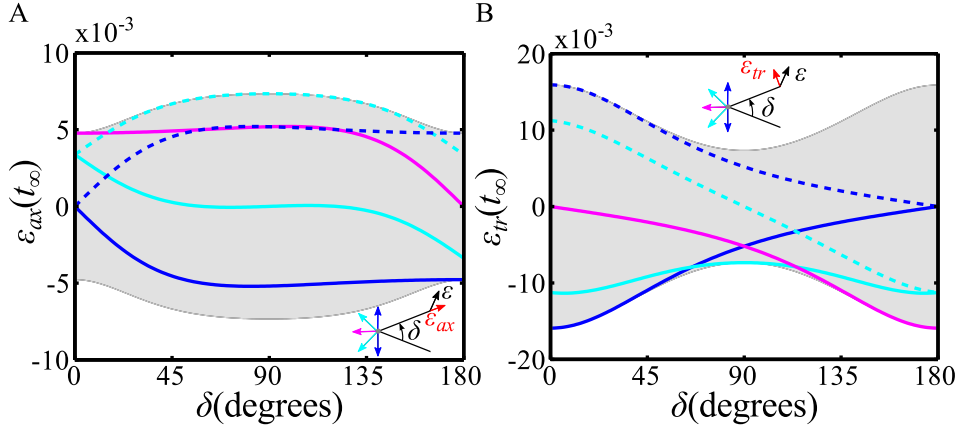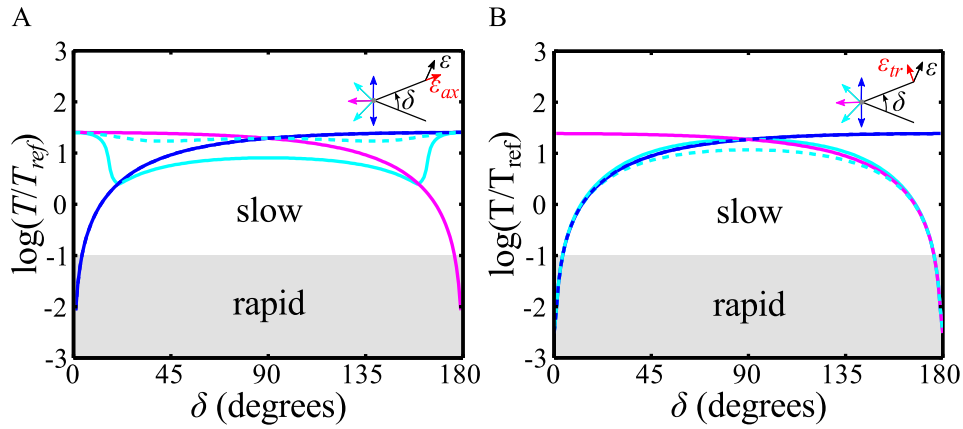FIGURE 2.4: Characteristic time of strain dynamics in the directions longitudinal (A) and transverse (B) to the top fiber as a function of the angle between the fibers, δ, for different force directions - $\theta = 0°$ (solid blue line), $\theta = 45°$ (solid cyan line), $\theta = 90°$ (magenta solid line), $\theta = 135°$ (dashed cyan line) and $\theta = 180°$ (dashed blue line). The insets depict the configurations studied. T_{ref} is a reference period, $T_{ref} = 1$ s . The grey zones delimit the regions of rapid force transmission, taken as $0.1 T_{ref}$ (100 ms).

and $\tau_v = \tau_y \approx 1$ ms. Thus, longitudinal strain dynamics are dominated by a slow time scale for all forces that have a non-negligible component in the longitudinal direction, and only the curves $\theta = 0°$ for $\delta = 0°$ and $\theta = 90°$ for $\delta = 180°$ are in the grey zone. On the other hand, the transverse strain is associated with rapid dynamics, and a broader range of external force directions can be rapidly transmitted. When the angle δ between the two fibers increases, the difference between the time scales decreases, and at $\delta = 90°$, the two time scales are equal with $\tau_x = \tau_y \approx 1$ s, and the general dynamics of the system are slow.

Thus, the results in figure 2.4 suggest that rapid mechanical signal transmission is only possible when fibers are significantly aligned. Furthermore, the narrow range of force directions inducing rapid longitudinal strain suggests that longitudinal strain is not a robust mediator of rapid mechanical signal transmission.

2.3.4 Spatial distribution of an applied force - strain differences between fibers

We have thus far presented results only for the top fiber, since the results for the bottom fiber can be deduced from symmetry arguments. However, it is instructive to compare signal transmission through the top and bottom fibers in order to develop an appreciation for the spatial distribution of an applied force. To this end, we study the ratio of the steady-state longitudinal strain in the top fiber to that in the bottom fiber,

r_{ax}, and the equivalent ratio for transverse strain, r_{tr}, i.e.:

$$r_{ax} = \frac{\epsilon_{ax}^{up}(t_{\infty})}{\epsilon_{ax}^{down}(t_{\infty})}, \ r_{tr} = \frac{\epsilon_{tr}^{up}(t_{\infty})}{\epsilon_{tr}^{down}(t_{\infty})}. \tag{2.13}$$

Figure 2.5 represents r_{ax} and r_{tr}^{-1} as a function of the fiber alignment angle δ for different force directions. For clarity, we plot r_{tr}^{-1} instead of r_{tr} to avoid infinite values and we restrict the representation to $\theta \in [0, 90]$. The symmetry of the system makes it straightforward to deduce the results for a broader range of θ, i.e. $r(\theta + \pi) = r(\theta)^{-1}$. Figure 2.5 shows that the mechanical signal in the top and bottom fibers can differ significantly $|r| \ll 1$. The strain in one fiber can be negligible compared to that in the other fiber ($|r| \approx 0$), and one fiber can be in compression while the other is in tension ($r < 0$). Thus, force transmission can be strongly heterogeneous in space, the implications of which will be considered in the Discussion section.
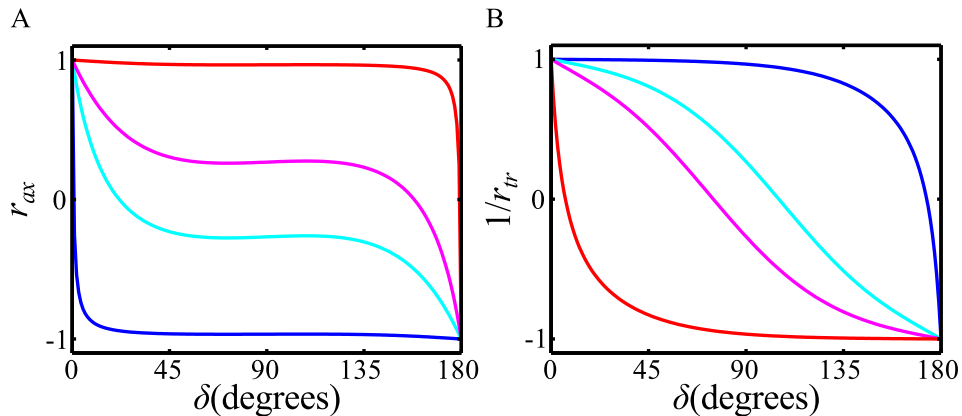
FIGURE 2.5: Ratio of the steady-state strain in the top fiber to that in the bottom fiber in the longitudinal direction (A) and the transverse strain (B) as a function of the fiber alignment angle δ for force directions $\theta = 1°$ (blue), $\theta = 30°$ (cyan), $\theta = 60°$ (magenta) and $\theta = 89°$ (red).

The spatial heterogeneity in force transmission depends strongly on stress fiber alignment angle, δ, and on force direction, θ. Unless the fibers are perfectly aligned ($\delta = 0°$), the strains are different in the two fibers and $|r| \neq 1$. We also note a plateau in the longitudinal strain ratio for intermediate values of θ, which is absent in the transverse strain ratio. Thus, over a broad range of stress fiber alignment angles δ, the longitudinal strain ratio is independent of δ and depends only on force direction angle θ. Another significant difference between the transverse and longitudinal cases is the localization of the maximum strain. For the range of force directions θ represented in figure 2.5, $|r_{ax}| < 1$ so that the longitudinal strain in the top fiber is smaller than that in the bottom fiber. The opposite is true for the transverse strain.

2.3.5   Role of forcing dynamics: reversing vs. non-reversing forcing

Experiments both in vivo and in vitro have shown that different shear stress profiles elicit different endothelial cell behavior. In particular, it has been suggested that atherosclerosis develops preferentially in zones of disturbed flow where the shear stress is low or reversing, whereas regions of high, non-reversing shear appear to be protected (Caro et al., 1969, Chatzizisis et al., 2007). To study possible differences in how forces characteristic of disturbed and undisturbed flow regions are transmitted, we consider an oscillatory non-reversing force F_A and a reversing force F_B. These forces are defined by equation (2.10), where we choose $F_0 = 300$ pN, $(\alpha_A, \beta_A) = (0.5, 0.75)$ and $(\alpha_B, \beta_B) = (0.75, 0.5)$. Thus, $\max(F_A) = \max(F_B) = 375$ pN, $\min(F_A) = 75$ pN and $\min(F_B) = -75$ pN, and the sign of F_A does not change in time whereas the sign of F_B does. Figures 2.6A and B represent the two applied force profiles over a period of oscillation T. We denote as ϵ_A and ϵ_B the norms of the fiber strains resulting from
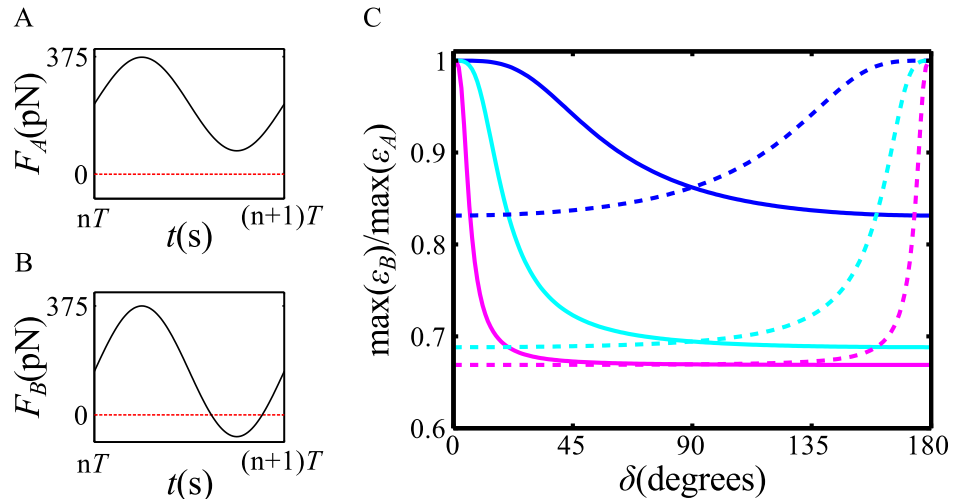
FIGURE 2.6: Non-reversing (A) and reversing (B) forcing over a period T. C. Ratio of the maximum strain in the top fiber when a reversing forcing is applied to the maximum strain in the same fiber in response to a non-reversing forcing. The force is applied in the directions $\theta = 0°$ (solid lines) or $\theta = 90°$ (dashed lines) at a frequency of $f = 0.1$ Hz (blue), $f = 1$ Hz (cyan), and $f = 10$ Hz (magenta).

stimulation by the non-reversing force F_A and by the reversing force F_B, respectively, and we plot the ratio of the maximum ϵ_B to the maximum ϵ_A over a period (figure 2.6C). Since the input forces F_A and F_B have the same maximum, a difference in the maximum of the resulting strains indicates a difference in signal transmission between the non-reversing and reversing cases. Interestingly, figure 2.6C shows that the ratio is always smaller than one, suggesting that a reversing forcing is less efficiently transmitted than a non-reversing forcing. When the fibers are isotropically organized ($\delta = 90°$), the ratio does not depend on force direction and is small. As the fibers become more

aligned, however, the ratio takes on a broader range of values depending on force direction. In the perfectly aligned configurations ($\delta = 0°$ and $\delta = 180°$), the sensitivity to θ is maximum, and the ratio reaches its minimum if the force is applied along the fiber axis and its maximum (equal to one) if the force is applied transverse to the fibers. These observations hold for all frequencies tested, $0.1 \leq f \leq 10$ Hz. However, as frequency increases, the minimum value of the ratio decreases and the stress fibers need to be more aligned to allow the ratio to approach unity.

The results of figure 2.6 are related to the existence of the two time scales τ_x and τ_y introduced above. As previously discussed, the oscillatory part of the signal is cut off when its frequency is greater than the inverse of the characteristic time scale of the system. As for the constant part of the signal, its transmission does not depend on frequency. Since the reversing force has a smaller constant component (β) and a larger oscillatory component (α), its transmission is more impacted by the cutting off of the oscillatory part of the signal than the non-reversing force. This cutting off of the oscillations occurs for configurations associated with a large time scale, i.e. for all force directions when the fiber configuration is isotropic and for forcing in the direction of the fibers when they are aligned.

2.4 Discussion

Consistent with previous experimental results (Hu et al., 2003, Hu and Wang, 2006, Na et al., 2008), the present model predicts long distance force transmission that depends centrally on prestress. Stress fiber displacement in response to an externally applied force similar to that used in previous experiments (Wang and Ingber, 1994) is found to be in good agreement with experimental results (Hu et al., 2003, 2004), $w = \epsilon L \sim 0.1$ μm (figure 2.3). The model also predicts the dynamics observed experimentally, in particular strain development within tens of milliseconds following application of a step force (Na et al., 2008), as well as low-pass filter behavior (Hu and Wang, 2006). Consistent with Hu et al. (2004), the model predicts that in the case of an elongated morphology (aligned fibers), rapid dynamics are associated with forcing orthogonal to the stress fiber axis and slow dynamics are associated with forcing along the stress fiber axis (figure 2.4). Thus, the present model provides a theoretical framework that explains various experimental results.

2.4.1 Prestressed stress fibers mediate rapid mechanical signal transmission

Experimental results suggest that prestressed stress fibers mediate rapid mechanical signal transmission in cells (Na et al., 2008). In particular, the application of a step force to integrins has been shown to induce very rapid (within 300 ms) activation of the mechanosensitive protein Src at discrete intracellular sites as far away as 20 μm from the site of force application. Diffusive transport and protein translocation along molecular motors would require several seconds to cover this distance, so these more "traditional" pathways for intracellular signaling fail to explain the experimental results (Na et al., 2008). In contrast, our model predicts that the time scale for strain development in prestressed actin stress fibers ranges from a few milliseconds to a few seconds. For certain stress fiber configurations that are subjected to forces in particular directions, strains are transmitted within several hundred milliseconds (grey zones in figure 2.4), in line with the experimental observations on Src activation (Na et al., 2008). These findings are consistent with the hypothesis advanced in this paper that strain transmission is a mechanism for stress fiber-mediated mechanotransduction.

Interestingly, there are key limitations to this rapid strain transmission pathway. Our results demonstrate that only highly aligned stress fibers stimulated by a force 'sufficiently' orthogonal to the direction of alignment of the fibers would allow strain transmission on this short time scale. In the arterial physiological context of an oscillatory forcing of period T, this implies that a force 'sufficiently' orthogonal to the fibers is efficiently transmitted within a cell even for high oscillation frequencies on the order of a kilohertz, whereas a force along the fibers is cut off when the oscillation frequency exceeds 0.1 Hz. This observation is in agreement with experimental results (Hu et al., 2004, Hu and Wang, 2006).

An interesting prediction of the model is that the definition of a 'sufficiently' orthogonal forcing is very strict in the case of a longitudinal strain, as a force only a few degrees away from the orthogonal fails to induce rapid longitudinal strain. On the other hand, a force at an angle of up to 50° away from the orthogonal direction can still elicit rapid transverse strain. The very narrow range of conditions allowing rapid longitudinal strain suggests that downstream signaling events that need to be robustly rapid would need to rely on transverse rather than longitudinal strain of the fibers.

2.4.2 Stress fibers: a critical link in the mechanotransduction chain?

Over the past years, many studies have focused on understanding how cells sense and respond to mechanical forces. An emerging paradigm is that mechanical forces

change the chemical landscape of the cell either by altering intracellular reaction kinetics, uncovering cryptic binding sites, or bringing together molecules that would otherwise be apart (Hoffman et al., 2011, Janmey, 1998, Vogel, 2006). In particular, several proteins that localize to focal adhesions including p130Cas (Sawada et al., 2006), zyxin (Lele et al., 2006) or talin (del Rio et al., 2009) have been shown to change their activity under force. Some of these proteins have also been shown to link to stress fibers in a manner dependent upon stress fiber stretch. Thus, it has been suggested that protein binding affinity to stress fibers is altered by tension (Colombelli et al., 2009, Sawada and Sheetz, 2002, Yoshigi et al., 2005). Our model indicates that the force-induced strain in stress fibers is not localized to the portion of the stress fiber in contact with focal adhesions but is rather distributed throughout the length of the stress fiber. Thus, we propose that mechano-chemical conversion may occur anywhere along the stress fiber length and not only at focal adhesions. This prediction is supported by recent experiments showing activation of the protein c-Src along stress fibers through binding to the mechanosensitive protein AFAP (Han et al., 2004). Activation of Src following application of a stress of 20 Pa by magnetic tweezers (Na et al., 2008) shows that the level of mechanical strain predicted by our model is sufficient to elicit such biological response. A mechanism to explain stress fiber strain perception by proteins has been suggested for zyxin. Zyxin, which has been implicated in the stabilization of stress fibers (Smith et al., 2010), has several LIM domains, which may act as a ruler to measure the distance between binding sites (Schiller and Fässler, 2013), so that the extent of zyxin binding to a stress fiber would be directly related to the strain in the stress fiber.

The present results show the potential richness of the stress fiber mechano-transmission pathway. In our model, the extent (figure 2.3) and dynamics (figure 2.4) of strain that a protein linked to a stress fiber would experience depend on the direction of the external force, the extent of stress fiber alignment, and the way the protein binds to the stress fiber, since whether a protein undergoes transverse or longitudinal strain depends on how the protein is attached to the fiber. For example, if the activity of a protein bound to a stress fiber is maximum at zero strain and the protein responds to longitudinal strain, then its average activity would be greater in aligned than in isotropic stress fiber networks, and its activity would be more sensitive to the direction of force application for isotropic networks (figure 2.3A). The opposite would be true if the protein were responsive to transverse strain. These examples show how the biological activity of a protein that is sensitive to stress fiber strain can be modulated by mechanical cues applied at the cell membrane and how different proteins that have different functions can be modulated differently.

The fact that the dynamics of strain development in stress fibers can range from milliseconds to several seconds depending on stress fiber organization and on force direction

(figure 2.4) may provide cells with the ability for temporal orchestration of responses to mechanical stimulation. In endothelial cells, relatively rapid force-induced responses including activation of mechanosensitive ion channels and of integrins as well as mobilization of intracellular calcium have been shown to occur over time scales ranging from a fraction of a second to several seconds after the onset of the mechanical stimulus (Kholodenko et al., 2010). These time scales are consistent with the results of the present model.

2.4.3 Cell polarization under force: the strain track

A prominent response of endothelial cells to shear stress is cellular polarization and alignment in the direction of shear (Dewey et al., 1981, Helmlinger et al., 1991). Several models have been proposed to explain this polarization, including a shear rate-dependent gradient of chemical cues around the cell (Shamloo et al., 2008) and shear stress-dependent activation of small GTPases at focal adhesions that triggers cytoskeletal remodeling (Li et al., 1999, Shyy and Chien, 2002). Our model shows that an external force induces a spatially heterogeneous strain in the stress fiber network (figure 2.5). As discussed above, this can in turn induce directional heterogeneity of protein activation. Since this heterogeneous strain contains information on force directionality, we propose stress fiber strain as a candidate mechanism through which a force can trigger early events in cell polarization.

2.4.4 Low-level stress fiber strain as a key feature of disturbed flow regions

It has been experimentally observed that cells respond differently to different types of forces. For instance, endothelial cells subjected to high, non-reversing shear stress exhibit a stress fiber architecture that is aligned in the direction of the applied force, and these cells exhibit a quiescent, anti-inflammatory, and atheroprotective phenotype. In contrast, cells subjected to low or reversing shear stress adopt an isotropic stress fiber organization and express an inflammatory phenotype that favors the development of atherosclerosis (Chatzizisis et al., 2007, Hahn and Schwartz, 2009, Malek et al., 1999). Our results demonstrate that a reversing forcing elicits smaller stress fiber strain than a non-reversing forcing (figure 2.6). At physiological frequencies, the strain difference can be as large as 30% even for the mild reversal considered in figure 2.6. Our model also predicts that a low non-reversing shear would lead to a small strain of the stress fibers. Thus, our results indicate that low- level stress fiber strain is a common feature of both reversing and low shear flows. As discussed above, this may impact the activity of many

proteins and subsequent signaling pathways and may play a role in the cell's adoption of an atheroprone or atheroprotective phenotype.

2.5 Conclusions

We have developed a model to study the transmission of mechanical signals in a network of prestressed viscoelastic actin stress fibers. To understand the correlation between external force characteristics, stress fiber alignment, and expression of atheroprotective or atheroprone genes, we studied a system of two fibers whose unique parameters are the alignment of the fibers and the external force characteristics. We showed that the dynamics of force transmission in the fibers are consistent with experimental results, and we proposed that strain-dependent binding of proteins to stress fibers may explain cell polarization and differences in cell function in disturbed versus undisturbed flow regions. We thus propose that stress fiber strain may be an intermediate mechanism to translate a force signal applied to the cell into a chemical signal, via the activation of strain-dependent proteins within the cell. Although the two-fiber network considered in the present work is very simple, we expect it to capture the essential features of mechanical signal transmission through a more complex network of stress fibers. In fact, the theoretical framework developed here can be readily expanded to allow the study of two- and three-dimensional networks of arbitrary complexity. Such a study, however, awaits quantitative experimental data on the topology of stress fiber networks in cells.

2.6 Appendix 1

Following the previous work (Hwang and Barakat, 2012), we model actin stress fibers as uniformly prestressed viscoelastic filaments that link cell membrane proteins such as integrins/focal adhesions to other focal adhesions or to intracellular structures such as the nucleus. As depicted in figure 2.1A, we consider a stress fiber of length L, cross sectional area A, second moment of area I, density ρ, internal viscosity γ, elastic modulus E, and prestress σ_p. The stress fiber is surrounded by a cytoplasm of viscosity μ that resists fiber transverse and longitudinal motion with drag coefficients C_v and C_l, respectively. Application of a force F_v orthogonal to the stress fiber axis at a point not far from the membrane protein results in a transverse displacement w_v governed by the

following momentum balance, derived from the equilibrium of moments:

$$
\rho A \frac{\partial^2 w_v}{\partial t^2} = \frac{\partial}{\partial x}\left(\sigma_p A \frac{\partial w_v}{\partial x}\right) -
$$
$$
\frac{\partial}{\partial x}\left(EI\frac{\partial^3 w_v}{\partial x^3} + \gamma I \frac{\partial^4 w_v}{\partial x^3 \partial t}\right) - C_v \mu \frac{\partial w_v}{\partial t} + F_v \delta(x).
$$

(A1.1a)

In this expression, stress fiber inertia is balanced by the restoring forces due to prestress σ_p and flexural rigidity EI, the internal damping force due to the flexural material viscosity γI, the cytosolic drag force, and the external forcing F_v applied at $x = 0$ ($\delta(x)$ is the Dirac delta function). As in (Hwang and Barakat, 2012), we consider a stress-free boundary condition at the membrane protein and a pinched boundary condition at the other end of the stress fiber:

$$
\left.\frac{\partial w_v}{\partial x}\right|_{x=0} = \left.\frac{\partial^3 w_v}{\partial x^3}\right|_{x=0} = 0,
$$

(A1.1b)

$$
w_v|_{x=L} = \left.\frac{\partial^2 w_v}{\partial x^2}\right|_{x=L} = 0.
$$

(A1.1c)

In the case of a longitudinal force F_l along the stress fiber axis, the longitudinal displacement w_l of the fiber is governed by the momentum balance:

$$
\rho A \frac{\partial^2 w_l}{\partial t^2} = \frac{\partial}{\partial x}\left(EA\frac{\partial w_l}{\partial x} + \gamma A \frac{\partial^2 w_l}{\partial x \partial t}\right) - C_l \mu \frac{\partial w_l}{\partial t} + F_l \delta(x).
$$

(A1.2a)

Here, fiber inertia is balanced by the restoring force due to the elastic modulus E, the internal damping force due to the material viscosity γ, the cytosolic drag on the fiber, and the external forcing F_l. The prestress term does not appear in equation (A1.2a) because the longitudinal forces due to a constant prestress σ_p at any point in the stress fiber are balanced in both directions. As in the case of transverse motion, we consider a stress-free boundary condition at the membrane protein and zero displacement at the the other end of the stress fiber:

$$
\left.\frac{\partial w_l}{\partial x}\right|_{x=0} = 0,
$$

(A1.2b)

$$
w_l|_{x=L} = 0.
$$

(A1.2c)

2.7 Appendix 2

Results obtained with a single stress fiber (Hwang and Barakat, 2012) suggest that stress fiber inertia is negligible, so that wave perturbations in the deformation field are damped by fiber internal viscosity. In support of this notion, the results show that force transmission dynamics are indeed dominated by spatially monotonic deformation

of stress fibers. Therefore, the structure of the deformation field does not change significantly in time, and displacement of the fiber can be written as:

$$w_v(x, t) = a_v(t)\psi_v(x), \tag{A2.1a}$$

$$w_l(x, t) = a_l(t)\psi_l(x). \tag{A2.1b}$$

Substituting (A2.1a) and (A2.1b) into (1a) and (1b) and integrating these equations over the spatial domain yields:

$$\frac{\sigma_p A}{L} \underbrace{\left(\int_0^1 \frac{d^2\psi_v(\hat{x})}{d\hat{x}^2} d\hat{x} \right)}_{C_{1,v}} a_v(t) +$$

$$\frac{\gamma I}{L^3} \underbrace{\left(-\int_0^1 \frac{d^4\psi_v(\hat{x})}{d\hat{x}^4} d\hat{x} \right)}_{C_{2,v}} \frac{da_v(t)}{dt} + F_v = 0, \tag{A2.2a}$$

$$\frac{E A}{L} \underbrace{\left(\int_0^1 \frac{d^2\psi_l(\hat{x})}{d\hat{x}^2} d\hat{x} \right)}_{C_l} a_l(t) +$$

$$\frac{\gamma A}{L} \underbrace{\left(\int_0^1 \frac{d^2\psi_l(\hat{x})}{d\hat{x}^2} d\hat{x} \right)}_{C_l} \frac{da_l(t)}{dt} + F_l = 0, \tag{A2.2b}$$

where $\hat{x}$ is defined as x/L.

Equations (A2.1a) and (A2.1b) can be used to relate the displacement of the free end of the fiber to the time functions a_v and a_l: $w_v^{end}(t) = a_v(t)\psi_v(0)$ and $w_l^{end}(t) = a_l(t)\psi_l(0)$ and $w_l(t) = a_l(t)\psi_l(0)$. Rearranging equations (A2.2) with $\hat{C}_{1,v} = C_{1,v}/\psi_v(0)$, $\hat{C}_{2,v} = C_{2,v}/\psi_v(0)$ and $\hat{C}_l = C_l/\psi_l(0)$, we obtain the following ordinary differential equations (ODEs) that describe the motion of the free end of the fiber ($x = 0$):

$$\frac{\sigma_p A}{L} \hat{C}_{1,v} w_v^{end}(t) + \frac{\gamma I}{L^3} \hat{C}_{2,v} \frac{dw_v^{end}(t)}{dt} + F_v = 0, \tag{A2.3a}$$

$$\frac{E A}{L} \hat{C}_l w_l^{end}(t) + \frac{\gamma A}{L} \hat{C}_l \frac{dw_l^{end}(t)}{dt} + F_l = 0. \tag{A2.3b}$$

An order of magnitude analysis on the three constants $\hat{C}_{1,v}$, $\hat{C}_{2,v}$ and $\hat{C}_l$ reveals that their magnitudes are $O(1)$. We detail the analysis for the case of $\hat{C}_{1,v}$:

$$\hat{C}_{1,v} = \frac{1}{\psi_v(0)} \int_0^1 \frac{d^2\psi_v(\hat{x})}{d\hat{x}^2} d\hat{x} = \frac{1}{\psi_v(0)} \frac{d\psi_v(\hat{x})}{d\hat{x}} \bigg|_{\hat{x}=1}, \tag{A2.4}$$

given that the boundary condition at $x = 0$ imposes that $d\psi_v(\hat{x})/d\hat{x}|_{\hat{x}=0} = 0$. The derivative of ψ_v at $\hat{x} = 1$ can be approximated by $(\psi_v(1) - \psi_v(0))/(1 - 0)$, where

$\psi_v(1) = 0$. Substituting this into (A2.4) yields $\hat{C}_{1,v} = O(1)$.

Because forces associated with prestress, elasticity, and material viscosity act against the direction of the externally applied force, their signs should be negative, and it is reasonable to approximate $\hat{C}_{1,v} = \hat{C}_{2,v} = \hat{C}_l = -1$. Hence, the transverse and longitudinal motions of the free end are governed by the two ODEs (2a) and (2b).

Chapter 3

Theoretical Model of Strain Transmission in a Monolayer of Cells

This chapter has been submitted as an invited paper to Cellular and Molecular Bioengineering.

3.1 Introduction

Many biological surfaces are lined by monolayers of cells that are subjected to various mechanical loads. For instance, intestinal epithelia are stretched during peristaltic movement in the gut, lung alveoli deform during breathing, and arterial endothelia are exposed to blood flow–derived shear stress (Guillot and Lecuit, 2013, Hahn and Schwartz, 2009, Roan and Waters, 2011). Of particular interest to us, mechanical stresses have been shown to play a key role in the physiology and pathology of vascular endothelium (Davies, 2008, Hahn and Schwartz, 2009). For instance, the formation at the arterial wall of an atherosclerotic plaque has been shown to colocalize with regions of branching and bifurcation where blood flow is disturbed (Caro et al., 1969, Chatzizisis et al., 2007). In these regions, endothelial cells are generally round with isotropic organization of actin stress fibers whereas in regions of undisturbed flow that remain largely spared of early atherosclerotic lesions, endothelial cells are elongated and exhibit cellular alignment and stress fiber polarization in the primary flow direction (Flaherty et al., 1972, Malek et al., 1999, Wong et al., 1983).

Much of the research in the field of cellular mechanotransduction has focused on the response of isolated cells to mechanical stress (Fletcher and Mullins, 2010, Hu et al., 2003, Na et al., 2008). Experiments on the responses of cellular monolayers to mechanical stimulation have revealed complex dynamics (Feneberg et al., 2004, Harris et al., 2012), anisotropy of the response with respect to force direction (Karcher et al., 2003), and transmission of locally applied mechanical signals to neighboring cells (Charras and Horton, 2002, Feneberg et al., 2004, Tambe et al., 2011). Several of these investigations point to a key role for the actin cytoskeleton and associated myosins (Feneberg et al., 2004, Harris et al., 2012), a result consistent with experimental observations on single cells (Hu et al., 2003, Na et al., 2008) and computational modeling results (Gouget et al., 2014, Hwang and Barakat, 2012) on single cells. Indeed, actin stress fibers constitute a particularly good candidate for mediating intercellular transmission of mechanical signals in light of evidence that stress fibers of adjacent cells in a monolayer are physically linked to one another at cell-cell junctions (Millán et al., 2010).

We had previously developed models of mechanical signal transmission via actin stress fibers within a single cell (Gouget et al., 2014, Hwang and Barakat, 2012, Hwang et al., 2012). In the present work, we propose that a force applied locally to a single cell in a monolayer gets transmitted via stress fibers to other cells in the monolayer. Thus, we extend our previous models to study force transmission in stress fiber networks whose topologies represent cellular monolayers. A key goal of this study is to establish how the differences in endothelial cell monolayer stress fiber alignment between atheroprotective and atheroprone regions (Flaherty et al., 1972, Malek et al., 1999, Wong et al., 1983) may impact the response of the monolayer to an externally applied force. The results demonstrate that such a model succeeds in reproducing several key experimental results regarding the magnitude of strain and the dynamics of its evolution as well as force transmission between neighboring cells. Interestingly, the model yields stress fiber strain levels that can exceed the reported thresholds for eliciting biological responses (Charras and Horton, 2002). Consistent with previous experimental findings (Glogauer et al., 1997, Tagawa et al., 1997), the model also predicts differences between isotropic and aligned stress fiber networks that suggest that stress fiber alignment allows enhanced strain propagation and thus improved cell-cell communication within a cellular monolayer.

3.2 Methods

3.2.1 Model of a cellular monolayer as a network of stress fibers

Experiments have demonstrated that actin stress fibers play a key role in determining the mechanical behavior of cellular monolayers (Feneberg et al., 2004, Harris et al., 2012). We wish to develop a model that describes this behavior and explores its potential implications for force transmission within the monolayer. Stress fibers of neighboring cells have been shown to be physically connected at cell–cell junctions, thus forming an intercellular fiber network through which force can potentially be transmitted (Millán et al., 2010). This represents the rationale for the present approach of modeling a monolayer of cells by its underlying network of stress fibers.

In cells, stress fibers form complex three-dimensional networks whose structure is difficult to describe quantitatively. In the present work, we do not wish to represent this high level of structural complexity. Rather, we propose to exploit the experimnetally–derived observation that the topology of the stress fiber network is correlated to the overall morphology of the cell (Cunningham and Gotlieb, 2004, Galbraith et al., 1998), i.e. the observation that when a cell is oriented in one direction, the global stress fiber orientation is also in the same direction. Therefore, we use cell borders, which delineate cell morphology, as a guide for setting the orientation of the stress fibers in the monolayer.

As depicted in figure 3.1, we follow two complementary approaches to investigate the effect of stress fiber alignment on mechanical signal transmission within a cellular monolayer. The first approach consists of "real" networks where we use phase contrast microscopy images obtained from the literature (Lum et al., 2000) of monolayers of cultured bovine aortic endothelial cells that had either not been exposed to flow (figure 3.1A) or that had been subjected in a parallel plate flow chamber to a steady shear stress of 2 Pa in the horizontal direction for a period of 24 hrs (figure 3.1D). As can be clearly seen from the images, the no–flow cells are cuboidal and exhibit no preferred orientation, whereas the cells exposed to flow are elongated and largely oriented in the flow direction. The contours of individual cells in these images were manually outlined as a series of straight line segments as shown in figures 3.1B and 3.1E. Each line segment is considered as a stress fiber, and each intersection point between two stress fibers is taken as a node in the network. As described in a later section, external forces can only be applied at nodes, and node displacement defines the strain field in the network. We will refer to the no–flow network (figure 3.1B) as the "isotropic" network and to the flow–elongated network (figure 3.1E) as the "aligned" network.
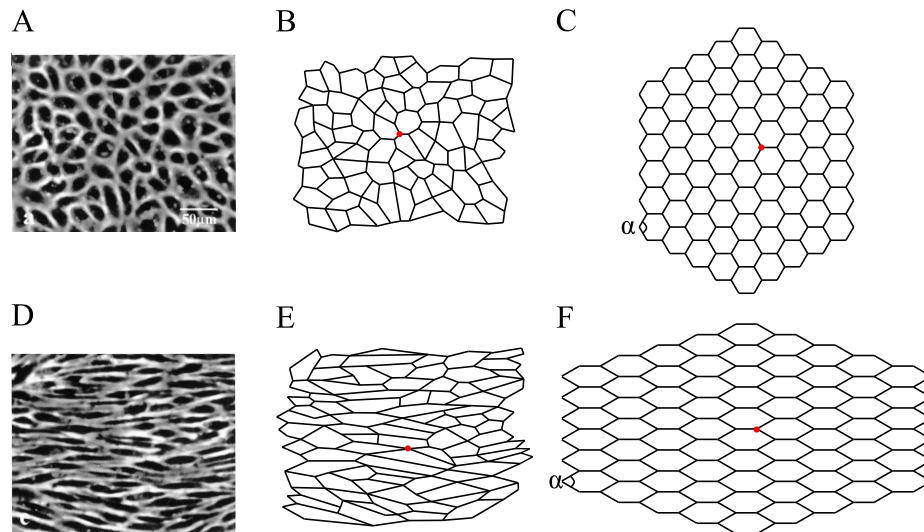
FIGURE 3.1: Based on phase contrast microscopy images of a monolayer of either round (A) or aligned (D) bovine aortic endohtelial cells, "real" isotropic (B) and aligned (E) networks of stress fibers are obtained. "Idealized" networks consisting of hexagonal cells are also studied, where the side angle of the hexagones, α, can be tuned to model isotropic ($\alpha = 120°$) (C) and aligned cases ($\alpha = 60°$) (F). The red dots in panels B, C, E, and F represent the points where the force is applied.

The two networks in figures 3.1B and 3.1E differ in their connectivity, in the mean length of the fibers, and in the extent of alignment in the horizontal direction. To study network behavior in a more controlled and systematic manner, we use a second approach that consists of using "idealized" stress fiber networks as depicted in figures 3.1C and 3.1F. Each of these two networks represents a monolayer whose cells are all identical. Each cell in the monolayer is represented by a hexagonal structure of 25 μm–long stress fibers. In these networks, the angle α between two side stress fibers (see figures 3.1C and 3.1F) determines the extent of isotropy or alignment of the network: $\alpha = 120°$ corresponds to the isotropic case (figure 3.1C) whereas $\alpha = 60°$ represents a network aligned in the horizontal direction (figure 3.1F).

All other dimensions and mechanical properties of individual stress fibers for the isotropic and aligned networks in both the real and idealized cases are assumed to be identical and are taken from the literature. These values are provided in Table 3.1.

3.2.2   Model of cellular adhesion to the substrate

Cells adhere to their substrates via focal adhesions, clusters of transmembrane integrin proteins and associated proteins that physically link the substrate to intracellular stress fibers (Choquet et al., 1997, Geiger et al., 2009). To overcome the simplification that we consider a purely two dimensional network, we assume that vertical stress

fibers of the typical height of a cell link the two dimensional stress fiber network to the adhesions, as examplified in figure 3.2A.
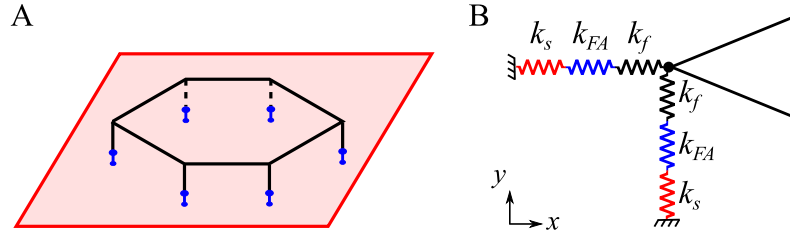
FIGURE 3.2: A. The 2D stress fiber network is attached to the elastic substrate (red in the figure) via other stress fibers (black vertical lines) and adhesive transmembrane proteins (blue). B. The intermediate stress fiber-adhesive protein-substrate complex is modeled as three springs in series that constrain the displacement of network nodes (black dot in the figure).

We model the substrate, the focal adhesions, and the intermediate stress fibers as springs of respective constant k_s, k_{FA} and k_f (figure 3.2B). The adhesion of the network is then modeled by attaching the nodes of the network to a zero-displacement surface via an element consisting of three springs whose overall spring constant k_{adh} is given as $1/k_{adh} = 1/k_s + 1/k_{FA} + 1/k_f$. At each node M of the network, the adhesion force exerted on the node is:

$$\mathbf{F}_{s \to M} = -k_{adh}\mathbf{w}_M, \tag{3.1}$$

where w_M is the displacement vector for node M.

3.2.3 Model of mechanical deformation of a stress fiber

As in Chapter 2 and in our previous work (Gouget et al., 2014, Hwang and Barakat, 2012, Hwang et al., 2012), we model each actin stress fiber as a uniformly prestressed viscoelastic filament of length L, cross sectional area A, second moment of area I, internal viscosity γ, elastic modulus E, and constant prestress σ_p. As represented in figure 3.3A, a stress fiber physically links together two nodes M_1 and M_2; these nodes may represent cell membrane proteins such as focal adhesions or cell–cell adhesion proteins, various intracellular sites, or linker proteins between two stress fibers.

Application of an external force to the stress fiber network leads to fiber displacement. As we have shown previously (Gouget et al., 2014, Hwang and Barakat, 2012), this displacement is governed by a balance between stress fiber inertia and the various forces acting on the fiber including the externally applied force, restoring forces due to fiber prestress as well as fiber elasticity, and damping forces due to fiber internal viscosity and cytoplasmic drag. As has been demonstrated elsewhere (Hwang and Barakat, 2012), the effects of both fiber inertia and cytoplasmic drag are negligible relative to the other
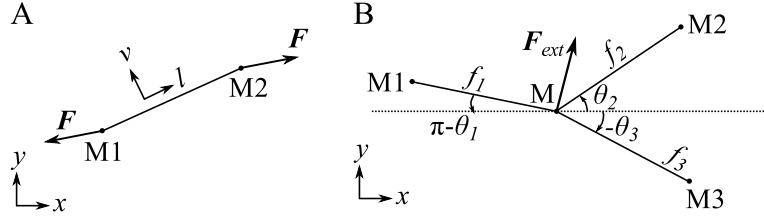
FIGURE 3.3: A. Example of a single stress fiber that links points M_1 and M_2 and that is subjected to an external force **F**. B. Example of a simple network where the node M is connected to nodes M_1, M_2, and M_3 and is subjected to a force **F**.

terms. Under these simplifications, it has been shown in Chapter 2 that application of an external force **F** to the ends of a stress fiber leads to a fiber deformation $\Delta w = w_{M_2} - w_{M_1}$ that is governed by the ordinary differential equations:

$$\frac{\sigma_p A}{L} \Delta w^v(t) + \frac{\gamma I}{L^3} \frac{d\Delta w^v(t)}{dt} = F^v, \tag{3.2a}$$

$$\frac{EA}{L} \Delta w^l(t) + \frac{\gamma A}{L} \frac{d\Delta w^l(t)}{dt} = F^l, \tag{3.2b}$$

which respectively describe the balance of forces in the directions transverse and longitudinal to the fiber. Here and in all that follows, the superscripts v and l refer to the components of a vector in the directions transverse and longitudinal to the fiber, respectively. Note that the resistance to transverse motion is due to a balance of moments that has been reduced to the present ordinary differential equations. Equations (3.2a) and (3.2b) are simplifications of partial differential equations of stress fiber motion and allow us to view a stress fiber as a two dimensional anisotropic Kelvin-Voigt viscoelastic body, whose resistance to deformation k_v and k_l in the transverse and longitudinal directions are given by:

$$k_v = \frac{\sigma_p A}{L}; \qquad k_l = \frac{EA}{L}, \tag{3.3}$$

and whose characteristic times of deformation τ_l and τ_v in the transverse and longitudinal directions are given by:

$$\tau_v = \frac{\gamma I}{\sigma_p A L^2}; \qquad \tau_l = \frac{\gamma}{E}. \tag{3.4}$$

This result is in good agreement with experimental observations on the mechanical behavior of stress fibers (Kumar et al., 2006).

3.2.4 Model of mechanical deformation of a network of stress fibers

We consider a network of stress fibers as the example stress fiber network shown in figure 3.3B. The mechanical and geometric characteristics of fiber fi are denoted by the subscript i; θ_i is the angle between the x-axis and the fiber. The deformation of each

fiber is governed by equations (3.2a) and (3.2b), and these equations are coupled at the network nodes, thus providing a system of ordinary differential equations that describes the displacements of the nodes of the system. We illustrate here the derivation for the simple case of the network represented in figure 3.3B. The derivation for the general case is available in Appendix 1 (section 3.6).

At node M in figure 3.3B, the force balance is:

$$\mathbf{F}_{f1\to M} + \mathbf{F}_{f2\to M} + \mathbf{F}_{f3\to M} + \mathbf{F} = \mathbf{0}, \tag{3.5}$$

where $\mathbf{F}_{fi\to M}, i = 1, 2, 3$ is the force exerted on M due to the deformation of the fiber fi and $\mathbf{F}$ is the external force applied at M. The external force includes both the ahesion force $\mathbf{F}_{s\to M}$ and any other source of external forces $\mathbf{F}_{ext}$ (e.g. applied force). A projection of the force balance in equation (3.5) along the $x-$ and $y-$ directions yield:

$$\sum_{i=1}^{3} \left(F_{fi\to M}^{l} \cos(\theta_i) - F_{fi\to M}^{v} \sin(\theta_i) \right) + F^x = 0, \tag{3.6a}$$

$$\sum_{i=1}^{3} \left(F_{fi\to M}^{l} \sin(\theta_i) + F_{fi\to M}^{v} \cos(\theta_i) \right) + F^y = 0. \tag{3.6b}$$

Substituting the relations (3.2a) and (3.2b) for $F_{fi\to M}^{l}$ and $F_{fi\to M}^{v}$ in equations (3.6a) and (3.6b) yields the following system of ordinary differential equations:

$$\begin{pmatrix} \sum_{i=1}^{3}\Gamma_i^{xx} & \sum_{i=1}^{3}\Gamma_i^{xy} & -\Gamma_1^{xx} & -\Gamma_1^{xy} & -\Gamma_2^{xx} & -\Gamma_2^{xy} & -\Gamma_3^{xx} & -\Gamma_3^{xy} \\ \sum_{i=1}^{3}\Gamma_i^{xy} & \sum_{i=1}^{3}\Gamma_i^{yy} & -\Gamma_1^{xy} & -\Gamma_1^{yy} & -\Gamma_2^{xy} & -\Gamma_2^{yy} & -\Gamma_3^{xy} & -\Gamma_3^{yy} \end{pmatrix} \frac{d}{dt}\mathbf{w} =$$

$$- \begin{pmatrix} \sum_{i=1}^{3}K_i^{xx} & \sum_{i=1}^{3}K_i^{xy} & -K_1^{xx} & -K_1^{xy} & -K_2^{xx} & -K_2^{xy} & -K_3^{xx} & -K_3^{xy} \\ \sum_{i=1}^{3}K_i^{xy} & \sum_{i=1}^{3}K_i^{yy} & -K_1^{xy} & -K_1^{yy} & -K_2^{xy} & -K_2^{yy} & -K_3^{xy} & -K_3^{yy} \end{pmatrix} \mathbf{w} + \begin{pmatrix} F^x \\ F^y \end{pmatrix},$$

$$\tag{3.7a}$$

where $\mathbf{w}$ is the displacement vector:

$$\mathbf{w} = \begin{pmatrix} w_M^x & w_M^y & w_{M_1}^x & w_{M_1}^y & w_{M_2}^x & w_{M_2}^y & w_{M_3}^x & w_{M_3}^y \end{pmatrix}, \tag{3.7b}$$

K_i^{xx}, K_i^{xy} and K_i^{yy} refer to the different contributions to the rigidity of the system:

$$K_i^{xx} = \frac{E_i A_i}{L_i} \cos^2(\theta_i) + \frac{\sigma_{p_i} A_i}{L_i} \sin^2(\theta_i),$$

$$K_i^{xy} = \left(\frac{E_i A_i}{L_i} - \frac{\sigma_{p_i} A_i}{L_i} \right) \cos(\theta_i) \sin(\theta_i),$$

$$K_i^{yy} = \frac{E_i A_i}{L_i} \sin^2(\theta_i) + \frac{\sigma_{p_i} A_i}{L_i} \cos^2(\theta_i), \tag{3.7c}$$

and Γ_i^{xx}, Γ_i^{xy} and Γ_i^{yy} are the contributions to the viscosity of the system:

$$\Gamma_i^{xx} = \frac{\gamma_i A_i}{L_i} \cos^2(\theta_i) + \frac{\gamma_i I_i}{L_i^3} \sin^2(\theta_i),$$

$$\Gamma_i^{xy} = \left(\frac{\gamma_i A_i}{L_i} - \frac{\gamma_i I_i}{L_i^3} \right) \cos(\theta_i) \sin(\theta_i),$$

$$\Gamma_i^{yy} = \frac{\gamma_i A_i}{L_i} \sin^2(\theta_i) + \frac{\gamma_i I_i}{L_i^3} \cos^2(\theta_i). \tag{3.7d}$$

Similar force balances can be performed for nodes M_1, M_2 and M_3. Adding the resulting equations to the system of equations (3.7a) yields the global system of equations describing the network of fibers. The generalization of this result to any network of stress fibers yields the system of equations:

$$\mathbf{\Gamma} \frac{d}{dt} \mathbf{w} = -\mathbf{K}\mathbf{w} - k_{adh}\mathbf{w} + \mathbf{F}_{ext}, \tag{3.8}$$

where $\mathbf{w}$ is the vector of the displacements of the nodes of the system, $\mathbf{F}$ is the vector of the external forces applied to the nodes of the system, $\mathbf{\Gamma}$ is the damping matrix and $\mathbf{K}$ is the stiffness matrix. The components of the stiffness and damping matrices are a combination of the contributions given in equations (3.7c) and (3.7d), respectively. Solution of equation (3.8) provides the displacements of the nodes of the system. Details of the resolution method are given in Appendix 2 (section 3.7).

The strain ϵ of a stress fiber f of length L_f that links points M_1 and M_2 is:

$$\epsilon(t, f) = \frac{\mathbf{w}_{M_2} - \mathbf{w}_{M_1}}{L_f} \tag{3.9a}$$

We will also consider the components of the strain longitudinal and transverse to the fiber, ϵ_l and ϵ_v:

$$\epsilon_l(t, f) = \epsilon_x \cos(\theta_f) + \epsilon_y \sin(\theta_f), \tag{3.9b}$$

$$\epsilon_v(t, f) = -\epsilon_x \sin(\theta_f) + \epsilon_y \cos(\theta_f). \tag{3.9c}$$

3.2.5 Parameter values

We consider that all stress fibers in a network have the same internal viscosity, elastic modulus, prestress, cross-sectional area, and second moment of area, and we take these values from literature (Table 3.1).

TABLE 3.1: Stress fiber mechanical and geometrical parameter values.

	Symbol	Unit	Value	Source
Radius	R	m	10^{-7}	Deguchi et al. 2006
				Kumar et al. 2006
Cross-sectional area	A	m^2	$\pi 10^{-14}$	$A = \pi R^2$
Second moment of area	I	m^4	$\pi/4 \; 10^{-28}$	$I = \int r^2 dA$
Stiffness	E	Pa	10^6	Deguchi et al. 2006
				Lu et al. 2008
Prestress	σ_p	Pa	$3 \; 10^5$	Deguchi et al. 2006
Internal viscosity	γ	Pa sec	$4 \; 10^6$	Kumar et al. 2006

Drawing the real networks (figures 3.1B and 3.1E) from the endothelial cell images (figures 3.1A and 3.1D) as described in section 3.2.1 yields a set of fibers of different lengths L. The mean fiber length is $< L >= 21$ μm for the isotropic network and $< L >= 29$ μm for the aligned network. To isolate the effect of length from the effect of other parameters, we rescale the fiber lengths in the real networks to obtain mean fiber lengths $< L >= 21$ μm, $< L >= 25$ μm or $< L >= 29$ μm. In the idealized networks (figures 3.1C and 3.1F), all the fibers have the same length, and we will investigate networks with fibers of length $L = 21$ μm, $L = 25$ μm or $L = 29$ μm.

The global adhesion spring constant k_{adh} is driven by the softest of its three spring elements. The spring constant associated with protein stiffness is typically greater than 1 Nm^{-1} (Jin et al., 2004, Schwarz et al., 2006). Displacement w of an adhesion induces a force on the substrate that scales as $F = AE_s w/L = k_{adh} w$, where E_s is the stiffness of the substrate, L is a characteristic length of deformation, and A is the area of force application. Hence, $k_s = \frac{AE_s}{L}$. The characteristic length is the distance between two points of force application, i.e. the mean fiber length. For a very rigid substrate with a stiffness on the order of a gigapascal, characteristic of plastic or glass, $k_s \sim 1$ Nm^{-1}, whereas for a tissue or a gel with a stiffness of a hundred kilopascals that more closely mimics physiological conditions (Engler et al., 2006), $k_s \sim 10^{-4}$ Nm^{-1}. The 2D motion of the network yields a transverse deformation of the fibers that link the network to the adhesions. According to equation (3.2b), this transverse motion is associated with a spring constant $k_f = \frac{\sigma_p A}{L} \sim 10^{-3}$ Nm^{-1}, for a cell height $h \sim 5$ μm (Liu et al., 1994). Consequently, on a very stiff substrate such as glass or plastic, the adhesion

spring constant is $k_{adh} \sim k_f \sim 10^{-3}$ Nm^{-1} whereas on a soft substrate, it is driven by the substrate stiffness and $k_{adh} \sim k_s \sim 10^{-4}$ Nm^{-1}.

We normalize the concept of isotropy of a network by defining the isotropy index q. For an idealized network:

$$q = \frac{\alpha}{\alpha_{isotropy}}, \tag{3.10}$$

where $\alpha_{isotropy}$ is the angle at which the network reaches its maximum isotropy, for the network of hexagons, $\alpha_{isotropy} = 120°$. Thus, $q = 1$ indicates an isotropic network, and $q = 0$ denotes a perfectly aligned network. We consider $q = 1$ for the real isotropic network and $q = 0.1$ for the real aligned network.

The externally applied point force is exerted at a sufficiently central point (marked in red in figures 3.1B, 3.1C, 3.1E and 3.1F) and at an angle θ_{ext} with the x-axis. We consider both step and oscillatory forcing as can be applied experimentally:

$$\mathbf{F}_{ext} = F_0 \left(1 - e^{(-t/t_\epsilon)}\right) \left(\cos(\theta_{ext})\mathbf{e}_x + \sin(\theta_{ext})\mathbf{e}_y\right), \tag{3.11}$$

$$\mathbf{F}_{ext} = F_0/2 \left(c_1 \left(1 - e^{(-t/t_\epsilon)}\right) + c_2 \sin(\Omega t)\right) \left(\cos(\theta_{ext})\mathbf{e}_x + \sin(\theta_{ext})\mathbf{e}_y\right), \tag{3.12}$$

where Ω is the angular frequency of the oscillatory forcing, F_0 is the magnitude of the forcing, and t_ϵ is the time needed to enforce the constant forcing, $t_\epsilon << \tau_v$ and $t_\epsilon << \tau_l$. As in Chapter 2, the coefficients c_1 and c_2 drive the extent of reversing forcing. In the present study, we only consider non-reversing forcing, with $c_1 = 0.6$ and $c_2 = 0.4$. In accordance with experiments, we take $F_0 = 300$ pN (Gouget et al., 2014, Hu et al., 2004, Na et al., 2008, Wang and Ingber, 1994). However, given the linearity of the equations, the qualitative results do not depend on this value. Note that by virtue of the linearity of the system of equations (3.8), straightforward superposition would yield the mechanical response to a more complex stress.

3.3   Results

Upon application of a force to a point in the stress fiber network, the nodes at the junctions of the fibers move, inducing strain in the stress fibers. This is examplified in figure 3.4 which depicts the distributions of steady-state strain in isotropic and aligned idealized networks on either rigid or soft substrates in response to a constant point force of 300 pN applied in the vertical direction.

The results demonstrate that strains are larger in aligned networks (figures 3.4C and 3.4D) than in isotropic networks (figures 3.4A and 3.4B). Furthermore, strains are larger
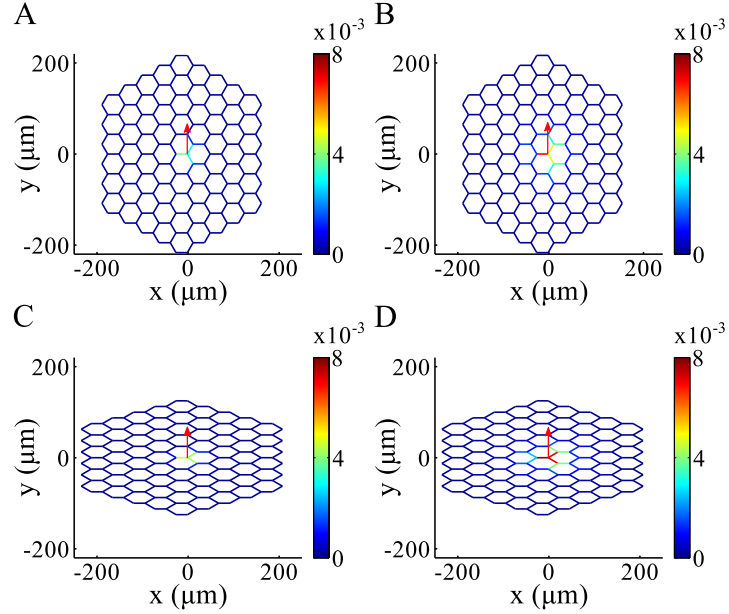
FIGURE 3.4: Magnitude of stress fiber strain, in an isotropic network, $q = 1$, on either a rigid ($k_{adh} = 10^{-3}$ Nm^{-1}, A) or a soft substrate ($k_{adh} = 10^{-4}$ Nm^{-1}, B) and in an aligned network, $q = 0.5$, on either a rigid ($k_{adh} = 10^{-3}$ Nm^{-1}, C) or a soft substrate ($k_{adh} = 10^{-4}$ Nm^{-1}, D). A constant force is applied along the vertical direction (red arrow), and the strain is taken at steady-state. The fiber length is 25 μm.

and propagate farther on softer than on more rigid substrates (figures 3.4A vs 3.4B and 3.4C vs 3.4D).

3.3.1 Steady-state strain around the point of force application

To more clearly illustrate the effects of network alignment, we plot different measures of strain near the site of force application, where most of the strain is concentrated, as a function of the isotropy index q (figure 3.5). To this end, we define the mean strain ϵ^0, the mean absolute longitudinal strain ϵ_l^0 and the mean absolute transverse strain ϵ_v^0 in the fibers in direct contact with the point of force application as follows:

$$\epsilon^0 = < ||\epsilon(t_\infty, f)|| >_{f|M_F \in f}, \tag{3.13a}$$

$$\epsilon_l^0 = < |\epsilon_l(t_\infty, f)| >_{f|M_F \in f}, \tag{3.13b}$$

$$\epsilon_v^0 = < |\epsilon_v(t_\infty, f)| >_{f|M_F \in f}, \tag{3.13c}$$

where M_F is the point of force application.

Consistent with the anisotropy of the resistance of the stress fiber to force (equation (3.3)) and the differences in fiber prestress and stiffness (Table 3.1), the longitudinal strain is about one third of the transverse strain (figures 3.5B and 3.5C). Consequently,
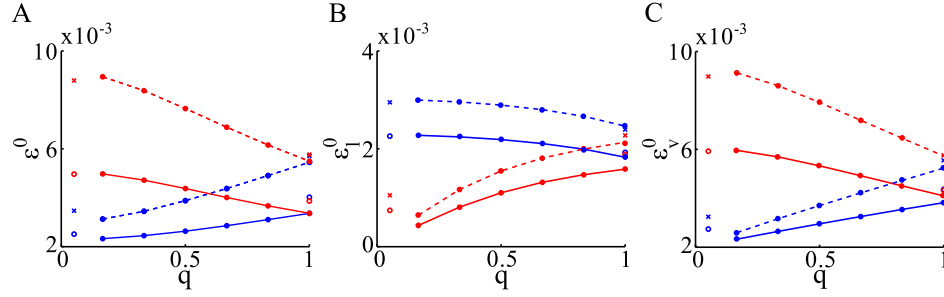
FIGURE 3.5: Magnitude (A), absolute longitudinal (B) and absolute transverse (C) steady-state strain in the fibers in direct contact with the point of force application as a function of the isotropy index q. A constant force is applied along either the x-axis (blue) or the y-axis (red) to an idealized hexagonal network ($k_{adh} = 10^{-3}$ Nm^{-1}: solid line, $k_{adh} = 10^{-4}$ Nm^{-1}: dashed line) or to a real network ($k_{adh} = 10^{-3}$ Nm^{-1}: circle, $k_{adh} = 10^{-4}$ Nm^{-1}: cross). Mean fiber length is 25 μm.

the amplitude of the strain is driven mainly by the transverse strain (figure 3.5A). Interestingly, the longitudinal and transverse strains exhibit a different dependence on network isotropy. When the force is applied along the x-axis (blue curves in figure 3.5), the transverse strain (and the overall mean strain since it is primarily driven by the transverse strain) increase with isotropy whereas the longitudinal strain decreases. Indeed, in an aligned network stimulated along the direction of alignment, the force is mainly applied in the longitudinal direction of the fibers, whereas when the isotropy of the network increases, force is split in the longitudinal and transverse directions of the fibers. The opposite is true for a force applied in the vertical direction (red curves in figure 3.5). Both the longitudinal and transverse strains are significantly larger when the adhesion to the substrate is softer ($k_{adh} = 10^{-4}$ Nm^{-1}: dashed lines and crosses vs $k_{adh} = 10^{-3}$ Nm^{-1}: solid lines and circles in figure 3.5). This significant effect of the rigidity of the adhesion is intuitive, as a very stiff substrate would prevent any motion of the nodes and nullify any strain. All the observations above hold for both idealized networks (solid and dashed lines in figure 3.5) and real networks (circles and crosses), which suggests that from the standpoint of strain propagation, the idealized networks are a reasonable representation of real cellular stress fiber networks.

The conclusions above are fairly robust. For instance, changing the length of the fibers in the network only changed the strain by a few percent (data not shown). Changing the number of cells in the idealized networks also left the results largely unchanged. Thus, it appears that the main determinants of strain elicited by a force are the rigidity of the adhesion and the extent of alignment of the network, whereas the length of the fibers and the connectivity of the network have negligible effects.

3.3.2 Strain propagation in the stress fiber networks

The results of figure 3.4 raise the question of how far within the monolayer a force applied at a point elicits non-negligible strains. We define N_f as the number of fibers separating the point of force application from the furthest fiber that undergoes more than 10% of the maximum strain:

$$N_f = \max \left(n_f \mid \epsilon(t_\infty, f) > 1/10\epsilon_{max} \right) , \qquad (3.14)$$

where n_f is the number of fibers between fiber f and the point of force application, and ϵ_{max} is the maximum strain. The strain ϵ can be the magnitude of the total strain, the absolute longitudinal strain or the absolute transverse strain.

Figure 3.6 depicts N_f as a function of the isotropy index q for both idealized and real stress fiber networks on both soft and rigid substrates and for force application either along or orthogonal to the direction of network alignment. The jagged (or bumpy) nature of the resulting curves is attributable to the fact that the values of N_f are discrete. The transverse strain and the total strain appear to propagate further when the force is applied in the x-direction (blue data in figures 3.6A and 3.6C) than when it is applied in the y-direction (red data), a result of limited relevance given the small levels of associated strain (figure 3.5). Strain tends to be transmitted further in aligned idealized networks than in isotropic idealized networks (solid and dashed curves in figure 3.6), but the difference is not significant ($\Delta N_f \sim 1$ fiber), and the same trend is not consistently observed in the real networks (circles and crosses in figure 3.6). This may lead one to postulate that the connectivity of the network is as or even more important than its alignment in determining the transmission of the mechanical signal. In contrast, increasing the value of k_{adh} significantly decreases the distance of transmission of the strain in both idealized (dashed vs solid curves in figure 3.6) and real (crosses vs circles in figure 3.6) networks. The mean length of the fibers has no or very little effect on the results (data not shown). The effect of the monolayer size was also tested by increasing the number of cells of the idealized networks and was determined to have no impact on the results.

3.3.3 Direction of maxmial strain

Figure 3.7 provides information on the preferred direction of strain transmission relative to the direction of the applied external force in isotropic (figures 3.7A and 3.7B) and aligned (figures 3.7C and 3.7D) networks. In each case, the strain in the direction θ, $E(\theta)$, is defined as the average strain in the angular slice, $S_{[\theta-d\theta:\theta+d\theta]}$, between $\theta - d\theta$
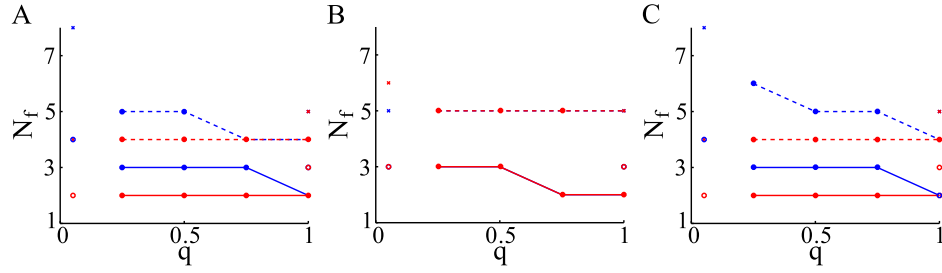
FIGURE 3.6: Maximal number of fibers N_f between the point of force application and the fibers undergoing more than 10% of the maximal strain (A), absolute longitudinal strain (B), and absolute transverse strain (C) as a function of the isotropy index q. The external force is applied either along the x-axis (blue) or along the y-axis (red) to an idealized hexagonal network ($k_{adh} = 10^{-3}$ Nm^{-1}: solid line, $k_{adh} = 10^{-4}$ Nm^{-1}: dashed line) or to a real network ($k_{adh} = 10^{-3}$ Nm^{-1}: circle, $k_{adh} = 10^{-4}$ Nm^{-1}: cross). Mean fiber length is 25 μm.

and $\theta + d\theta$ around the point of force application:

$$E(\theta) = < \epsilon \left(t_\infty, f \in S_{[\theta - d\theta : \theta + d\theta]} \right) > . \tag{3.15}$$

This equation holds for the magnitude of the total strain, the longitudinal strain, and the transverse strain. The preferred direction of strain transmission is then the angle θ_{max} where the function E reaches its maximum.
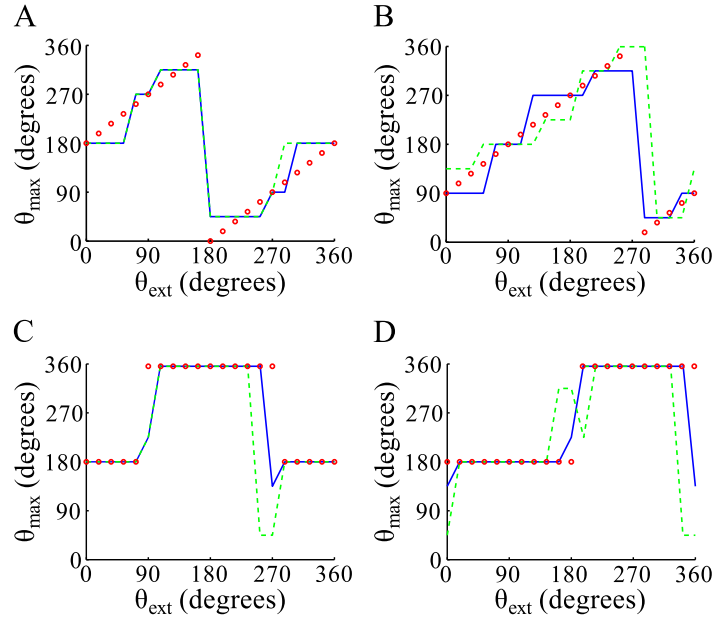
FIGURE 3.7: Angle θ_{max} at which the maximal longitudinal (A, C) and transverse (B, D) strain is reached as a function of the direction of the external force, θ_{ext}, in isotropic (A, B) and aligned networks (C, D). Solid blue line: hexagonal networks with either $q = 1$ (A,B) or $q = 0.25$ (C,D), dashed green line: real networks, red circles: fit. Mean fiber length is 25 μm.

Figure 3.7 shows the angle θ_{max} as a function of the angle θ_{ext} between the x-axis and the applied force. Two distinct behaviors appear depending on the isotropy of the network. In both real and idealized isotropic networks (figures 3.7A and 3.7B), the preferred direction of strain transmission depends linearly on the external force angle θ_{ext}. The fibers undergoing maximal longitudinal tension (positive strain) are at an angle $\theta = 180° + \theta_{ext}[360°]$ (figure 3.7A) and the fibers undergoing maximal transverse tension are in the direction $\theta = 90° + \theta_{ext}[360°]$ (figure 3.7B). On the other hand, in aligned networks, the maximal longitudinal tension is in the direction $\theta = 180°$ when the force has a positive x-component ($\theta_{ext} < 90°$ or $\theta_{ext} > 270°$), and in the direction $\theta = 360°$ otherwise. Thus, in isotropic networks, the preferred direction of strain transmission is linearly determined by the external force direction, whereas in aligned networks, it only depends on the general direction of the force. Interestingly, these results are very similar in real and idealized networks (dashed green line and solid blue line in figure 3.7), and they do not depend on adhesion rigidity, mean fiber length, or monolayer size.

3.3.4 Dynamics of strain development

To study the dynamics of the mechanical response of cellular monolayers, figure 3.8 depicts the charatteristic time of the response, T, as a function of the index of isotropy, q. For the constant force given by equation (3.11), the characteristic response time T is defined such that:

$$\sum_f \epsilon\,(T, f) = \frac{1}{\sqrt{2}} \max_t \left(\sum_f \epsilon\,(t, f) \right), \tag{3.16a}$$

where ϵ is either the magnitude of the strain, the absolute axial strain, or the absolute transverse strain. Equivalently, for an oscillatory force (equation (3.12)), T is defined as the cutoff period such that:

$$\sum_f A\,(\epsilon\,(F_T, f)) = \frac{1}{\sqrt{2}} \max_\tau \left(A \left(\sum_f \epsilon\,(F_\tau, f) \right) \right), \tag{3.16b}$$

where F_τ is a forcing of pulsation $\Omega = 2\pi/\tau$ and A is the amplitude function. Figures 3.8B and 3.8C show very different dynamics associated with longitudinal and transverse strain, $T \sim 10$ s and $T \sim 10^{-4}$ s, respectively. These results are consistent with equations (3.2) and (3.4), which predict anisotropic dynamics with $\tau_l \sim 4$ s and $\tau_v \sim 10^{-4}$ s for the parameter values from Table 3.1 and for a mean fiber length $L = 25\ \mu$m. The expression for $\tau_v \sim 10^{-4}$ s (equation (3.4)) predicts the dynamics to be fiber length-dependent, and indeed increasing the mean fiber length from 21 μm to 29 μm decreases the characteristic time associated with the transverse motion of the fiber, though withtout changing its order of magnitude. In real networks, the dispersion of fiber lengths is associated with
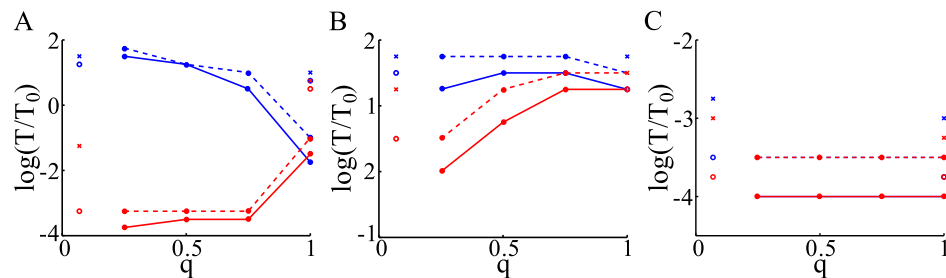
FIGURE 3.8: Characteristic time T of the development of the strain magnitude (A), absolute longitudinal value (B) and absolute transverse value (C) as a function of the isotropy index q. T_0 is a reference time, $T_0 = 1$ s. The external force is applied either along the x-axis (blue) or along the y-axis (red) to an idealized hexagonal network ($k_{adh} = 10^{-3}$ Nm^{-1}: solid line, $k_{adh} = 10^{-4}$ Nm^{-1}: dashed line) or to a real network ($k_{adh} = 10^{-3}$ Nm^{-1}: circle, $k_{adh} = 10^{-4}$ Nm^{-1}: cross). Mean fiber length is 25 μm.

non-uniform characteristic times through the network, and the global characteristic time is limited by the slower dynamics. This explains the relative differences observed between the dynamics of real networks (circles and crosses in figure 3.8) and those of idealized networks (solid and dashed curves in figure 3.8). Despite these differences, real and idealized networks show a similar dependence on network alignment. The dynamics of transverse strain transmission do not depend significantly on the external force direction or the index of isotropy (figure 3.8C), whereas the longitudinal strain is transmitted faster when the force is applied in the vertical direction (red curve in figure 3.8B). In this latter case, the networks are mainly forced in the transverse direction of the fiber, and the resulting high transverse strain induces a small rapid axial strain. The overall dynamics of the magnitude of total strain (figure 3.8C) are highly dependent on force direction and isotropy of the network. When the network is aligned and stimulated in the y-direction, the strain magnitude is driven by the transverse strain and its dynamics are rapid (red data in 3.8A), whereas a force in the x-direction yields mostly slow longitudinal strain (blue data). When the isotropy increases, the fibers are strained in both their longitudinal and transverse directions, and the dynamics of the magnitude of the strain converge towards a force direction-independent value. Decreasing the adhesion rigidity k_{adh} tends to slow down the dynamics of strain transmission (dashed curves and crosses vs solid curves and circles in figure 3.8); however, this effect is not very pronounced. The dynamics of strain transmission do not depend on the number of cells in the idealized networks (data not shown).

3.4   Discussion

3.4.1   Comparison with experimental results

Experiments on the twisting of magnetic beads coated with cell-surface adhesive ligands have demonstrated a bead displacement of ~ 0.1 μm in response to a twisting force of ~ 100 pN (Feneberg et al., 2004, Karcher et al., 2003). Comparatively, our model yields a displacement of the node at which the force is applied of approximately $\epsilon L = 5.10^{-3} \times 25 = 0.125$ μm. Thus, the displacements predicted by our model are of the same order of magnitude as the experimental data. Our model also predicts anisotropy of the strain with respect to force direction (figures 3.5 and 3.7), a dependence observed experimentally and attributed to the actin cytoskeleton (Bausch et al., 1998, Karcher et al., 2003).

Our results show that strain is transmitted only two fibers away from the point of force application on a rigid substrate. Thus, only the cells in contact with the force feel non-negligible strain, a result in agreement with experimental results showing decay over a single cell length of the mechanical information in monolayers of cells cultured on a plastic substrate (Charras and Horton, 2002, Feneberg et al., 2004, Karcher et al., 2003). On a softer substrate, however, our model results suggest that the strain extends up to seven fibers, which corresponds to a few cells (figure 3.4), consistent with experiments on cells cultured on a gel substrate (Tambe et al., 2011).

Various experimental results have demonstrated the complex dynamics of the response of cells to mechanical stimulation. In particular, experiments on cellular monolayers show a mix of rapid dynamics on the order of a few milliseconds and slower dynamics on the order of a few seconds (Feneberg et al., 2004, Harris et al., 2012). Our model predicts these complex dynamics (figure 3.8). The mechanism underlying these dynamics is the anisotropy of the stress fiber mechanical behavior (equation (3.2)), which is due to the myosin-related prestress of these filaments. This mechanism is in good agreement with the dependence of the mechanical properties on both myosins and the intregrity of the actin cytoskeleton (Balland et al., 2006).

3.4.2   Effect of cellular alignment

Our results show that the magnitude of strain, the direction of maximal strain, and the dynamics of strain development are all dependent on the extent of cellular alignment in the monolayer (figure 3.5, 3.6 and 3.8A). Importantly, comparison of real to idealized networks shows that the trends observed are not due to the difference in connectivity of

the isotropic (figure 3.1A) or aligned (figure 3.1B) monolayers of cells. The effect of stress fiber mean length was also tested, but it only changed the results by a few percent, which is negligible compared to the effect of the isotropy index. Finally, a potential effect of the size of the portion of monolayer considered was ruled out by testing idealized networks of different sizes.

In arterial regions of branching and bifurcation where blood flow is disturbed, endothelial cells are generally round with isotropic cytoskeletal organization whereas in regions of undisturbed flow, endothelial cells are elongated and exhibit cellular alignment and cytoskeletal polarization in the flow direction (Flaherty et al., 1972, Malek et al., 1999, Wong et al., 1983). Previous studies have demonstrated that endothelial cell alignment leads to a reduction in the fluid mechanical shear stress gradients on the cell surface (Barbee et al., 1995, Charras and Horton, 2002) and that an increase in the mechanical stress triggers an increase in cell stiffness (Glogauer et al., 1997, Tagawa et al., 1997). In line with these observations, we have found that the magnitude of the total strain is smallest in aligned networks subjected to a force applied in the direction of alignment (figure 3.6A, blue data). On the other hand, our model predicts that in regions of disturbed flow where the force may change direction over a cardiac cycle, aligned networks undergo the highest strain when the force is orthogonal to the direction of alignment, whereas strain takes on a mean, force direction-independent value in isotropic networks. Furthermore, our model predicts that in aligned monolayers, transient or high frequency perturbations are cut off only if the force is applied in the direction of alignment. In regions of disturbed flow where perturbations are likely and force direction can change, isotropic networks offer a compromise.

Several models have been proposed to explain how endothelial cells polarize in response to shear stress, including a shear rate-dependent gradient of chemical cues around the cell (Shamloo et al., 2008) and shear stress-dependent activation of small GTPases at focal adhesions that triggers cytoskeletal remodeling (Li et al., 1999, Shyy and Chien, 2002). Our model shows that application of a force in a given direction to an isotropic monolayer of cells induces highly polarized stress fiber strain. In contrast, in aligned monolayers, the direction of the force only determines the sign of the strain.

3.4.3 Effect of the rigidity of adhesion to the substrate

Comparison of the magnitude of strain, extent of strain propagation, and dynamics of strain development for two values of the adhesion rigidity k_{adh} characteristic of very rigid substrates such as plastic or glass and soft substrates characteristic of in vivo or gel substrates showed significantly different results. In particular, propagation of strain to

neighboring cells was inhibited by increasing the value of k_{adh}, which is consistent with experimental observations (Feneberg et al., 2004, Karcher et al., 2003, Tambe et al., 2011). Substrate stiffness is thus a critical factor when studying the response of cellular monolayers to force.

3.4.4 Stress fiber strain as a potential link in the mechanotransduction chain

Several proteins, such as zyxin, have been shown to link to stress fibers with an affinity that depends on stress fiber stretch; thus, it has been suggested that these proteins' binding affinity to stress fibers is altered by tension (Colombelli et al., 2009, Sawada and Sheetz, 2002, Yoshigi et al., 2005). These results implicate stress fiber strain as a potential link in the mechanotransduction chain. The stress fiber strains predicted by our model (figure 3.5) are compatible with those needed to trigger biological pathways (Charras and Horton, 2002). If strain is directly transduced into a biological response, then our results on dynamics, propagation and polarization of strain may explain several key phenomena as discussed above.

3.5 Conclusions

We have developed a theoretical model of a monolayer of cells that consists of a network of stress fibers adhering to the substrate, and we have studied the response of this network to a localized forcing. Albeit minimalist, this model provided results on the extent of intracellular displacements and strains, as well as on the transmission of strain to neighboring cells and on the dynamics of the response to force that are consistent with several experimental results. The present results suggest a key role for stress fiber networks in the mechanical response of cellular monolayers to force.

The present results also suggest that mimization of strain and of variations in strain might drive stress fiber alignment and thus the cell morphology. In regions of disturbed flow where fast perturbations and changes in force direction occur, strain is averaged and perturbations are cut off in an isotropic stress fiber topology. Our results also show a polarization of isotropic networks that depends linearly on the direction of the applied force. These results are all the more interesting in view of the observation that the stress fiber strain is sufficient to elicit a biological response.

Future studies may focus on adding the other cell constituents, including the cell membrane, the cytoplasm, and other cytoskeletal filaments to test their effects on the mechanical response of the monolayer.

3.6 Appendix 1

We consider the general case of a network of n fibers and m nodes (for example, for the network in figure 3.3B, $n = 3$ fibers and $m = 4$ nodes). At a node M, the following balance of forces must be enforced:

$$\sum_{i|M \in f_i} \mathbf{F}_{f_i \to M} + \mathbf{F}_{ext \to M} = \mathbf{0}, \tag{A1.1}$$

where $\mathbf{F}_{ext \to M}$ is an external force applied to node M, and $\mathbf{F}_{f_i \to M}$ is the force applied to M due to the deformation of fiber f_i, of which M is a node ($M \in f_i$). Applying ODEs (3.2a) and (3.2b) to the fiber f_i yields the components of $\mathbf{F}_{f_i \to M}$ in the directions transverse and longitudinal to the fiber, $F^v_{f_i \to M}$ and $F^l_{f_i \to M}$:

$$F^v_{f_i \to M} = \frac{\sigma_{p_i} A_i}{L_i}(w^v_{M_{f_i}} - w^v_M) + \frac{\gamma_i I_i}{L_i^3}\frac{d}{dt}(w^v_{M_{f_i}} - w^v_M), \tag{A1.2a}$$

$$F^l_{f_i \to M} = \frac{E_i A_i}{L_i}(w^v_{M_{f_i}} - w^v_M) + \frac{\gamma_i A_i}{L_i}\frac{d}{dt}(w^v_{M_{f_i}} - w^v_M), \tag{A1.2b}$$

where w^l_M and w^v_M are the displacements of node M in the directions longitudinal and transverse to the fiber, and $w^l_{M_{f_i}}$ and $w^v_{M_{f_i}}$ are the displacements of the other node M_{f_i} to which the fiber f_i is linked. For example, in figure 3.3B, $M_{f_1} = M_1$.

Let θ_i be the angle between the fiber f_i and the x-axis; we can then rewrite equations (A1.2a) and (A1.2b) to cast $\mathbf{F}_{f_i \to M}$ in the Cartesian coordinate system:

$$\begin{pmatrix} F^x_{f_i \to M} \\ F^y_{f_i \to M} \end{pmatrix} = K_{f_i,M} \begin{pmatrix} w^x_{M_{f_i}} - w^x_M \\ w^y_{M_{f_i}} - w^y_M \end{pmatrix} + \Gamma_{f_i,M}\frac{d}{dt}\begin{pmatrix} w^x_{M_{f_i}} - w^x_M \\ w^y_{M_{f_i}} - w^y_M \end{pmatrix}, \tag{A1.3a}$$

where

$$K_{f_i,M} = \begin{pmatrix} \frac{\sigma_{p_i} A_i}{L_i}\cos^2(\theta_i) + \frac{E_i A_i}{L_i}\sin^2(\theta_i) & \left(\frac{\sigma_{p_i} A_i}{L_i} - \frac{E_i A_i}{L_i}\right)\cos(\theta_i)\sin(\theta_i) \\ \left(\frac{\sigma_{p_i} A_i}{L_i} - \frac{E_i A_i}{L_i}\right)\cos(\theta_i)\sin(\theta_i) & \frac{\sigma_{p_i} A_i}{L_i}\sin^2(\theta_i) + \frac{E_i A_i}{L_i}\cos^2(\theta_i) \end{pmatrix}, \tag{A1.3b}$$

and

$$\Gamma_{f_i,M} = \begin{pmatrix} \frac{\gamma_i I_i}{L_i^3}\cos^2(\theta_i) + \frac{\gamma_i A_i}{L_i}\sin^2(\theta_i) & \left(\frac{\gamma_i I_i}{L_i^3} - \frac{\gamma_i A_i}{L_i}\right)\cos(\theta_i)\sin(\theta_i) \\ \left(\frac{\gamma_i I_i}{L_i^3} - \frac{\gamma_i A_i}{L_i}\right)\cos(\theta_i)\sin(\theta_i) & \frac{\gamma_i I_i}{L_i^3}\sin^2(\theta_i) + \frac{\gamma_i A_i}{L_i}\cos^2(\theta_i) \end{pmatrix}. \tag{A1.3c}$$

Using expression (A1.3a) in the force balance (A1.1) yields:

$$\Gamma_M \frac{d\mathbf{w}}{dt} = -K_M \mathbf{w} + \mathbf{F}_{ext \to M}, \tag{A1.4a}$$

where $\mathbf{w}$ is a column vector containing the displacements of the moving nodes:

$$\mathbf{w} = \begin{pmatrix} w_{M_1}^x & w_{M_1}^y & \dots & w_M^x & w_M^y & \dots & w_{M_m}^x & w_{M_m}^y \end{pmatrix}^T, \tag{A1.4b}$$

$\mathbf{F}_{ext \to M}$ is the external force vector applied at M:

$$\mathbf{F}_{ext \to M} = \begin{pmatrix} F_{ext \to M}^x & F_{ext \to M}^y \end{pmatrix}^T, \tag{A1.4c}$$

and K_M and Γ_M are respectively the stiffness and damping matrices associated with the balance of force at node M:

$$K_M = \left(\begin{cases} -K_{f_i,M} & \text{if } \exists f_i | M_1 \& M \in f_i \\ 0 & \text{otherwise} \end{cases} \dots \sum_{f_i | M \in f_i} K_{f_i,M} \dots \begin{cases} -K_{f_i,M} & \text{if } \exists f_i | M \& M_m \in f_i \\ 0 & \text{otherwise} \end{cases} \right),$$

$$\tag{A1.4d}$$

$$\Gamma_M = \left(\begin{cases} -\Gamma_{f_i,M} & \text{if } \exists f_i | M_1 \& M \in f_i \\ 0 & \text{otherwise} \end{cases} \dots \sum_{f_i | M \in f_i} \Gamma_{f_i,M} \dots \begin{cases} -\Gamma_{f_i,M} & \text{if } \exists f_i | M \& M_m \in f_i \\ 0 & \text{otherwise} \end{cases} \right).$$

$$\tag{A1.4e}$$

Note that a node M_μ is involved in the force balance at M only if it is linked to M by a fiber ($\exists f_i \mid M \& M_\mu \in f_i$). Equations (A1.4) enforce the force balance at the moving node M. Repeating the same analysis for every moving node yields a system of ODEs that describes the global equilibrium of the system:

$$\Gamma \frac{d\mathbf{w}}{dt} = -K\mathbf{w} + \mathbf{F}, \tag{A1.5a}$$

with

$$K = \begin{pmatrix} K_{M_1} \\ \dots \\ K_M \\ \dots \\ K_{M_m} \end{pmatrix}, \quad \Gamma = \begin{pmatrix} \Gamma_{M_1} \\ \dots \\ \Gamma_M \\ \dots \\ \Gamma_{M_m} \end{pmatrix}, \quad \text{and} \quad F = \begin{pmatrix} F_{ext \to M_1}^x \\ F_{ext \to M_1}^y \\ \dots \\ F_{ext \to M}^x \\ F_{ext \to M}^y \\ \dots \\ F_{ext \to M_m}^x \\ F_{ext \to M_m}^y \end{pmatrix} \tag{A1.5b}$$

3.7 Appendix 2

Adaptation of equation (3.8) for resolution

The equation of deformation of a mechanical structure provided by the balance of external and interal forces yield the deformation of the structure up to a rigid body rotation or tranlation. Thus, full resolution of the equation requires to prescribe the displacement of some points of the structure. In our model, the translation and rotation of the network as a whole are prevented by the adhesion of the nodes to the substrate, which yields the term $-k_{adh}\mathbf{w}$ in equation (3.8). Thus, a "corrected" stiffness matrix can be defined, that includes the stiffness matrix derived from the mechanical properties of the network and the adhesion rigidity, i.e.:

$$\mathbf{K}' = \mathbf{K} - k_{adh}\mathbf{Id}, \tag{A2.1}$$

where $\mathbf{Id}$ is the identity matrix of the size of $\mathbf{K}$. Whereas $\mathbf{K}$ is singular, $\mathbf{K}'$ is not and takes into account the constraint on node displacements.

As $\mathbf{K}$, the damping matrix $\mathbf{\Gamma}$ is singular, because the constraint on node displacements imposed by the adhesion to the substrate is not taken into account into $\mathbf{\Gamma}$. To solve this problem, we use the condition on the node displacements to modify $\mathbf{\Gamma}$. Indeed, the force of adhesion to the substrate and the applied force are both external force that must be balanced:

$$\sum_{i=1}^{m} k_{adh}\mathbf{w}_{M_i} = \mathbf{F}_{ext}, \tag{A2.2}$$

where, as above, m is the number of nodes of the network and M_i is the i-th node. The displacement of one node of the system can be expressed as a function of the applied force $\mathbf{F}_{ext}$. For instance, $\mathbf{w}_{M_1}$ can be written as:

$$\mathbf{w}_{M_1} = \frac{1}{k_{adh}}\mathbf{F}f(t) - \sum_{i=2}^{m} k_{adh}\mathbf{w}_{M_i}, \tag{A2.3a}$$

and the time derivative of $\mathbf{w}_{M_1}$ is given by:

$$\frac{d\mathbf{w}_{M_1}}{dt} = \frac{1}{k_{adh}}\mathbf{F}f'(t) - \sum_{i=2}^{m} \frac{d\mathbf{w}_{M_i}}{dt}, \tag{A2.3b}$$

where f describes the time evolution of $\mathbf{F}_{ext}$, $\mathbf{F}_{ext} \equiv \mathbf{F} f(t)$. We use equation (A2.3b) to rewrite equation (3.8) without using $\mathbf{w}_{M_1}$:

$$\left[\mathbf{\Gamma} \frac{d\mathbf{w}}{dt} \right]_{i,i\geq 2} = \sum_{j=2}^{m} (\mathbf{\Gamma}_{i,2j-1} - \mathbf{\Gamma}_{i,1}) \frac{dw_{M_j}^x}{dt} + \sum_{j=2}^{m} (\mathbf{\Gamma}_{i,2j} - \mathbf{\Gamma}_{i,2}) \frac{dw_{M_j}^y}{dt}$$
$$+ \frac{\mathbf{\Gamma}_{i,1}}{k_{adh}} F^x f'(t) + \frac{\mathbf{\Gamma}_{i,2}}{k_{adh}} F^y f'(t). \tag{A2.4}$$

The two first columns and lines of the damping matrix Γ are not needed anymore as the contributions of M_1 to the system have been distributed. Therefore, we define a new square matrix $\tilde{\mathbf{\Gamma}}$, of size $2m - 2$, as:

$$\tilde{\mathbf{\Gamma}}_{i,2j} = \mathbf{\Gamma}_{i+2,2j+2} - \mathbf{\Gamma}_{i+2,2}, \tag{A2.5a}$$

$$\tilde{\mathbf{\Gamma}}_{i,2j-1} = \mathbf{\Gamma}_{i+2,2j+1} - \mathbf{\Gamma}_{i+2,1}, \tag{A2.5b}$$

where $i \in [1, 2m - 2]$ and $j \in [1, m - 1]$. We also define the vector $\mathbf{R}_{\mathbf{\Gamma}}$ of size $2m - 1$ that corresponds to the remainder term in equation (A2.4), i.e.:

$$\mathbf{R}_{\mathbf{\Gamma} i} = \frac{\mathbf{\Gamma}_{i+2,1}}{k_{adh}} F^x + \frac{\mathbf{\Gamma}_{i+2,2}}{k_{adh}} dF^y. \tag{A2.5c}$$

In order to keep the size homogeneity in the system of equations (3.8), similar modifications are done on the matrix $\mathbf{K}'$, and we define the $(2m - 2) \times (2m - 2)$ matrix $\tilde{\mathbf{K}}$ as:

$$\tilde{\mathbf{K}}_{i,2j} = \mathbf{K}'_{i+2,2j+2} - \mathbf{K}'_{i+2,2}, \tag{A2.6a}$$

$$\tilde{\mathbf{K}}_{i,2j-1} = \mathbf{K}'_{i+2,2j+1} - \mathbf{K}'_{i+2,1}, \tag{A2.6b}$$

where $i \in [1, 2m - 2]$ and $j \in [1, m - 1]$, and the vector $\mathbf{R}_{\mathbf{K}}$ of size $2m - 1$ as:

$$\mathbf{R}_{\mathbf{K} i} = \frac{\mathbf{K}'_{i+2,1}}{k_{adh}} F^x + \frac{\mathbf{K}_{i+2,2}}{k_{adh}} F^y. \tag{A2.6c}$$

Substitution of the stiffness and damping matrices by these expressions in equation (3.8) yield:

$$\tilde{\mathbf{\Gamma}} \frac{d}{dt} \tilde{\mathbf{w}} = -\tilde{\mathbf{K}} \tilde{\mathbf{w}} + \left(\tilde{\mathbf{F}} - \mathbf{R}_{\mathbf{K}} \right) f(t) - \mathbf{R}_{\mathbf{\Gamma}} f'(t), \tag{A2.7}$$

where $\tilde{\mathbf{w}} = \begin{pmatrix} w_{M_2}^x & w_{M_2}^y & ... & w_{M_m}^x & w_{M_m}^y \end{pmatrix}^T$ and $\tilde{\mathbf{F}} f(t) = \begin{pmatrix} F_{ext \to M_2}^x & F_{ext \to M_2}^y & ... & F_{ext \to M_m}^x & F_{ext \to M_m}^y \end{pmatrix}^T$. The displacement of node M_1 is then obtained using equation (A2.3a).

Analytic solution

In the case of a step force as given by equation (3.11), the system of equations (A2.7) yields:

$$\tilde{\boldsymbol{\Gamma}}\frac{d}{dt}\tilde{\mathbf{w}} = -\tilde{\mathbf{K}}\tilde{\mathbf{w}} + \left(\tilde{\mathbf{F}} - \mathbf{R_K}\right) + \left(-\tilde{\mathbf{F}} + \mathbf{R_K} - \frac{1}{t_\epsilon}\mathbf{R_\Gamma}\right)e^{(-t/t_\epsilon)}, \qquad \text{(A2.8)}$$

whose analytical solution is:

$$\tilde{\mathbf{w}} = \left[-\tilde{\mathbf{K}}^{-1}\left(\tilde{\mathbf{F}} - \mathbf{R_K}\right) + \left(\frac{1}{t_\epsilon}\tilde{\boldsymbol{\Gamma}} - \tilde{\mathbf{K}}\right)^{-1}\left(-\tilde{\mathbf{F}} + \mathbf{R_K} - \frac{1}{t_\epsilon}\mathbf{R_\Gamma}\right)\right]\exp\left(-\tilde{\boldsymbol{\Gamma}}^{-1}\tilde{\mathbf{K}}t\right)$$

$$+ \tilde{\mathbf{K}}^{-1}\left(\tilde{\mathbf{F}} - \mathbf{R_K}\right) - \left(\frac{1}{t_\epsilon}\tilde{\boldsymbol{\Gamma}} - \tilde{\mathbf{K}}\right)^{-1}\left(-\tilde{\mathbf{F}} + \mathbf{R_K} - \frac{1}{t_\epsilon}\mathbf{R_\Gamma}\right)\exp\left(-t/t_\epsilon\right). \qquad \text{(A2.9)}$$

In the case of an oscillatory force as given by equation (3.11), the system of equations (A2.7) yields:

$$\tilde{\boldsymbol{\Gamma}}\frac{d}{dt}\tilde{\mathbf{w}} = -\tilde{\mathbf{K}}\tilde{\mathbf{w}} + c_1\left(\tilde{\mathbf{F}} - \mathbf{R_K}\right) + c_1\left(-\tilde{\mathbf{F}} + \mathbf{R_K} - \frac{1}{t_\epsilon}\mathbf{R_\Gamma}\right)e^{(-t/t_\epsilon)} \qquad \text{(A2.10)}$$

$$+ \left(\tilde{\mathbf{F}} - \mathbf{R_K}\right)c_2\sin(\Omega t) - \mathbf{R_\Gamma}c_2\Omega\cos(\Omega t),$$

and the analytical solution is:

$$\tilde{\mathbf{w}} = A\exp\left(-\tilde{\boldsymbol{\Gamma}}^{-1}\tilde{\mathbf{K}}t\right)$$

$$+ c_1\tilde{\mathbf{K}}^{-1}\left(\tilde{\mathbf{F}} - \mathbf{R_K}\right) - c_1\left(\frac{1}{t_\epsilon}\tilde{\boldsymbol{\Gamma}} - \tilde{\mathbf{K}}\right)^{-1}\left(-\tilde{\mathbf{F}} + \mathbf{R_K} - \frac{1}{t_\epsilon}\mathbf{R_\Gamma}\right)\exp\left(-t/t_\epsilon\right)$$

$$+ \left[\left(\mathbf{Id} + \mathbf{M}^2\right)^{-1}\mathbf{M}\tilde{\boldsymbol{\Gamma}}^{-1}\mathbf{R_\Gamma} - \frac{1}{\Omega}\left(\mathbf{Id} + \mathbf{M}^2\right)^{-1}\tilde{\boldsymbol{\Gamma}}^{-1}\left(\tilde{\mathbf{F}} - \mathbf{R_K}\right)\right]c_2\cos(\Omega t)$$

$$- \left[\left(\mathbf{Id} + \mathbf{M}^2\right)^{-1}\tilde{\boldsymbol{\Gamma}}^{-1}\mathbf{R_\Gamma} + \frac{1}{\Omega}\left(\mathbf{Id} + \mathbf{M}^2\right)^{-1}\mathbf{M}\tilde{\boldsymbol{\Gamma}}^{-1}\left(\tilde{\mathbf{F}} - \mathbf{R_K}\right)\right]c_2\sin(\Omega t), \quad \text{(A2.11)}$$

where $\mathbf{M} = -\frac{1}{\Omega}\tilde{\boldsymbol{\Gamma}}^{-1}\tilde{\mathbf{K}}$, $\mathbf{Id}$ is the identity matrix of the size of $\mathbf{M}$, and A is a coefficient calculated to have $\tilde{\mathbf{w}}(t = 0) = \mathbf{0}$, which yields:

$$A = -c_1\tilde{\mathbf{K}}^{-1}\left(\tilde{\mathbf{F}} - \mathbf{R_K}\right) + c_1\left(\frac{1}{t_\epsilon}\tilde{\boldsymbol{\Gamma}} - \tilde{\mathbf{K}}\right)^{-1}\left(-\tilde{\mathbf{F}} + \mathbf{R_K} - \frac{1}{t_\epsilon}\mathbf{R_\Gamma}\right)$$

$$+ \left(\mathbf{Id} + \mathbf{M}^2\right)^{-1}\left(\mathbf{Id} - \mathbf{M}\right)\tilde{\boldsymbol{\Gamma}}^{-1}\mathbf{R_\Gamma} + \frac{1}{\Omega}\left(\mathbf{Id} + \mathbf{M}^2\right)^{-1}\left(\mathbf{Id} + \mathbf{M}\right)\tilde{\boldsymbol{\Gamma}}^{-1}\left(\tilde{\mathbf{F}} - \mathbf{R_K}\right)$$

$$\text{(A2.12)}$$

Chapter 4

Model of Cell Migration Driven by Mechanical Cues

The work presented in this chapter was performed in collaboration with Prof. Roger Kamm, MIT.

4.1 Introduction

Migration of cells in a three dimensional matrix lies at the heart of several key physiological processes including angiogenesis, vasculogenesis, and wound healing (Lamalice et al., 2007, Risau and Flamme, 1995). These processes have been reproduced in vitro (Jeon et al., 2014, Whisler et al., 2012); however, cellular migration in 3D matrices remains poorly understood.

Studies of cell migration on 2D substrates have documented three distinct and successive steps: 1) protrusion at the leading edge of the cell and formation of new attachments with the matrix, 2) contraction of the cell and establishment of a gradient of binding and traction forces between the leading and rear edges of the cell, and finally 3) detachment of the rear edge and pulling of the cell body towards the front edge (Lauffenberger and Horwitz, 1996, Ridley et al., 2003). Cellular adhesion to the extracellular matrix is mediated by integrins, transmembrane proteins that form a bridge between specific ligands in the matrix and the cytoskeleton within the cell (Brakebusch and Fässler, 2003, Plow et al., 2000). Contractile stress is generated by the actomyosin machinery of the cell: myosin motors slide actin filaments relative to one another, which tenses these filaments and their ends (Goeckeler and Wysolmerski, 1995). A traction force is thus applied to the integrins that are bound to the actin filaments, and this force is transmitted to

the matrix. When subjected to force, integrins cluster with other proteins to form focal adhesion sites that mediate firm cellular attachment to the matrix (Balaban et al., 2001, Wolfenson et al., 2011). Focal adhesion development has also been shown to be proportional to the matrix stiffness (Choquet et al., 1997).

Intuitively, cellular migration in 3D matrices is bound to differ from migration on 2D substrates. The basal-apical polarity that is imposed in 2D does not exist in 3D, and the cell does not have to overcome the resistance of dense surroundings in 2D as it does in 3D. Two prototypic modes of migration have been reported in 3D matrices: the amoeboid migration in which the cell squeezes through the matrix (Lämmermann and Sixt, 2009) and the mesenchymal migration which relies on successive steps of proteolytic-dependent protrusion and actin-dependent pulling (Friedl and Wolf, 2009). This second mode of migration shares many features with the 2D migration process, including the general steps of protrusion, maturation of the attachments, and contraction-dependent detachment. The main differences are the proteolytic activity (which is necessary to overcome the matrix barrier) the more diffuse distribution of adhesions, and the absence of stress fibers in favor of a less organized actomyosin system in the 3D case (Even-Ram and Yamada, 2005, Friedl and Bröcker, 2000).

Experiments in both 2D and 3D have shown that cell migration is dependent on matrix stiffness and that cells tend to migrate towards regions of greater stiffness, a phenomenon termed durotaxis (Ehrbar et al., 2011, Hadjipanayi et al., 2009, Lo et al., 2000). However, in the presence of a neighboring cell, this preference is not observed, and it has been suggested that an increase in the matrix resistance sensed by the cell was responsible for this observation (Lo et al., 2000). Along the same lines, a pair of cells was shown to remain close to one another during migration as a result of cell-cell communication through traction forces exerted on the substrate (Reinhart-King et al., 2008).

Based on these observations and on the similarities between 2D migration and 3D mesenchymal migration, we propose that migration of cells towards each other in a 3D matrix may involve the "apparent stiffness" of the matrix sensed by the cells. We define this apparent stiffness as the ratio of the stress applied by the actomyosin machinery to the resulting strain at the cell border. We show that this concept allows us to account for absolute matrix mechanical properties as well as other parameters such as the presence of an obstacle in the matrix and cell mechanical properties.

Furthermore, we develop a model of the steps of attachment and detachment during 3D mensenchymal migration. Following experimental evidence that cell–matrix adhesion density increases with increasing matrix stiffness, we postulate that the distribution

of adhesive proteins at the cell border is proportional to the apparent stiffness. Adhesions are then detached with a force per adhesion probability. This model reproduces the anisotropic detachment of adhesions and subsequent motion of the cell body. The preferred migration towards stiffer regions observed experimentally is predicted by the model, and this preference is shown to mediate cell migration towards obstacles or other cells. These results confirm that mechanical cues are an important factor that drives cell migration in 3D matrices and regulates cell-cell migration in these matrices.

4.2   Methods

Several modes of cell migration have been documented in 3D matrices (Friedl and Wolf, 2009, Lämmermann and Sixt, 2009). We focus here on mesenchymal migration, which has been described as consisting of three distinct steps of protrusion, maturation of attachments to the matrix, and anisotropic detachment of the attachments (Friedl and Wolf, 2009). Our goal is to understand how cell-generated contraction forces allow the cell to sense a mechanical obstacle such as another cell and to determine migration direction; therefore, we focus specifically on the steps of attachment and detachment.

In the first step of the attachment-detachment sequence, the cell contracts and a gradient of attachments is established depending on the traction forces generated (Friedl and Bröcker, 2000). The cell contraction is modeled by a uniform contractile stress at the cell membrane and the attachment gradient by a distribution of adhesive proteins that depends on the resistance of the matrix to this force. In the second step, the attachments detach sequentially with a force−dependent probability. The remaining attachment determines the direction of migration of the cell.

Consistent with experimental results (Friedl and Bröcker, 2000, Friedl and Wolf, 2009), contracile stress plays a key role in migration. We begin by describing the modeling of this active contraction before delving into the steps of attachment and detachment.

4.2.1   Geometry

We study the migration of a single cell embedded in a matrix whose walls are fixed and thus constitute an obstacle to cell movement. We model the cell as a right circular cylinder of radius R and height $h >> R$, so that we can limit our study to the simplified 2D problem represented in figure 4.1. Under this simplification, the cell is modeled as a disk of radius R, and the matrix as a rectangle. The cell is initially at a distance L from three of the walls and at a distance $d = \alpha R$ from the fourth wall. The distance

L is chosen sufficiently large so that the walls have a negligible effect on the results. Thus, the obstacle is the nearest wall and the coefficient α provides a measure of how far the obstacle is from the cell. The regions where the cell is attached to the matrix are grouped in the attached interface $I_{attached}$ (solid line in figure 4.1), and the regions where the cell does not adhere to the matrix are grouped in the detached interface $I_{detached}$.
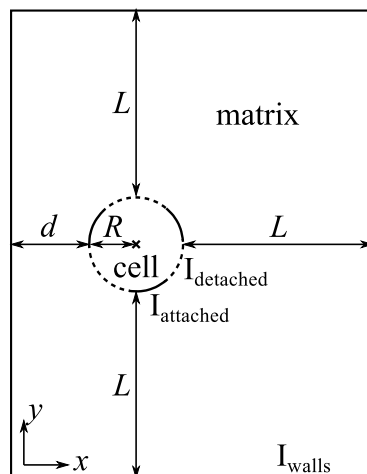
FIGURE 4.1: 2D geometry of the problem: we consider a disk cell of radius R in a rectangular matrix. The cell is at a distance d from the left wall and at a distance $L \geq d$ from the other walls. Cell membrane can be attached to the matrix (interface $I_{attached}$, solid lines) or detached (interface $I_{detached}$, dashed lines). The matrix outer walls (I_{walls}) are fixed.

Although we study a 2D geometry, it is indeed the migration in a 3D matrix that we are modeling. On a 2D substrate, the cell sits on the substrate and the adhesions would be defined through the entire disk section. It should be noted that the model formulation applies directly to the 3D case, but we limit the current effort to the 2D case in order to reduce computational time cost. Limited comparisons of the 2D results with full 3D results on a spherical cell embedded in a parallepipedic matrix show that the general behavior reported here in 2D is representative of that obtained in 3D.

4.2.2 Active contraction of the cell

Many cell types including endothelial cells adhere to the surrounding matrix via transmembrane proteins that form a bridge between the extracellular matrix and the actin cytoskeleton inside the cell (Brakebusch and Fässler, 2003, Plow et al., 2000). This attachment mediates mechanical communication between the cell and its matrix (Cukierman et al., 2001, Harris et al., 1980). Myosin activity along actin filaments generates tension on the adhesion sites that leads to traction forces on the matrix (Goeckeler and Wysolmerski, 1995). We model the contractile stress generated by the actomyosin

machinery by a uniform radial stress at the cell membrane:

$$\sigma_{\mathbf{a}} = -\sigma_0 \mathbf{n} \otimes \mathbf{n}, \tag{4.1}$$

where $\sigma_{\mathbf{a}}$ is the Cauchy stress tensor, σ_0 is the scalar value of stress generated by the actomyosin machinery, and $\mathbf{n}$ is the outward normal to the cell membrane. The active contraction of the cell is an external force that must be balanced by the cell and matrix internal stresses, $\sigma_{\mathbf{c}}$ and $\sigma_{\mathbf{m}}$ respectively.

We model both the cell and the matrix as linear elastic materials, of respective Young's moduli E_c and E_m and Poisson's ratios ν_c and ν_m (Balland et al., 2006, Lim et al., 2006). The constitutive law of elasticity yields the relations between the stress and the strain in the cell and the matrix (Holzapfel, 2000, Le Tallec, 2008):

$$\sigma_{\mathbf{c}}(x,y) = \frac{E_c}{1+\nu_c}\epsilon_{\mathbf{c}}(x,y) + \frac{E_c}{(1-2\nu_c)(1+\nu_c)}\mathrm{tr}(\epsilon_{\mathbf{c}}(\mathbf{x},\mathbf{y}))\mathbf{1}, \tag{4.2a}$$

$$\sigma_{\mathbf{m}}(x,y) = \frac{E_m}{1+\nu_m}\epsilon_{\mathbf{m}}(x,y) + \frac{E_m}{(1-2\nu_m)(1+\nu_m)}\mathrm{tr}(\epsilon_{\mathbf{m}}(\mathbf{x},\mathbf{y}))\mathbf{1}, \tag{4.2b}$$

where $\mathbf{1}$ is the identity tensor, and $\epsilon_{\mathbf{c}}$ and $\epsilon_{\mathbf{m}}$ are the cell and matrix strain tensors, related to the gradient of displacement in the cell $\nabla\mathbf{u}_c$ and in the matrix $\nabla\mathbf{u}_m$, respectively, by the relation:

$$\epsilon(x,y) = \frac{1}{2}\left(\nabla\mathbf{u}(x,y) + {}^t\nabla\mathbf{u}(x,y)\right). \tag{4.2c}$$

In the absence of volumic and inertial forces, the balance of forces yields:

$$\mathrm{div}(\sigma_{\mathbf{c}}) = \mathbf{0}, \tag{4.3a}$$

$$\mathrm{div}(\sigma_{\mathbf{m}}) = \mathbf{0}. \tag{4.3b}$$

The cell and matrix equations are coupled at the interface where the cell and matrix are attached, $I_{attached}$. The boundary condition imposes that the active stress $\sigma_{\mathbf{a}}$ is balanced by the cell and matrix internal stresses:

$$\sigma_{\mathbf{c}}(x,y).\mathbf{n} - \sigma_{\mathbf{m}}(x,y).\mathbf{n} = \sigma_{\mathbf{a}}.\mathbf{n} \text{ if } (x,y) \in I_{attached}, \tag{4.4a}$$

and that the matrix and cell boundaries move together where they are attached:

$$\mathbf{u}_{\mathbf{c}}(x,y) = \mathbf{u}_{\mathbf{m}}(x,y) \text{ if } (x,y) \in I_{attached}. \tag{4.4b}$$

On the other hand, on the interface where the cell is detached from the matrix, the cell alone sustains the active stress:

$$\sigma_{\mathbf{c}}(x, y).\mathbf{n} = \sigma_{\mathbf{a}}.\mathbf{n} \text{ if } (x, y) \in I_{detached}, \tag{4.4c}$$

whereas the matrix is free of stress:

$$\sigma_{\mathbf{m}}(x, y).\mathbf{n} = \mathbf{0} \text{ if } (x, y) \in I_{detached}. \tag{4.4d}$$

A zero displacement boundary condition is imposed on the walls of the matrix I_{walls}:

$$\mathbf{u_m}(x, y) = \mathbf{0} \text{ if } (x, y) \in I_{walls}. \tag{4.4e}$$

The finite element method is used to solve these equations (Bonnet and Frangi, 2006). The weak form of equations (4.3a) and (4.3b) is derived using stress expressions (4.2a) and (4.2b) and boundary conditions (4.4):

$$\begin{cases} \int_{\Omega_c} \left(2\mu_c \epsilon_{\mathbf{c}} \tilde{\epsilon}_{\mathbf{c}} + \lambda_c \text{div}(\mathbf{u_c}) \text{div}(\tilde{\mathbf{u}}_{\mathbf{c}}) \right) d\Omega - \int_{I_{detached}} \sigma_{\mathbf{a}}.\mathbf{n} d\partial\Omega = 0 \\ \mathbf{u_c} = \mathbf{u_m} \text{ on } I_{attached} \end{cases} \tag{4.5a}$$

and

$$\begin{cases} \int_{\Omega_m} \left(2\mu_m \epsilon_{\mathbf{m}} \tilde{\epsilon}_{\mathbf{m}} + \lambda_m \text{div}(\mathbf{u_m}) \text{div}(\tilde{\mathbf{u}}_{\mathbf{m}}) \right) d\Omega - \int_{I_{attached}} (\sigma_{\mathbf{c}} - \sigma_{\mathbf{a}}).\mathbf{n} d\partial\Omega = 0, \\ \mathbf{u_m} = \mathbf{0} \text{ on } I_{walls}, \end{cases} \tag{4.5b}$$

where $\tilde{\mathbf{u}}_{\mathbf{c}}$ and $\tilde{\mathbf{u}}_{\mathbf{m}}$ are test displacements, $\tilde{\epsilon}_{\mathbf{c}}$ and $\tilde{\epsilon}_{\mathbf{m}}$ are the strains associated with these displacements (equation (4.2c)), Ω_c and Ω_m are the cell and matrix domains, and $\mathbf{n}$ is the boundary normal outward with respect to the domain considered. The treatment of the attached interface boundary condition was chosen so that both the cell and the matrix have a displacement boundary condition.

Equations (4.5a) and (4.5b) are solved using the finite element software FreeFem (Hecht, 2012). To ensure convergence of the coupling of equations (4.5a) and (4.5b), they are solved iteratively until the following convergence condition is enforced:

$$\sum_{(x,y) \in I_{attached}} ||\mathbf{u_c}(x, y) - \mathbf{u_m}(x, y)|| \leq \gamma \sum_{(x,y) \in I_{attached}} ||\mathbf{u_m}(x, y)||, \tag{4.6}$$

where γ is a scalar.

The cell and matrix domains are meshed using gmesh (Geuzaine and Remacle, 2009). As shown in figure 4.2, a coarse mesh size m_1 is chosen at the matrix-wall boundary, a fine mesh size m_3 at the cell-matrix boundary (red in figure 4.2), and an intermediate mesh

size m_2 inside the cell and at intermediate location between the cell-matrix boundary and the matrix walls (dashed lines in figure 4.2A).
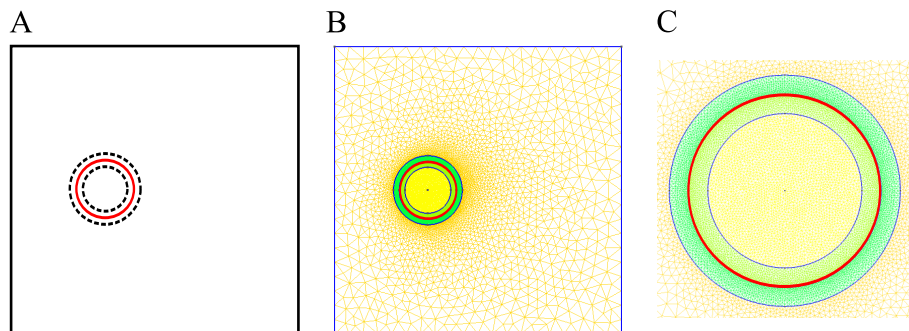
FIGURE 4.2: A. Mesh size is m_1 at the outer matrix wall, m_2 at the cell-matrix interface (red in the figure), and m_3 at two intermediate locations within the cell and the matrix (dashed lines in the figure). B. Mesh obtained with $m_1 = L/10$, $m_2 = R/30$ and $m_3 = R/90$. C. Zoom on the cell-matrix interface mesh (red line).

The convergence of the iterative finite element resolution of equations (4.5a) and (4.5b) was tested on the case of concentric disk matrix and cell, for which an analytical solution is available. Based on the results of this test case, we choose $\gamma = 0.01$, $m_1 = L/10$, $m_2 = R/30$ and $m_3 = R/90$. The resulting mesh is shown in figures 4.2B and 4.2C. With these parameters, the time needed to compute the solution of the system of equations (4.5a) and (4.5b) is one minute on average on an Intel Core i5 operating Linux.

4.2.3   First step: matrix stiffness probing and adhesion to the matrix

Definition of the apparent stiffness of the matrix

The standard engineering approach to determining the mechanical properties of a material is to impose a known force on the material and record the resulting deformation or to impose a known deformation and measure the resulting force. The exact mechanisms by which cells sense matrix stiffness are not known, but it is thought that they require the application of traction forces to the matrix at adhesion sites. Therefore, we propose that the cell probes its surrounding environment by applying a contractile stress at its membrane, and registering the resultant cell strain.

We model the traction stress generated by the cell contractile machinery by a normal stress (negative pressure) at the cell membrane (equation (4.1)). We define the apparent matrix stiffness sensed at a point (x, y) on the cell border as the ratio of the applied stress to the cell radial strain:

$$E_{app}(x, y) = \frac{\sigma_0}{|\mathbf{n}.\epsilon_\mathbf{c}(\mathbf{x}, \mathbf{y}).\mathbf{n}|}, \tag{4.7}$$

where the strain $\epsilon_{\mathbf{c}}$ is obtained by solving the system of equations (4.5a) and (4.5b) for the case of a cell uniformly attached to the matrix, i.e. $I_{detached} = \varnothing$. This configuration is consistent with the formation of diffuse nascent adhesions after the protrusion step (Cukierman et al., 2001).

Adhesion to the matrix

In cells cultured on 2D substrates, integrins cluster into regions of firm attachment called focal adhesions, whose size depends on the force applied to the adhesion and on matrix stiffness (Balaban et al., 2001, Pelham and Wang, 1997). In 3D, these structures are usually not observed and the distribution of adhesive proteins is more diffuse, but their density also increases with matrix stiffness (Cukierman et al., 2001). Consistent with these observations, the distribution of proteins at the cell membrane is taken proportional to the apparent matrix stiffness (equation (4.7)). To avoid mesh-size dependent distribution of proteins, we regroup cell–matrix border mesh points in regions of attachments over which the apparent stiffness is roughly constant, and we define the number of adhesions in the attachment region r as:

$$n_{adh}(r) = n_{adh}^{tot} \frac{\sum\limits_{(x,y)\in r} E_{app}(x,y)}{\sum\limits_{(x,y)\in I} E_{app}(x,y)}, \tag{4.8}$$

where n_{adh}^{tot} is the total number of adhesions at the cell membrane.

4.2.4 Second step: detachment of the adhesions and cell body motion

Force-dependent probability of detachment

The adhesions of region $r \in I_{attached}$ are subjected to a force from the matrix:

$$F(r) = \sum_{(x,y)\in r} \sigma_{\mathbf{m}}(x,y)hdl(x,y), \tag{4.9}$$

where dl is the boundary element length around the point (x,y) and h is the height of the cylindrical cell. Therefore, the force per adhesion in region r is:

$$F_{adh}(r) = \frac{\sum\limits_{(x,y)\in r} \sigma_{\mathbf{m}}(x,y)hdl(x,y)}{n_{adh}(r)}. \tag{4.10}$$

Thus, a non-uniform apparent matrix stiffness results in non-uniform adhesion distribution and force per adhesion at the cell membrane.

The probability of detachment of an adhesion is force−dependent (Bell, 1978, Evans and Ritchie, 1997, Li et al., 2003). Indeed, the energy of the integrin–ligand system is a well, and the minimum is reached when the adhesion is formed. To detach, the system has to overcome the energy well, and application of a force provides energy that helps the transition (Bell, 1978). The probability of an adhesion submitted to a force F to detach during a time interval t is given by (Evans and Ritchie, 1997):

$$p(t) = 1 - e^{-k(F)t}. \tag{4.11}$$

In the case of an integrin, the rate of detachment $k(f)$ is (Li et al., 2003):

$$k = \left(\frac{1}{k_1} e^{-\frac{Fg_1}{k_bT}} + \frac{1}{k_2} e^{-\frac{Fg_2}{k_bT}} \right)^{-1}, \tag{4.12}$$

where k_1 and k_2 are the two characteristic dissociation rates of the integrin-matrix bond in the absence of force, associated with two energy transitions that occur at reaction coordinates g_1 and g_2. Application of a force provides the work energies Fg_1 and Fg_2 that lower the energy barrier. The work energy is normalized by the thermal energy k_bT where k_b is the Boltzmann constant and T is the temperature.

Integrins within an attachment region do not have an independent fate and are considered to remain attached or to detach together. We can then define the dissociation rate of the region r under the force $F_{adh}(r)$ by using equation (4.10) in (4.12).

Iterative detachment of the adhesions

In our model, adhesions are made to detach in an iterative manner. At each iteration, equations (4.5a) and (4.5b) are solved, the force per adhesion is computed, and an adhesion is either detached or not in accordance with a criterion discussed below. The attached and detached interfaces $I_{attached}$ and $I_{detached}$ are consequently modified, and in the next iteration, solving equations (4.5a) and (4.5b) yields the new distribution of force per adhesion. Iteration stops when only one region of adhesion remains attached to the matrix. In this process, the cell center of mass has moved towards the last attachment, a first step in directional migration.

To determine which attachment region detaches first, a scalar $0 \leq r_a \leq 1$ is drawn at random for each attachment $a \in I_{attached}$ and the time t_r of detachment of a is deduced from equation (4.11), i.e.:

$$t_a = \frac{\ln(1 - r_a)}{k(F_adh(a))}. \tag{4.13}$$

The region of smallest detachment time is detached and is moved from $I_{attached}$ to $I_{detached}$. The other adhesions remain attached.

To get information on the distribution of migration direction, the whole process has to be repeated many times, typically several hundred times. The associated computational cost is too high to allow a complete parametric study of the migration. Instead, we focus on the preferred direction of migration and the probability of an attachment to be the first to detach.

We turn off the random contribution to the problem by replacing the random detachment time t_a by the mean detachment time τ_a, defined as the time at which the adhesion has a probability of 50% to be detached, i.e.:

$$\tau_a = \frac{\ln(2)}{k(F(a))}. \tag{4.14}$$

This determinitistic approach provides information on the preferred direction of migration.

We caculate the probability for an attachment to be the first to detach. The probability p^1_{first} of attachment $a = 1$ to be the first of N attachments to detach is:

$$p^1_{first} = p(t_1 < \overline{t_1}) = p(t_1 - \overline{t_1} < 0), \tag{4.15}$$

where $\overline{t_1}$ is the time needed for an attachment other than 1 to detach. The probability p^1_{first} is the difference of two random variables. If $f_1(t)$ and $f_{\overline{1}}(t)$ are the probability density functions associated with the events 'Attachement 1 detaches during time t' and 'An attachment other than 1 detaches during time t', then the probability density function of the difference of the two random variables is (Méléard, 2010):

$$f(z) = \int_{-\infty}^{+\infty} f_{\overline{1}}(t) f_1(z+t) dt. \tag{4.16}$$

The probability density function $f_1(t)$ is obtained by calculating the time derivative of equation (4.11):

$$f_1(t) = k(F_1) e^{(-k(F_1)t)} \ \forall t \geq 0. \tag{4.17}$$

The probability law of the event 'Another attachment than 1 detaches during time t' is:

$$p(\overline{t_1} < t) = 1 - p(\overline{t_1} > t) = 1 - p(t_2 > t \ \& \ ... \ \& \ t_N > t) = 1 - \prod_{i=2}^{N} p(t_i > t), \tag{4.18}$$

because the events are independent. We use expression (4.11) to get:

$$p(\overline{t_1} < t) = 1 - \prod_{i=2}^{N} e^{(-k(F_i)t)}. \tag{4.19}$$

Taking the derivative of equation (4.19) yields the probability density function of the event, defined on $t \in [0, +\infty]$:

$$f_{\overline{t_1}}(t) = \sum_{i=2}^{N} k(F_i) \prod_{i=2}^{N} e^{(-k(F_i)t)} \ \forall t \geq 0. \tag{4.20}$$

Expression of the probability density functions $f_1(t)$ and $f_{\overline{1}}(t)$ provided by equations (4.17) and (4.18) respectively are used in equation (4.16) to get the expression of the probability density function of the event 'The difference between the time of detachment of adhesion 1 and the time of detachment of adhesion N is equal to z':

$$f(z) = k(F_1) \frac{\sum_{i=2}^{N} k(F_i)}{\sum_{i=1}^{N} k(F_i)} \exp\left(\sum_{i=2}^{N} k(F_i)z\right). \tag{4.21}$$

Finally, the probability that attachment 1 detaches first is the probability that $z \leq 0$:

$$p_{first}^{1} = \int_{-\infty}^{0} f(z) = \frac{k(F_1)}{\sum_{i=1}^{N} k(F_i)}. \tag{4.22}$$

In conclusion, the probability that attachment a detaches first is:

$$p_{first}^{a} = \frac{k(F_a)}{\sum_{i=1}^{N} k(F_i)}. \tag{4.23}$$

4.2.5 Parameters

Table 4.1 shows the typical values obtained from literature for the geometric and mechanical parameters of the problem. The height of the cylinder was chosen to match the cylinder surface area to that of a sphere of radius R.

4.3 Results

4.3.1 First step: apparent stiffness and adhesion to the matrix

In the first step of migration, the cell probes its mechanical surroundings by application of a tensile stress to the cell−matrix interface. The apparent matrix stiffness, E_{app}, is the resistance to deformation that the cell experiences in this process, defined as the ratio of the applied stress to the radial strain at the cell membrane (equation

TABLE 4.1: Model of cellular migration: mechanical and geometric parameter values.

	Symbol	Unit	Value	Source
Cell radius	R	m	10^{-5}	Cukierman et al. 2002
Cylindrical cell height	h	m^2	2.10^{-5}	
Active stress magnitude	σ_0	Pa	100	Lo et al. 2000
Cell Young's modulus	E_c	kPa	1	Balland et al. 2006
Cell Poisson's ratio	ν_c	1	0.4	Lim et al. 2006
Matrix Young's modulus	E_m	kPa	10	Duong et al. 2009
				Pedersen and Swartz 2005
Matrix Poisson's ratio	ν_m	1	0.25	Duong et al. 2009
Total number of adhesive proteins	n_{adh}^{tot}	1	1000	Irvine et al. 2002

(4.7)). Figure 4.2A depicts the apparent stiffness along the border of a cell that lies at a distance $d = R$ from the left wall and at a distance $L > d$ from the other walls (figure 4.1). It shows that the apparent stiffness is non-uniform along the cell border, which is due to the vicinity of the fixed wall since cell and matrix mechanical properties are uniform. The apparent stiffness is greatest near the wall, which is consistent with the notion of increased resistance to deformation of a smaller sample of material. If u is the displacement imposed to a sample of characteristic length l, its strain is $\epsilon \sim u/l$, and the associated stress is $\sigma \sim Eu/l$; thus, a given stress σ yields a deformation u proportional to the sample size. Figure 4.4A illustrates the magnitude of the displacement in the matrix and in the cell in this first step and illustrates that the displacement of the cell−matrix interface is indeed smaller near the wall. At the other side of the cell, at $x/R \approx 3$, the apparent stiffness is intermediate (figure 4.2A). Indeed, the radial strain experienced by the cell is $\epsilon_c \approx (u(x/R = 3) - u(x/R = 1))/R \approx u(x/R = 3)/R$ along the horizontal median and $\epsilon_c \approx (u(y/R = 6) - u(y/R = 4))/R \approx 2u(y/R = 6)/R$ along the vertical median (the displacements at the top and bottom of the cell point in opposite directions). Thus, the presence of an obstacle at $x = 0$ induces a greater apparent stiffness along the x-median of the cell, with a maximum at the closest to the obstacle.

The cell border is divided into a fixed number of attachment regions of equal length, and the density of integrin proteins in one of these regions is assumed to be proportional to the local apparent stiffness (equation (4.8)). Figure 4.3B shows the density of integrin proteins along the cell border. As a direct consequence of the heterogeneity of the apparent stiffness (figure 4.3A), the protein distribution is not uniform, and there is a higher integrin density in the attachment zones near the obstacle, at $x/R \approx 1$.
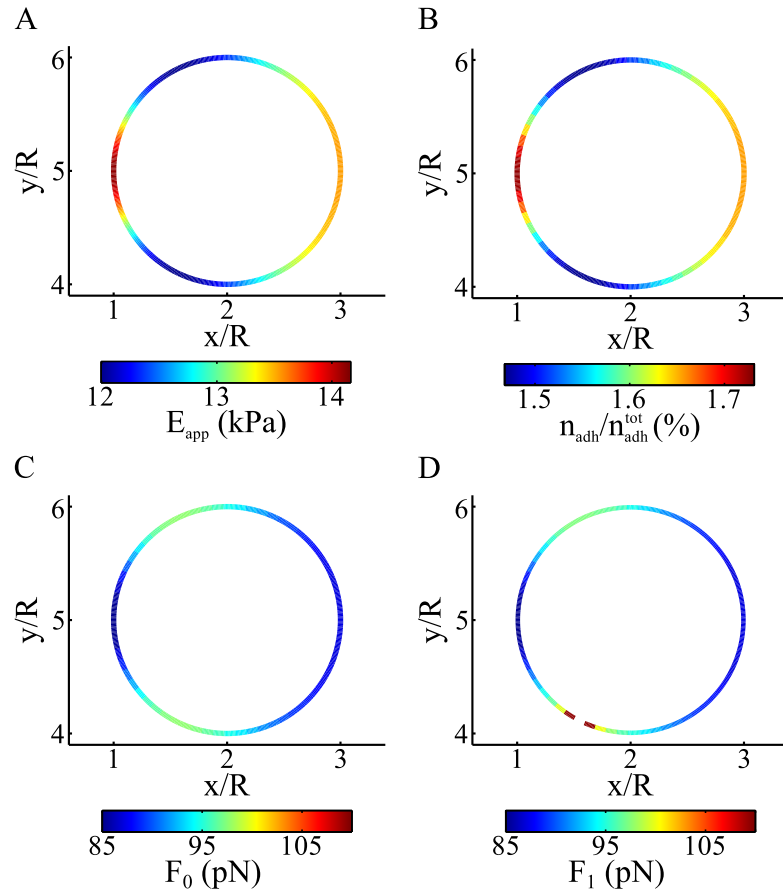
FIGURE 4.3: Cell−matrix interface with colormap of the apparent stiffness (A), of the relative number of integrins in the adhesions (B), of the force per integrin in the initial state where no adhesion is detached (C) and of the force per integrin in the attached regions after one adhesion has been detached (break in the circle) (D). In this example, $d = R$, $E_c = 1$ kPa, $E_m = 10$ kPa, $\nu_c = 0.4$, $\nu_m = 0.25$, and $n_{adh}^{tot} = 1000$.

4.3.2   Second step: iterative detachment from the matrix

Adhesions that bind the cell to the matrix are subjected to the reaction force of the matrix in response to the active contraction of the cell. The force per adhesive protein (equation (4.10)) along the cell−matrix interface is depicted in figure 4.3C. Due to the higher number of adhesive proteins near the wall ($x/R \approx 1$) and opposite to the wall ($x/R \approx 3$), the force per adhesive protein is smaller in these regions. This force determines the probability of the attachment region to detach, following equations (4.11) and (4.12). The attachment with the highest probability to detach is detached, the new cell−matrix balance is computed, and the matrix stress is used to obtain the new force distribution, as shown in figure 4.3D. The matrix experiences greater stress at the transition between attachment and detachment, so that the force sustained by the adhesive proteins is significantly higher in this region. Therefore, the region neighboring the first detachment has a greater probability to detach than the other regions, favoring cascade detachment. Figure 4.4 shows the magnitude of the displacement in the matrix

and the cell at the initial step when all adhesions are attached (figure 4.4A), in an intermediate step (figure 4.4B) and in the final step where only one attachment region remains (figure 4.4C). As suggested by the increase in force per adhesion at the vicinity of the first detachment (figure 4.3D), the intermediate step shows that the detached adhesions form a continuous region around the first detachment.
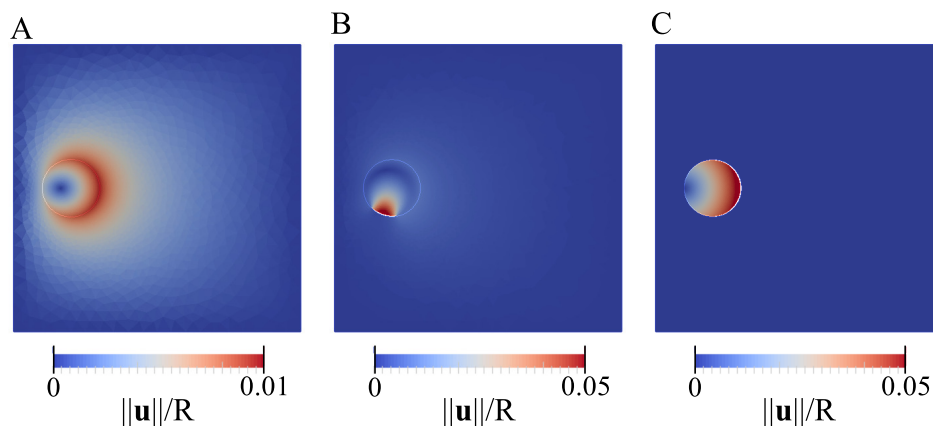
FIGURE 4.4: Magnitude of the displacement in the matrix and in the cell normalized by the radius of the cell in the initial state where no adhesion is detached (A), in an intermediate state where part of the adhesions are detached (B), and in the final state where a single attachment remains (C). The cell−matrix border is marked in white. In this example, $d = R$, $E_c = 1$ kPa, $E_m = 10$ kPa, $\nu_c = 0.4$, $\nu_m = 0.25$, and $n_{adh}^{tot} = 1000$.

4.3.3 Dependence of the migration on the distance to the wall

Figure 4.5 shows the apparent stiffness and the relative number of proteins per adhesions along the cell border as a function of the angular coordinate θ. As represented in the insets in figure 4.5, the angle θ is the angle between a point on the cell border and the x-direction. Results for a cell at a distance $d = R$, $d = 2.5R$ and $d = 4R = L$ from the wall are shown in green, blue, and red, respectively. As desribed above, the presence of the wall, here at $\theta = \pi$, is felt by the cell as an increase in stiffness and leads to an increased density of adhesions at $\theta = \pi$ and at $\theta = 0$. However, this effect is damped when the cell gets further from the wall. At $d = L$, the variations are minimal, and the effect that is present is primarily attributable to the corners of the matrix. To determine how the local variation in the relative density of integrin proteins per adhesion region impacts the migration of the cell, we study the probability of different regions to detach first and the preferred direction of migration. Figure 4.6A shows the probability that the first detachment occurs in the positive x-direction ($-\pi/4 \leq \theta \leq \pi/4$, green data in figure 4.6A), in the positive y-direction ($\pi/4 \leq \theta \leq 3\pi/4$, blue data in figure 4.6A) and in the negative x-direction ($3\pi/4 \leq \theta \leq 5\pi/4$, red data in figure 4.6A) as a function of the distance from the wall. Due to the symmetry of the system, the negative y data

FIGURE 4.5: Apparent stiffness (A) and relative number of integrins in the adhesions (B) as a function of the position angle θ for cell−wall distances $d = R$ (green line), $d = 2.5R$ (blue line) and $d = 4R$ (red line). The insets show the cell (disk) and the nearest wall (line) as well as the definition of d and θ. In this example, $E_c = 1$ kPa, $E_m = 10$ kPa, $\nu_c = 0.4$, and $\nu_m = 0.25$.

are identical to the positive y data and are not shown. The probability that the first adhesion detaches between θ_1 and θ_2 is:

$$p_{first}^{[\theta_1,\theta_2]} = \sum_{a \in [\theta_1,\theta_2]} p_{first}^a = \frac{\sum\limits_{a \in [\theta_1,\theta_2]} k(F_1)}{\sum\limits_{a \in I_{attached}} k(F_i)}, \qquad (4.24)$$

where p_{first}^a is the probability that adhesion a detaches first and is given by equation (4.23).
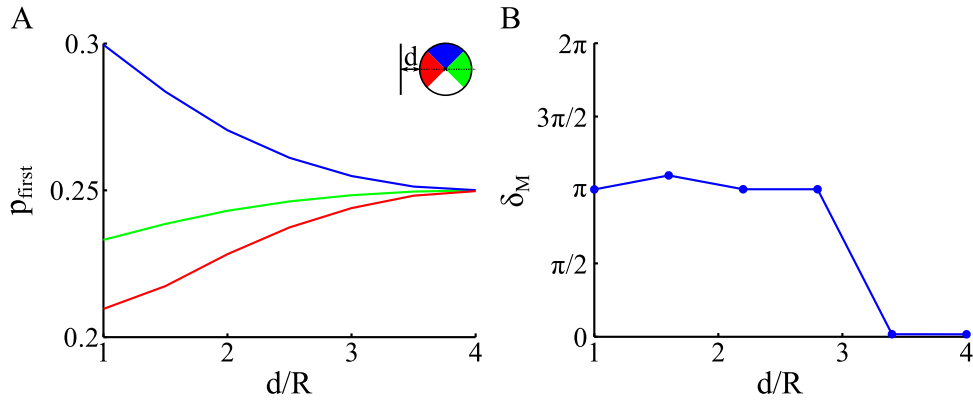
FIGURE 4.6: A. Probability that the first detachment occurs along $-\pi/4 \leq \theta \leq \pi/4$ (green line and green region in the inset), along $\pi/4 \leq \theta \leq 3\pi/4$ (blue line and blue region in the inset), or along $3\pi/4 \leq \theta \leq 5\pi/4$ (red line and red region in the inset) as a function of the distance to the wall, d, relative to the radius of the cell, R. B. Preferred direction of migration as a function of the distance to the wall, d, relative to the radius of the cell, R. In this example, $E_c = 1$ kPa, $E_m = 10$ kPa, $\nu_c = 0.4$, $\nu_m = 0.25$, and $n_{adh}^{tot} = 1000$.

Consistent with the density of adhesions (figure 4.5A) and the force per adhesive protein (figure 4.3C), the first adhesion is more likely to detach in the positive or negative

y-direction regions and least likely to detach near the wall. When the distance from the wall increases, these differences decrease, and finally, when the cell is equidistant from the four walls, $d = L = 4R$, the three regions have the same probability to experience the first detachment. Thus, cell migration is less likely to occur along the y-direction than along the x-direction, and along the x-direction, it is more likely to occur towards the wall than in the opposite direction. Naturally, when the cell−wall distance increases, the bias decreases as the effect of the wall is reduced.

Figure 4.6B shows the preferred direction of migration, δ_M, as a function of the distance from the wall. The preferred direction of migration is the angle between the x-direction and the displacement of the cell center. It is computed using a deterministic approach where the attachment that detaches is the one with the smallest mean detachment time as defined by equation (4.14). Figure 4.6B shows that the cell indeed migrates either towards the wall ($\delta_M \approx \pi$) or in the opposite direction ($\delta_M \approx 0$). The cell migrates towards the wall until $d \approx 3R$, and then away from the wall. However, note that the further the cell is from the left wall, the less significant are the deterministic results.

4.3.4 Dependence of the migration on cell and matrix mechanical properties

Several studies have shown that the mechanical properties of both the cell and the extracellular matrix play a key role in cell migration (Ehrbar et al., 2011, Hadjipanayi et al., 2009). Therefore, we study the dependence of our results on the Young's modulus (figure 4.7) and on the Poisson's ratio of (figure 4.8) of the cell and the matrix.

Figure 4.7A illustrates the apparent stiffness at the cell border for a cell Young's modulus $E_c = 1$ kPa and a matrix Young's modulus $E_m = 2E_c$ (green line), $E_m = 10E_c$ (blue line) and $E_m = 100E_c$ (red line). The mean apparent stiffness is of the same order of magnitude as the real matrix stiffness. The presence of the wall yields similar variations to those discussed before, with a positive peak at $\theta = \pi$ near the wall and at $\theta = 0$ opposite to the wall. These variations are amplified at larger differences between cell and matrix stiffness. Figure 4.7B shows that the density of integrin proteins is less uniform when the ratio of the matrix to the cell stiffness is higher. In contrast, by virtue of the linearity of the equations defining the apparent stiffness and the number of adhesions, different values of E_c and E_m for a fixed ratio E_m/E_c yield different apparent stiffness but identical adhesive protein distibutions (data not shown). Therefore, the decrease in uniformity in the distribution of adhesive proteins observed when the the

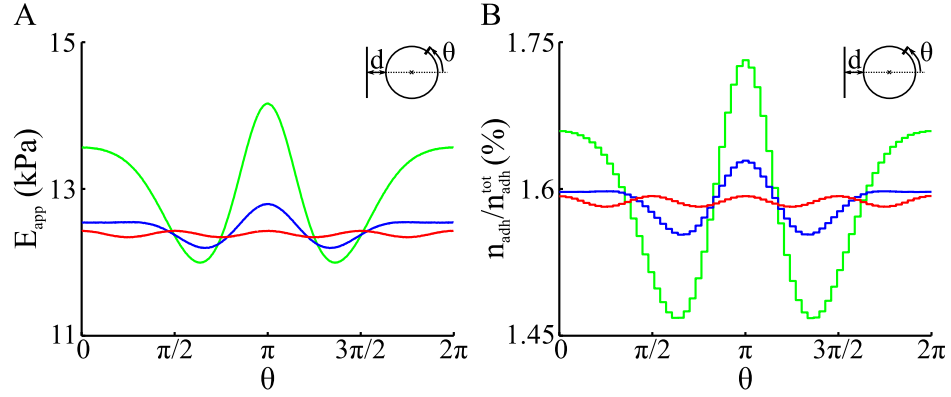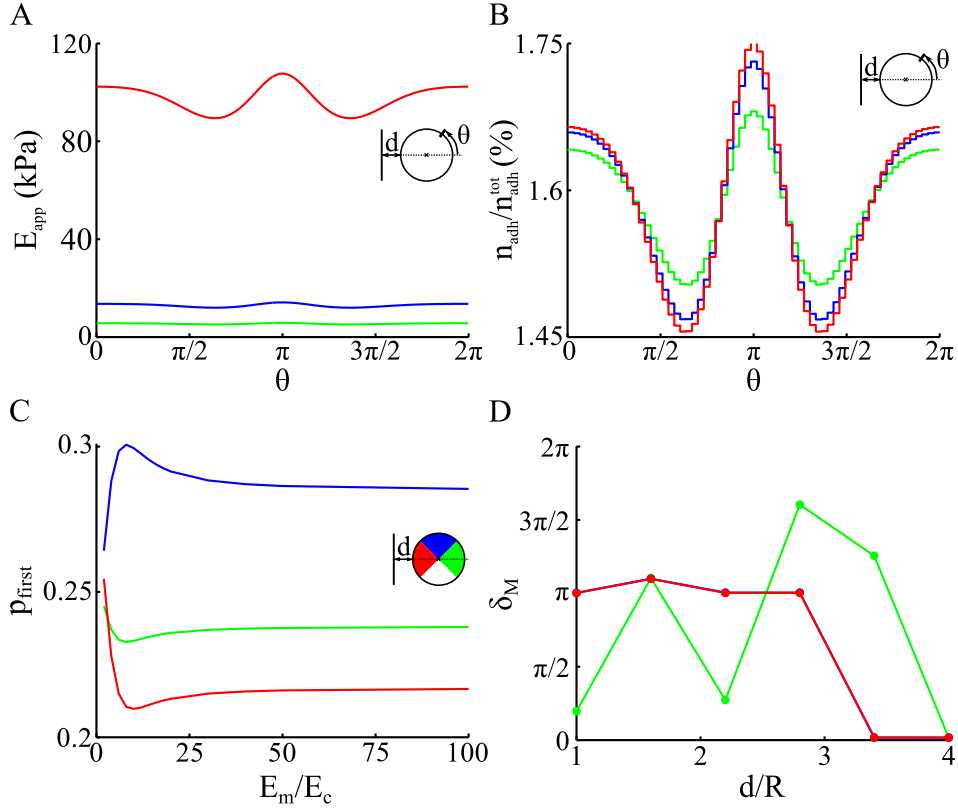FIGURE 4.7: Sensitivity of the results to the ratio of matrix stiffness to cell stiffness. A and B: Apparent stiffness (A) and relative number of integrins in the adhesions (B) as a function of the position angle θ, for $E_m/E_c = 2$ (green line), $E_m/E_c = 10$ (blue line), $E_m/E_c = 100$ (red line). The insets in A and B show the cell (disk) and the nearest wall (line) as well as the definition of d and θ. C: Probability that the first detachment occurs along $-\pi/4 \leq \theta \leq \pi/4$ (green line and green region in the inset), along $\pi/4 \leq \theta \leq 3\pi/4$ (blue line and blue region in the inset), or along $3\pi/4 \leq \theta \leq 5\pi/4$ (red line and red region in the inset) as a function of the ratio of matrix to cell stiffness. D: Preferred direction of migration as a function of the distance from the wall normalized by the cell radius. In this example, $E_c = 1$ kPa, $\nu_c = 0.4$, $\nu_m = 0.25$, and $n_{adh}^{tot} = 1000$, $d = R$ in panels A, B, and C.

matrix-cell Young's modulus ratio increases is a result of the ratio and not of the absolute increase in matrix stiffness.

The probability that the first detachment occurs in the region between θ_1 and θ_2, given by equation (4.24), is represented in figure 4.7C as a function of matrix-cell Young's modulus ratio for $\theta_1 = -\pi/4$, $\theta_2 = \pi/4$ (green line), $\theta_1 = \pi/4$, $\theta_2 = 3\pi/4$ (blue line), and $\theta_1 = 3\pi/4$, $\theta_2 = 5\pi/4$ (red line). The probability to first detach near the wall decreases rapidly as the matrix-cell Young's modulus ratio increases, attains a minimum around $E_m/E_c = 10$, and then increases very slowly. This non-monotonic behavior is due to the expression of the rate of detachment (equation (4.12)). Two contributions are involved, one of which drives the rate of detachment at small force (small E_m/E_c) and the other at high force (high E_m/E_c). When the matrix is relatively soft compared to the cell (small E_m/E_c), the first detachment has a similar probability to occur in

the three regions. This is consistent with the absence of a clear preferred direction of migration exhibited by figure 4.7D in the case of $E_m/E_c = 2$. On the other hand, figure 4.7D shows that both $E_m/E_c = 10$ and $E_m/E_c = 100$ yield a clear preferred direction of migration towards the wall when the cell is near the wall and away from the wall otherwise.

We also investigate the role of the cell and matrix Poisson's ratio. Figure 4.8A shows the apparent stiffness felt at the cell border for matrix Poisson's ratio $\nu_m = 0.4$ (solid line) and $\nu_m = 0.1$ (dashed line), and cell Poisson's ratio $\nu_c = 0.4$ (red line) and $\nu_c = 0.1$ (blue line). The results show that the apparent stiffness increases with the cell Poisson's ratio (red lines versus blue lines) whereas it decreases when the matrix Poisson's ratio increases (solid lines versus dashed lines). The greater its Poisson's ratio, the more a material can deform in the direction transverse to stimulation and the less compressible it is. When ν_m increases, the deformation in the direction normal to the cell−matrix border can be balanced by deformation in the transverse direction, and more deformation is needed to accommodate this reorganization. On the other hand, this reorganization is not possible in the cell because the transverse direction is itself subjected to constraints, and the incompressibility of the material prevents large deformations. It should be noted that the sensitivity of apparent stiffness to Poisson's ratio is small compared to the sensitivity to the matrix-cell stiffness ratio (figure 4.7A). Spanning the spectrum of possible Poisson's ratios yields a difference of only a few kPa in apparent stiffness, whereas changes in the ratio of the Young's moduli can change apparent stiffness by order of magnitudes.

The distribution of adhesive proteins in the attachment regions is depicted in figure 4.8B for the same values of the cell and matrix Poisson's ratio as in figure 4.8A. Only the cell Poisson's ratio has a significant effect on the distribution of adhesive proteins, and a greater cell Poisson's ratio is associated with a more uniform distribution. Indeed, in the limit of an incompressible cell, it would be almost impossible to deform the cell border, and the cell would feel an almost uniform and very high apparent stiffness.

Figure 4.8C depicts the probability that the first detachment occurs either in the positive x-direction region of the cell border (green line and green region in the inset), in the positive y-direction region of the cell (blue line and blue region in the inset), or in the negative x-direction region (red line and red region in the inset) as a function of the cell Poisson's ratio. Two values of the matrix Poisson's ratio are investigated: $\nu_m = 0.4$ (solid line) and $\nu_m = 0.1$ (dashed line). The probability of first detachment in any of the three regions depends very weakly on the matrix Poisson's ratio; this is a consequence of the very small effect of matrix Posisson's ratio on the distribution of adhesive proteins (figure 4.8B). Consistent with the increase in the uniformity of
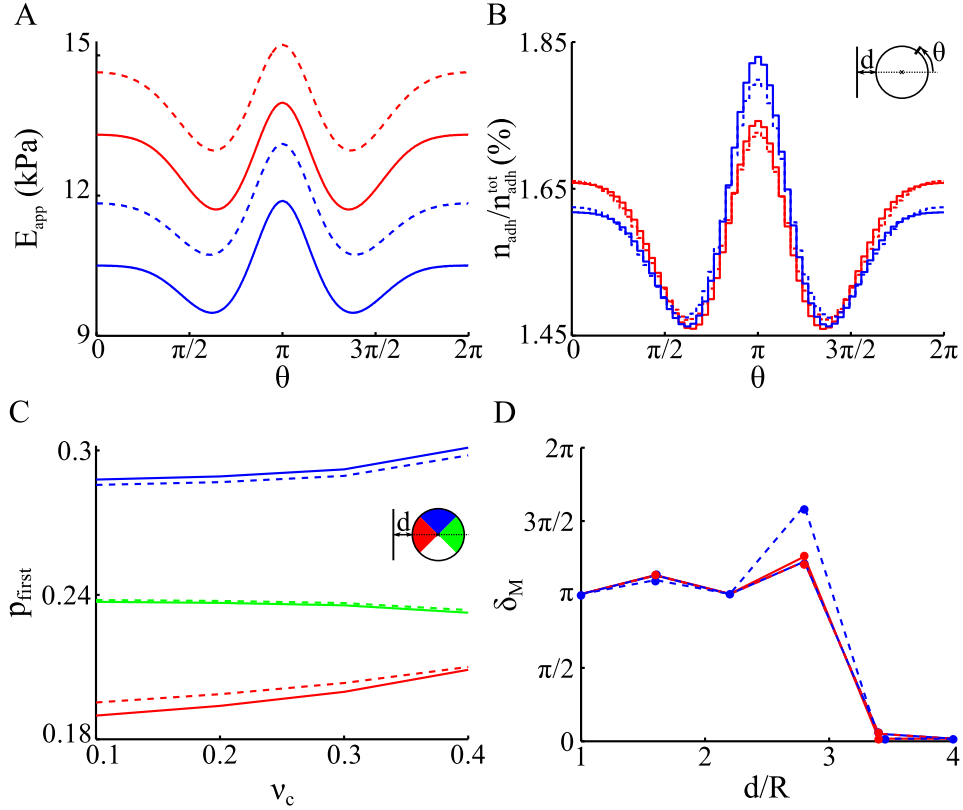
FIGURE 4.8: Sensitivity of the results to the matrix and cell Poisson's ratio, ν_m and ν_c. A and B: Apparent stiffness (A) and relative number of integrins in the adhesions (B) as a function of the position angle θ. The inset in B shows the cell (disk) and the nearest wall (line) as well as the definition of d and θ. C: Probability that the first detachment occurs along $-\pi/4 \leq \theta \leq \pi/4$ (green line and green region in the inset), along $\pi/4 \leq \theta \leq 3\pi/4$ (blue line and blue region in the inset), or along $3\pi/4 \leq \theta \leq 5\pi/4$ (red line and red region in the inset) as a function of the cell Poisson's ratio for $\nu_m = 0.4$ (solid lines) and $\nu_m = 0.1$ (dashed lines). D: Preferred direction of migration as a function of the distance to the wall normalized by the cell radius. In this example, $E_c = 1$ kPa, $E_m = 10$ kPa, $n_{adh}^{tot} = 1000$, and $d = R$ in panels A, B, and C. $\nu_m = 0.4$ (solid lines), $\nu_m = 0.1$ (dashed lines), $\nu_c = 0.4$ (red lines) and $\nu_c = 0.1$ (blue lines) in panels A, B, and D.

adhesive protein distribution, an increase in cell Poisson's ratio yields a decrease in the difference in the probability of first detachment among the three regions. However, this effect is small compared to the effect of a decrease in the ratio of matrix-cell Young's modulus (figure 4.7C).

The preferred direction of migration, δ_M is shown in figure 4.8B as a function of the cell−wall distance for different values of the cell and matrix Poisson's ratio. As in the other examples (see figures 4.5D and 4.6D), the cell migrates towards the wall, $\delta_M \approx \pi$, as long as it is sufficiently close to the wall and away from the wall otherwise.

4.3.5 Sensitivity to the total number of adhesions

Thus far, we have always considered a fixed total number of adhesive proteins $n_{adh}^{tot} = 1000$, which corresponds to the typical value found in the literature. We now investigate the sensitivity of our results to this value. Figure 4.9 shows the probability that the first detachment occurs in the positive x-direction region of the cell border (green line and green region in the inset), in the positive y-direction region (blue line and blue region in the inset), or in the negative x-direction region (red line and red region in the inset) as a function of the total number of adhesions. When the total number of adhesive proteins
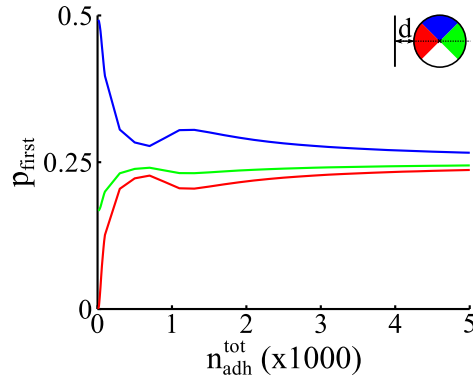
FIGURE 4.9: Probability that the first detachment occurs along $-\pi/4 \leq \theta \leq \pi/4$ (green line and green region in the inset), along $\pi/4 \leq \theta \leq 3\pi/4$ (blue line and blue region in the inset), or along $3\pi/4 \leq \theta \leq 5\pi/4$ (red line and red region in the inset) as a function of the total number of integrins at the membrane, n_{adh}^{tot}. In this example, $E_c = 1$ kPa, $E_m = 10$ kPa, $\nu_c = 0.4$, $\nu_m = 0.25$, and $d = R$.

is very high, the relative difference in force per adhesion along the cell border decreases:

$$\frac{F_i}{n_{adh}^i} - \frac{F_j}{n_{adh}^j} \approx \frac{<F_i, F_j>}{n_{adh}^{tot}} \left(\frac{n_{adh}^{tot}}{n_{adh}^i} - \frac{n_{adh}^{tot}}{n_{adh}^j} \right), \tag{4.25}$$

here the second part does not depend on n_{adh}^{tot}, hence the difference in force per adhesion between adhesion i and adhesion j decreases when the total number of adhesive proteins increases. Thus, the force per adhesion is more uniform around the cell, and the first detachment is equally likely to occur in one region or another. In contrast, when there are very few adhesive proteins, the difference in force per adhesion is large, and the distribution of adhesive proteins become critical in determining where the first detachment occurs. In the extreme case where only a single adhesion protein is available, the position of this protein on the cell border would by itself determine the direction of migration. However, in such cases, the initial probing of the mechanical environment would not be possible. Thus, these cases are of little relevance here.

For biologically relevant cases where $n_{adh}^{tot} \geq 500$, we observe that the probability to first detach in the negative x region shows a dip at $n_{adh}^{tot} \sim 1200$ (red data in figure

4.9); this is associated with a local maximum in the probability to first detach in the positive y region. This non-monotonic behavior is attributable to the expression of the rate of dissociation of the adhesive proteins under force (equation (4.12)). The rate of detachment at small force (high n_{adh}^{tot}) and at high force (small n_{adh}^{tot}) is driven by different contributions, and intermediate force yields the non-monotonic behavior.

4.4   Discussion

4.4.1   The apparent stiffness as a measure of the surrounding mechanical properties

Cell behavior, and in particular cell morphology, migration, and differentiation, have been shown to be dependent on matrix stiffness (Ehrbar et al., 2011, Engler et al., 2006, Hakkinen et al., 2010). More than its intrinsic mechanical properties, the mechanical state of the matrix, for instance its relaxation state or the presence of obstacles, has been shown to be critical for determining cell behavior (Cukierman et al., 2002, Lo et al., 2000). How cells feel these cues is poorly understood. It has been shown that cells adhere to their matrix, and that these adhesions mediate mechanical communication between the cell and the matrix (Cukierman et al., 2001, 2002, Lauffenberger and Horwitz, 1996). Application of traction forces at these adhesion sites by the contractile actomyosin machinery is key in both 2D and 3D processes (Friedl and Bröcker, 2000, Harris et al., 1980). Following these observations, we introduce the concept of apparent stiffness of the matrix, defined as the ratio of the stress actively applied by the actomyosin machinery at the cell−matrix interface to the resulting strain at the membrane (equation (4.7)). Our results show that the apparent stiffness is of the same order of magnitude as the matrix Young's modulus (figure 4.7A), but that it is also influenced by the matrix and cell Poisson's ratio as well as the presence of an obstacle (in our case a wall) in the matrix.

The apparent stiffness is shown to increase when the matrix Poisson's ratio decreases (figure 4.8A). The Poisson's ratio is a measure of the ability of the matrix to deform in the direction transverse to mechanical stimulation; in polymers, Poisson's ratio has been shown to decrease with polymer connectivity (Greaves et al., 2011). Thus, the dependence of the apparent stiffness on the matrix Poisson's ratio observed here is consistent with experimental results showing that cells behave similarly in highly crosslinked gels and in stiff gels (Ehrbar et al., 2011, Even-Ram and Yamada, 2005).

The dependence of the apparent stiffness on the cell mechanical properties is more difficult to position within an experimental context as experiments do not usually focus on this parameter. However, a number of studies have reported that different cell types, which have different mechanical properties (Balland et al., 2006), exhibit different behavior (Sieminski et al., 2004).

Our results also predict a dependence of the apparent stiffness on the presence of an obstacle in the matrix (figure 4.5A). The apparent stiffness felt by the cell is shown to increase near the obstacle, which is consistent with experiments showing a similar dependence in the vicinity of other cells or upon local manipulation of the substrate with a microneedle (Lo et al., 2000).

4.4.2   Apparent stiffness–based migration

Similar to migration on a 2D substrate, mesenchymal migration in a 3D matrix involves three steps of protrusion and formation of nascent adhesions with the matrix, cell contraction and establishment of a gradient of adhesions and traction forces at the cell border, and detachment of the low-adhesion part of the cell and displacement of the cell body (Friedl and Bröcker, 2000, Ridley et al., 2003). Our model of the two last steps reproduces the existence of a rear edge that experiences higher forces and has to detach to allow migration and of a front edge towards which the cell body is pulled (figure 4.4). It predicts preferential migration towards the region of greater apparent stiffness for sufficiently high stiffness gradients, which is consistent with experimental work by Hadjipanayi et al. (2009).

We model the presence of an obstacle by having a wall closer to the cell. Up to a cell−obstacle distance of $\sim 3.5R = 35~\mu$m, the cell feels and migrates towards the obstacle. Dependence of cell migration on the proximity of an obstacle, which can also be another cell, has been reported experimentally (Lo et al., 2000, Reinhart-King et al., 2008). In particular, Reinhart-King et al. (2008) suggested that cells communicate via the traction forces they exert on their substrate, and showed that this influence is felt up to a few tens of micrometers. Moreover, they found that the communication is optimal at an intermediate stiffness, which is consistent with our results (figure 4.7C).

In the present model, we have considered a uniform elastic matrix. In vivo, the extracellular matrix is a fibrous material, and experiments have shown that cell mesenchymal migration is guided by these fibers (Doyle et al., 2009, Petrie et al., 2009). At the scale of the cell, fibers will be felt as local stiffer regions, and our model predicts that the cell will migrate along these directions. Extension of the present model to the case

of a fibrous hyperelastic matrix (Spencer et al., 1984, Weiss et al., 1996) would allow one to study this specific problem.

4.4.3 Comments on the protrusion step

The present model lacks the protrusion step of the migration process. Protrusion in 3D matrices is particularly important as the cell has to overcome effects of the matrix that fully surrounds it (Ehrbar et al., 2011). Addition of a step of protrusion to the model would allow studying migration speed (Zaman et al., 2006) and may allow understanding the switch from mesenchymal migration to amoeboid migration at low matrix stiffness (Ehrbar et al., 2011). However, protrusion characteristically happens at the leading edge, where the cell remains attached to the matrix (Petrie et al., 2009). Therefore, addition of a step of protrusion would not be expected to change the present findings on cell migration directionality.

4.4.4 A first step in cell network formation?

Endothelial cells can spontaneously assemble into networks, which is key to the formation of new blood vessels in the process of angiogenesis (Jeon et al., 2014, Whisler et al., 2012). Diverse chemical and mechanical cues from the extracellular matrix have been shown to drive this process (Davis and Senger, 2005), among which are the matrix stiffness, traction force generation, and adhesion to the matrix (Sieminski et al., 2004). Our model integrates these mechanical cues and explains communication between two cells and migration towards each other, a key step in formation of networks of cells. Such a mechanism is in good agreement with the experimental prediction that traction forces play a key role in cell–cell communication (Reinhart-King et al., 2008) and coordinated migration (Lo et al., 2000, Reinhart-King et al., 2008). Moreover, we find that migration of two cells towards one another is optimum at intermediate to high stiffness (figures 4.7C and D) and at low number of adhesions (figure 4.9), a result consistent with experimental work by Califano and Reinhart-King (2008). However, in that study, they also found an efficient formation of networks at low stiffness and high density of adhesions, and they suggested that optimal formation of networks requires that cell–cell junctions are more favorable than cell–matrix adhesions. To discriminate between the role of mechanics in migration on the one hand and in formation of cell–cell adhesions on the other hand, a future study shoud focus on the step where two cells are very close to each other and have the choice to either adhere or to migrate away from one another.

4.4.5 Definition of the apparent stiffness

We have defined the apparent stiffness as the ratio of the actomyosin active stress applied at the cell border to the cell radial strain (equation (4.7)). How this strain is transduced to a biological response, here the density of adhesions, is not known, but it has been shown in 2D that adhesions develop and elongate along the force direction (Balaban et al., 2001). Therefore, the strain in this direction appears to be a good candidate.

Figure 4.10 shows the apparent stiffness along the cell border defined with either the tangential strain (figure 4.10A), i.e.:

$$E_{app}(x, y) = \frac{\sigma_0}{|\mathbf{t}.\epsilon_\mathbf{c}(\mathbf{x}, \mathbf{y}).\mathbf{t}|}, \tag{4.26a}$$

where $\mathbf{t}$ is the local vector tangential to the border, or with the volumic variation (figure 4.10B):

$$E_{app}(x, y) = \frac{\sigma_0}{|1 - \mathrm{tr}(\epsilon_\mathbf{c}(\mathbf{x}, \mathbf{y}))|}. \tag{4.26b}$$

Both definitions yield a non-uniform apparent stiffness that depends on the presence
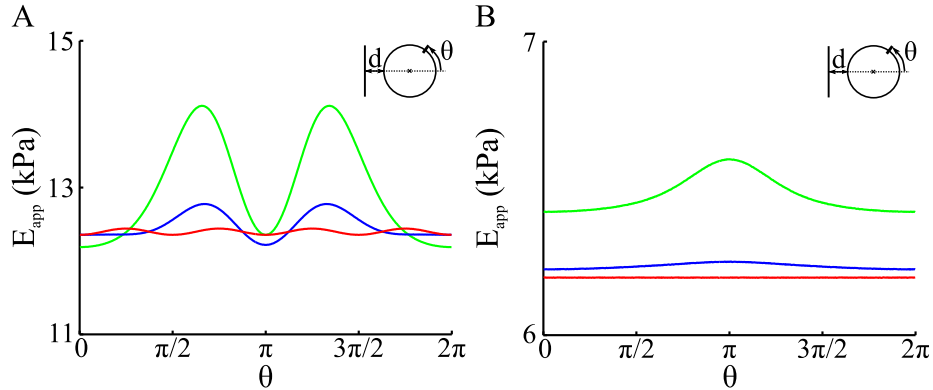
FIGURE 4.10: Apparent stiffness defined with either the tangential strain (A) or the volumic strain (B) as a function of the position angle θ, for cell−wall distances $d = R$ (green line), $d = 2.5R$ (blue line), and $d = 4R$ (red line). The insets show the cell (disk) and the nearest wall (line) as well as the definition of d and θ. In this example, $E_c = 1$ kPa, $E_m = 10$ kPa, $\nu_c = 0.4$, and $\nu_m = 0.25$.

of the obstacle. However, the apparent stiffness based on volumic dilatation depends much more weakly on the vicinity to the wall, in particular compared to other definitions of the apparent stiffness (see figures 4.5A and 4.10A). Therefore, a mechanism of adhesion based on this signal seems unlikely or would require an amplification of the signal. The apparent stiffness based on the tangential strain is of particular interest as it may be related to the stretch of the membrane, which has been suggested as a potential mechanosensor. Here the dependence on the presence of the wall is significantly different from that of the radial strain-related apparent stiffness. However, the maximum

apparent stiffness still occurs in the mid circle closest to the wall ($\pi/2 \leq \theta \leq 3\pi/2$) and remains consistent with cellular migration towards the wall.

4.5 Conclusions

We have developed a model of the attachment and detachment steps of mesenchymal migration in a 3D matrix which integrates key mechanical cues, including adhesion to the matrix, application of forces to the matrix, and force dependent detachment of the rear edge of the cell. Our results show that our definition of the apparent stiffness sensed by the cell accounts not only for the Young's modulus of the matrix but more generally for the matrix mechanical state. In particular, an obstacle, such as a wall or another cell, is sensed by an increase in the apparent stiffness. Use of this apparent sitffness to define the distribution of adhesions at the cell border shows migration in the direction of the obstacle, with a dependence on matrix and cell mechanical properties. These results provide a first step in understanding the role of mechanics in collective migration of cells necessary to the formation of blood vessels. Further development of the model will allow addressing other questions, including contact guidance in fibrous matrices, the role of the protrusion step, and cell–cell adhesion upon encounter.

Chapter 5

Conclusions and Recommendations for Future Work

The theoretical models developed in this work combine current knowledge on cell interactions with its mechanical environment and classical engineering concepts in order to further our understanding of the role of mechanical cues in key processes such as mechanotransduction, development of atherogenesis, and cell migration.

Stress fibers are bundles of actin filaments and myosin motors that link to cell–matrix adhesions, cell–cell adhesions, and intracellular structures such as the nucleus (Alberts et al., 2002, Jaalouk and Lammerding, 2009). In vitro study of mechanotransduction often involves application of a force at the cell–matrix adhesion of an isolated cell, and stress fibers have been suggested as a candidate to transmit this force to discrete sites within the cell (Hu et al., 2003, Na et al., 2008). Based on these observations and on known stress fiber mechanical properties, we develop a model of force transmission in a network of viscoelastic prestressed stress fibers that link membrane proteins where the force is applied to intracellular sites. We use beam theory and a viscoelastic Kelvin Voigt model to describe strain evolution in a network of such fibers.

In vivo, diturbed flow regions, where shear stress is low and/or reversing, are associated with isotropic organization of stress fibers and with increased risk of atherosclerotic lesions (Hahn and Schwartz, 2009). In vitro, the response of a cell to force is dependent on the forcing frequency and direction with respect to stress fiber alignment (Hu et al., 2004). To discriminate between the respective role of stress fiber alignment and of external force characteristics, we initially focused on the case of a simple network of two stress

fibers, in which fiber alignment is accounted for by the angle between the two fibers. The results demonstrate that the dynamics of force transmission by the fibers is consistent with very rapid force transmission directly to intracellular sites such as the nucleus and mechanochemical conversion at these intracellular sites (Na et al., 2008). The model also predicts the anisotropy in mechanical signal transmission observed experimentally (Hu et al., 2003, 2004). Stretching of cells stripped of their membranes triggers an increase in binding to the cytoskeleton of some proteins, such as focal adhesion kinase, p130Cas and paxillin (Sawada and Sheetz, 2002, Tamada et al., 2004). Therefore, we propose that stress fiber strain, elicited by cell stretching in these experiments and by transmission of an externally applied force in our model, may be a mechanism of mechanical signal conversion to a chemical signal. Such a mechanism would provide a direct link between stress fiber organization, external force characteristics, and forces on the nucleus that may regulate gene expression.

The model also predicts a critical role for stress fiber alignment in force transmission. To experimentally test these predictions, one approach would be to follow the activation of a rapid force-induced biological response such as the activation of the protein Src in a manner similar to what has been done in previous studies (Na et al., 2008, Wang et al., 2005) but in cells whose stress fiber network can be controlled. This experiment is currently being set up in our laboratory, where control of stress fiber organization is accomplished via surface micropatterning. We hope and expect that the experimental results that will emerge will inform strategies for future evolution of the present model.

To further understand force transduction in cells, we applied the model of force transmission via stress fibers to a monolayer of cells. Stress fibers of neigboring cells are connected at cell–cell adhesions and thus form a single network that spans the entire monolayer. Adhesion to the underlying matrix was modeled by a spring force at the nodes of the network. The respective roles in force transmission of external force characteristics, network connectivity, and stress fiber alignment were investigated. First, comparison of idealized and real stress fiber networks showed that the overall alignment of the network determines force transmission quite independently from the network connectivity. The model predicts that under disturbed flow conditions, an isotropic stress fiber organization yields the lowest strain configuration whereas for undisturbed flow conditions, strain and strain variations are minimized by having an aligned stress fiber organization. These results suggest that the organization of stress fiber networks in cells may be driven by a process of minimization of strain and strain variations. Our results also predict that in isotropic stress fiber configurations, the partitioning of strain in the monolayer depends on force direction. Such polarization of the monolayer with respect to force direction may be involved in the mechanism of cell alignment with flow. Overall, our model suggests that stress fiber strain in disturbed flow is

expected to be drastically different from that in undisturbed flow conditions. If stress fiber strain is involved in endothelial cell mechanotransduction, then the present results provide valuable insight into the observed correlations between disturbed flow shear stress, endothelial cell morphology, and atherosclerosis development.

Despite the apparent simplicity of the present model, it appears to capture a number of important experimentally observed features of the interplay among stress fiber organization, external force characteristics, and force transmission profiles in cellular monolayers. Progressively adding complexity to the model may allow us to test the role of additional parameters. For instance, the potential contributions of membrane and cytoplasmic resistance to deformation could be modeled by adding resistances to the motion of the network nodes. Studying three dimensional stress fiber networks would allow testing the role of this third dimension. An additional promising future direction would be to subject the cellular monolayer to an external force distribution that would mimic a realistic shear stress profile, which would allow studying the role of different shear stress profiles as well as shear stress gradients. The main challenge in this regard is numerical since such a study needs to be carried out on a sufficiently large network.

In the final model, we investigated the role of mechanical cues and equilibra in the attachment and detachment steps of mesenchymal migration of a cell in a three dimensional matrix. Key experimental observations informing this model include matrix probing by actomyosin-driven contraction of the cell, matrix rigidity–dependent distribution of adhesions, and tension–dependent detachment of the adhesions (Lauffenberger and Horwitz, 1996, Ridley et al., 2003). We modeled actomyosin-driven contraction as an active normal stress applied at the cell membrane. Consistent with cell–matrix mechanical connection at adhesion sites, this active stress is split between the matrix and the cell at the interface where they are connected. Using the engineering definition of stiffness, we defined the apparent stiffness of the cell as the ratio between the active stress and the resulting cell membrane strain. Adhesions were distributed proportionally to the apparent stiffness and were then made to detach with a probability that depends on the force applied on the adhesion. Our definition of apparent stiffness integrates intrinsic matrix mechanical properties and other cues that are felt by the cell as an increase in matrix rigidity, such as physical obstacles or a mechanical singularity in the matrix (Doyle et al., 2009). The model predicts preferential migration in the direction of higher stiffness, and thus explains migration of cells towards obstacles such as other cells (Lo et al., 2000) or along local stiffer fibers in the matrix (Doyle et al., 2009).

Further work is planned to realize a series of random migration processes to determine the strength of the attraction exerted by higher apparent stiffness regions. Several directions can be taken in future work. One possible path is to close the migration

loop by modeling the protrusion step, which, while not expected to play a critical role in determining the migration directionality, probably plays an important role in migration speed. Competition between cell–cell adhesions and cell–matrix adhesions has been shown to play a critical role in the formation of blood vessels. Therefore, a second possible path is to study this competition, for instance by modeling two neighboring cells in a matrix. The extracellular matrix is composed of various constituents including collagen fibers. It has been shown that cells tend to migrate along these fibers (Doyle et al., 2009), which is consistent with the model prediction that cells migrate in the direction of higher apparent matrix rigidity. Cell contraction changes the organization of these fibers, thus easing the cell path. A future study could investigate this contact guidance phenomenon. To this end, the matrix could be modeled as a fibrous hyperelastic material (Spencer et al., 1984, Weiss et al., 1996) whose fiber characteristics are updated depending on traction forces exerted by the cell on the matrix.

Bibliography

Alberts, B., Johnson, A., Lewis, J., Raff, M., Roberts, K., Walter, P. et al. (2002), 'Molecular biology of the cell'.

Ashkin, A., Schütze, K., Dziedzic, J., Euteneuer, U. and Schliwa, M. (1990), 'Force generation of organelle transport measured in vivo by an infrared laser trap', *Nature* **348**, 346–348.

Balaban, N. Q., Schwarz, U. S., Riveline, D., Goichberg, P., Tzur, G., Sabanay, I., Mahalu, D., Safran, S., Bershadsky, A., Addadi, L. et al. (2001), 'Force and focal adhesion assembly: a close relationship studied using elastic micropatterned substrates', *Nat Cell Biol* **3**(5), 466–472.

Balland, M., Desprat, N., Icard, D., Féréol, S., Asnacios, A., Browaeys, J., Hénon, S. and Gallet, F. (2006), 'Power laws in microrheology experiments on living cells: Comparative analysis and modeling', *Phys Rev E* **74**(2), 021911.

Barakat, A. I., Lieu, D. K. and Gojova, A. (2006), 'Secrets of the code: do vascular endothelial cells use ion channels to decipher complex flow signals?', *Biomaterials* **27**(5), 671–678.

Barbee, K., Mundel, T., Lal, R. and Davies, P. (1995), 'Subcellular distribution of shear stress at the surface of flow-aligned and nonaligned endothelial monolayers', *Am J Physiol* **268**(4), H1765–1772.

Bausch, A. R., Ziemann, F., Boulbitch, A. A., Jacobson, K. and Sackmann, E. (1998), 'Local measurements of viscoelastic parameters of adherent cell surfaces by magnetic bead microrheometry', *Biophys J* **75**(4), 2038–2049.

Bell, G. I. (1978), 'Models for the specific adhesion of cells to cells', *Science* **200**(4342), 618–627.

Bonnet, M. and Frangi, A. (2006), *Analyse des solides déformables par la méthode des éléments finis*, Editions Ecole Polytechnique.

Brakebusch, C. and Fässler, R. (2003), 'The integrin–actin connection, an eternal love affair', *EMBO J* **22**(10), 2324–2333.

Califano, J. P. and Reinhart-King, C. A. (2008), 'A balance of substrate mechanics and matrix chemistry regulates endothelial cell network assembly', *Cell Mol Bioeng* **1**(2-3), 122–132.

Caro, C., Fitz-Gerald, J. and Schroter, R. (1969), 'Arterial wall shear and distribution of early atheroma in man', *Nature* **223**, 1159–1161.

Charras, G. T. and Horton, M. A. (2002), 'Determination of cellular strains by combined atomic force microscopy and finite element modeling', *Biophys J* **83**(2), 858–879.

Chatzizisis, Y. S., Coskun, A. U., Jonas, M., Edelman, E. R., Feldman, C. L. and Stone, P. H. (2007), 'Role of endothelial shear stress in the natural history of coronary atherosclerosis and vascular remodeling', *J Am Coll Cardiol* **49**(25), 2379–2393.

Chen, C. S., Tan, J. and Tien, J. (2004), 'Mechanotransduction at cell-matrix and cell-cell contacts', *Annu Rev Biomed Eng* **6**, 275–302.

Choquet, D., Felsenfeld, D. P. and Sheetz, M. P. (1997), 'Extracellular matrix rigidity causes strengthening of integrin–cytoskeleton linkages', *Cell* **88**(1), 39–48.

Cines, D. B., Pollak, E. S., Buck, C. A., Loscalzo, J., Zimmerman, G. A., McEver, R. P., Pober, J. S., Wick, T. M., Konkle, B. A., Schwartz, B. S. et al. (1998), 'Endothelial cells in physiology and in the pathophysiology of vascular disorders', *Blood* **91**(10), 3527–3561.

Colombelli, J., Besser, A., Kress, H., Reynaud, E. G., Girard, P., Caussinus, E., Haselmann, U., Small, J. V., Schwarz, U. S. and Stelzer, E. H. (2009), 'Mechanosensing in actin stress fibers revealed by a close correlation between force and protein localization', *J Cell Sci* **122**(10), 1665–1679.

Costa, M., Marchi, M., Cardarelli, F., Roy, A., Beltram, F., Maffei, L. and Ratto, G. M. (2006), 'Dynamic regulation of erk2 nuclear translocation and mobility in living cells', *J Cell Sci* **119**(23), 4952–4963.

Cukierman, E., Pankov, R., Stevens, D. R. and Yamada, K. M. (2001), 'Taking cell-matrix adhesions to the third dimension', *Science* **294**(5547), 1708–1712.

Cukierman, E., Pankov, R. and Yamada, K. M. (2002), 'Cell interactions with three-dimensional matrices', *Curr Opin Cell Biol* **14**(5), 633–640.

Cunningham, K. S. and Gotlieb, A. I. (2004), 'The role of shear stress in the pathogenesis of atherosclerosis', *Lab Invest* **85**(1), 9–23.

Davies, P. F. (2008), 'Hemodynamic shear stress and the endothelium in cardiovascular pathophysiology', *Nat Clin Pract Cardiovasc Med* **6**(1), 16–26.

Davies, P. F., Robotewskyj, A. and Griem, M. (1993), 'Endothelial cell adhesion in real time. measurements in vitro by tandem scanning confocal image analysis.', *J Clin Invest* **91**(6), 2640.

Davies, P. F., Robotewskyj, A. and Griem, M. L. (1994), 'Quantitative studies of endothelial cell adhesion. directional remodeling of focal adhesion sites in response to flow forces.', *J Clin Invest* **93**(5), 2031.

Davis, G. E. and Senger, D. R. (2005), 'Endothelial extracellular matrix biosynthesis, remodeling, and functions during vascular morphogenesis and neovessel stabilization', *Circ Res* **97**(11), 1093–1107.

Deguchi, S., Ohashi, T. and Sato, M. (2006), 'Tensile properties of single stress fibers isolated from cultured vascular smooth muscle cells', *J Biomech* **39**(14), 2603–2610.

del Rio, A., Perez-Jimenez, R., Liu, R., Roca-Cusachs, P., Fernandez, J. M. and Sheetz, M. P. (2009), 'Stretching single talin rod molecules activates vinculin binding', *Science* **323**(5914), 638–641.

Dewey, C., Gimbrone, M., Davies, P. and Bussolari, S. (1981), 'The dynamic response of vascular endothelial cells to fluid shear stress', *J Biomech Eng* **103**(3), 177–185.

Di Stefano, I., Koopmans, D. R. and Langille, B. L. (1998), 'Modulation of arterial growth of the rabbit carotid artery associated with experimental elevation of blood flow', *J Vasc Res* **35**(1), 1–7.

Doyle, A. D., Wang, F. W., Matsumoto, K. and Yamada, K. M. (2009), 'One-dimensional topography underlies three-dimensional fibrillar cell migration', *J Cell Biol* **184**(4), 481–490.

Duong, H., Wu, B. and Tawil, B. (2009), 'Modulation of 3d fibrin matrix stiffness by intrinsic fibrinogen–thrombin compositions and by extrinsic cellular activity', *Tissue Eng Part A* **15**(7), 1865–1876.

Ehrbar, M., Sala, A., Lienemann, P., Ranga, A., Mosiewicz, K., Bittermann, A., Rizzi, S., Weber, F. and Lutolf, M. (2011), 'Elucidating the role of matrix stiffness in 3d cell migration and remodeling', *Biophys J* **100**(2), 284–293.

Engler, A. J., Sen, S., Sweeney, H. L. and Discher, D. E. (2006), 'Matrix elasticity directs stem cell lineage specification', *Cell* **126**(4), 677–689.

Evans, E. and Ritchie, K. (1997), 'Dynamic strength of molecular adhesion bonds', *Biophys J* **72**(4), 1541–1555.

Even-Ram, S. and Yamada, K. M. (2005), 'Cell migration in 3d matrix', *Curr Opin Cell Biol* **17**(5), 524–532.

Faxon, D. P., Fuster, V., Libby, P., Beckman, J. A., Hiatt, W. R., Thompson, R. W., Topper, J. N., Annex, B. H., Rundback, J. H., Fabunmi, R. P. et al. (2004), 'Atherosclerotic vascular disease conference writing group iii: pathophysiology', *Circ* **109**(21), 2617–2625.

Feneberg, W., Aepfelbacher, M. and Sackmann, E. (2004), 'Microviscoelasticity of the apical cell surface of human umbilical vein endothelial cells (huvec) within confluent monolayers', *Biophys J* **87**(2), 1338–1350.

Flaherty, J. T., Pierce, J. E., Ferrans, V. J., Patel, D. J., Tucker, W. K. and Fry, D. L. (1972), 'Endothelial nuclear patterns in the canine arterial tree with particular reference to hemodynamic events', *Circ Res* **30**(1), 23–33.

Fletcher, D. A. and Mullins, R. D. (2010), 'Cell mechanics and the cytoskeleton', *Nature* **463**(7280), 485–492.

Florian, J. A., Kosky, J. R., Ainslie, K., Pang, Z., Dull, R. O. and Tarbell, J. M. (2003), 'Heparan sulfate proteoglycan is a mechanosensor on endothelial cells', *Circ Res* **93**(10), e136–e142.

Friedl, P. and Bröcker, E.-B. (2000), 'The biology of cell locomotion within three-dimensional extracellular matrix', *Cell Mol Life Sci* **57**(1), 41–64.

Friedl, P. and Wolf, K. (2009), 'Proteolytic interstitial cell migration: a five-step process', *Cancer Metast Rev* **28**(1-2), 129–135.

Friedland, J. C., Lee, M. H. and Boettiger, D. (2009), 'Mechanically activated integrin switch controls $\alpha 5 \beta 1$ function', *Science* **323**(5914), 642–644.

Galbraith, C., Skalak, R. and Chien, S. (1998), 'Shear stress induces spatial reorganization of the endothelial cell cytoskeleton', *Cell Motil and the Cytoskel* **40**(4), 317–330.

Geiger, B., Spatz, J. P. and Bershadsky, A. D. (2009), 'Environmental sensing through focal adhesions', *Nat Rev Mol Cell Biol* **10**(1), 21–33.

Geuzaine, C. and Remacle, J.-F. (2009), 'Gmsh: A 3-d finite element mesh generator with built-in pre-and post-processing facilities', *Int J Numer Meth Eng* **79**(11), 1309–1331.

Glogauer, M., Arora, P., Yao, G., Sokholov, I., Ferrier, J. and McCulloch, C. (1997), 'Calcium ions and tyrosine phosphorylation interact coordinately with actin to regulate cytoprotective responses to stretching', *J Cell Sci* **110**(1), 11–21.

Goeckeler, Z. M. and Wysolmerski, R. B. (1995), 'Myosin light chain kinase-regulated endothelial cell contraction: the relationship between isometric tension, actin polymerization, and myosin phosphorylation.', *J Cell Biol* **130**(3), 613–627.

Gojova, A. and Barakat, A. I. (2005), 'Vascular endothelial wound closure under shear stress: role of membrane fluidity and flow-sensitive ion channels', *Journal of Applied Physiology* **98**(6), 2355–2362.

Gouget, C., Hwang, Y. and Barakat, A. I. (2014), 'Dynamics of mechanical signal transmission through prestressed stress fibers', *in review* .

Greaves, G. N., Greer, A., Lakes, R. and Rouxel, T. (2011), 'Poisson's ratio and modern materials', *Nat Mat* **10**(11), 823–837.

Guillot, C. and Lecuit, T. (2013), 'Mechanics of epithelial tissue homeostasis and morphogenesis', *Science* **340**(6137), 1185–1189.

Hadjipanayi, E., Mudera, V. and Brown, R. A. (2009), 'Guiding cell migration in 3d: a collagen matrix with graded directional stiffness', *Cell Motil Cytoskel* **66**(3), 121–128.

Hahn, C. and Schwartz, M. A. (2009), 'Mechanotransduction in vascular physiology and atherogenesis', *Nat Rev Mol Cell Biol* **10**(1), 53–62.

Haidekker, M. A., L'Heureux, N. and Frangos, J. A. (2000), 'Fluid shear stress increases membrane fluidity in endothelial cells: a study with dcvj fluorescence', *Am J Physiol-Heart Circ Physiol* **278**(4), H1401–H1406.

Hakkinen, K. M., Harunaga, J. S., Doyle, A. D. and Yamada, K. M. (2010), 'Direct comparisons of the morphology, migration, cell adhesions, and actin cytoskeleton of fibroblasts in four different three-dimensional extracellular matrices', *Tissue Eng Part A* **17**(5-6), 713–724.

Han, B., Bai, X.-H., Lodyga, M., Xu, J., Yang, B. B., Keshavjee, S., Post, M. and Liu, M. (2004), 'Conversion of mechanical force into biochemical signaling', *J Biol Chem* **279**(52), 54793–54801.

Harris, A. K., Wild, P. and Stopak, D. (1980), 'Silicone rubber substrata: a new wrinkle in the study of cell locomotion', *Science* **208**(4440), 177–179.

Harris, A. R., Peter, L., Bellis, J., Baum, B., Kabla, A. J. and Charras, G. T. (2012), 'Characterizing the mechanics of cultured cell monolayers', *Proc Natl Acad Sci* **109**(41), 16449–16454.

Hecht, F. (2012), 'New development in freefem++', *J Numer Math* **20**(3-4), 251–265.

Helmlinger, G., Geiger, R., Schreck, S. and Nerem, R. (1991), 'Effects of pulsatile flow on cultured vascular endothelial cell morphology', *J Biomech Eng* **113**(2), 123–131.

Hoffman, B. D., Grashoff, C. and Schwartz, M. A. (2011), 'Dynamic molecular processes mediate cellular mechanotransduction', *Nature* **475**(7356), 316–323.

Holzapfel, G. A. (2000), *Nonlinear solid mechanics*, Vol. 24, Wiley Chichester.

Hu, S., Chen, J., Butler, J. P. and Wang, N. (2005), 'Prestress mediates force propagation into the nucleus', *Biochem Biophys Res Commun* **329**(2), 423–428.

Hu, S., Chen, J., Fabry, B., Numaguchi, Y., Gouldstone, A., Ingber, D. E., Fredberg, J. J., Butler, J. P. and Wang, N. (2003), 'Intracellular stress tomography reveals stress focusing and structural anisotropy in cytoskeleton of living cells', *Am J Physiol-Cell Physiol* **285**(5), C1082–C1090.

Hu, S., Eberhard, L., Chen, J., Love, J. C., Butler, J. P., Fredberg, J. J., Whitesides, G. M. and Wang, N. (2004), 'Mechanical anisotropy of adherent cells probed by a three-dimensional magnetic twisting device', *Am J of Physiol-Cell Physiol* **287**(5), C1184–C1191.

Hu, S. and Wang, N. (2006), 'Control of stress propagation in the cytoplasm by prestress and loading frequency', *Mol Cell Biomech* **3**(2), 49.

Hwang, Y. and Barakat, A. I. (2012), 'Dynamics of mechanical signal transmission through prestressed stress fibers', *PloS One* **7**(4), e35343.

Hwang, Y., Gouget, C. L. M. and Barakat, A. I. (2012), 'Mechanisms of cytoskeleton-mediated mechanical signal transmission in cells', *Comm Int Biol* **5**(6), 538–542.

Hynes, R. O. (1987), 'Integrins: a family of cell surface receptors', *Cell* **48**(4), 549–554.

Ingber, D. E. (1997), 'Tensegrity: the architectural basis of cellular mechanotransduction', *Annu Rev Physiol* **59**(1), 575–599.

Ingber, D. E. (2006), 'Mechanical control of tissue morphogenesis during embryological development', *Int J Dev Biol* **50**(2/3), 255.

Irvine, D. J., Hue, K.-A., Mayes, A. M. and Griffith, L. G. (2002), 'Simulations of cell-surface integrin binding to nanoscale-clustered adhesion ligands', *Biophysical journal* **82**(1), 120–132.

Jaalouk, D. E. and Lammerding, J. (2009), 'Mechanotransduction gone awry', *Nat Rev Mol Cell Biol* **10**(1), 63–73.

Janmey, P. A. (1998), 'The cytoskeleton and cell signaling: component localization and mechanical coupling', *Physiol Rev* **78**(3), 763–781.

Jeon, J. S., Bersini, S., Whisler, J. A., Chen, M. B., Dubini, G., Charest, J. L., Moretti, M. and Kamm, R. D. (2014), 'Generation of 3d functional microvascular networks with human mesenchymal stem cells in microfluidic systems', *Integr Biol* **6**(5), 555–563.

Jin, M., Andricioaei, I. and Springer, T. A. (2004), 'Conversion between three conformational states of integrin i domains with a c-terminal pull spring studied with molecular dynamics', *Structure* **12**(12), 2137–2147.

Karcher, H., Lammerding, J., Huang, H., Lee, R. T., Kamm, R. D. and Kaazempur-Mofrad, M. R. (2003), 'A three-dimensional viscoelastic model for cell deformation with experimental verification', *Biophys J* **85**(5), 3336–3349.

Kholodenko, B. N., Hancock, J. F. and Kolch, W. (2010), 'Signalling ballet in space and time', *Nat Rev Mol Cell Biol* **11**(6), 414–426.

Kumar, S., Maxwell, I. Z., Heisterkamp, A., Polte, T. R., Lele, T. P., Salanga, M., Mazur, E. and Ingber, D. E. (2006), 'Viscoelastic retraction of single living stress fibers and its impact on cell shape, cytoskeletal organization, and extracellular matrix mechanics', *Biophys J* **90**(10), 3762–3773.

Lamalice, L., Le Boeuf, F. and Huot, J. (2007), 'Endothelial cell migration during angiogenesis', *Circ Res* **100**(6), 782–794.

Lämmermann, T. and Sixt, M. (2009), 'Mechanical modes of 'amoeboid'cell migration', *Curr Opin Cell Biol* **21**(5), 636–644.

Langille, B. L., Bendeck, M. P., Keeley, F. W. et al. (1989), 'Adaptations of carotid arteries of young and mature rabbits to reduced carotid blood flow', *Am J Physiol* **256**(4 Pt 2), H931–H939.

Lauffenberger, D. and Horwitz, A. (1996), 'Cell migration: a physically integrated molecular process', *Cell* **84**(3), 359–369.

Le Tallec, P. (2008), *Mécanique des milieux continus*, École polytechnique.

Leckband, D. E., le Duc, Q., Wang, N. and de Rooij, J. (2011), 'Mechanotransduction at cadherin-mediated adhesions', *Curr Opin Cell Biol* **23**(5), 523–530.

Lele, T. P., Pendse, J., Kumar, S., Salanga, M., Karavitis, J. and Ingber, D. E. (2006), 'Mechanical forces alter zyxin unbinding kinetics within focal adhesions of living cells', *J Cell Physiol* **207**(1), 187–194.

Levesque, M., Nerem, R. and Sprague, E. (1990), 'Vascular endottielial cell proliferation in culture and the influence of flow', *Biomaterials* **11**(9), 702–707.

Li, F., Redick, S. D., Erickson, H. P. and Moy, V. T. (2003), 'Force measurements of the $\alpha 5 \beta 1$ integrin–fibronectin interaction', *Biophys J* **84**(2), 1252–1262.

Li, S., Chen, B. P., Azuma, N., Hu, Y.-L., Wu, S. Z., Sumpio, B. E., Shyy, J. Y.-J. and Chien, S. (1999), 'Distinct roles for the small gtpases cdc42 and rho in endothelial responses to shear stress', *J Clin Invest* **103**(8), 1141–1150.

Li, Y.-S. J., Haga, J. H. and Chien, S. (2005), 'Molecular basis of the effects of shear stress on vascular endothelial cells', *J Biomech* **38**(10), 1949–1971.

Libby, P., Ridker, P. M. and Hansson, G. K. (2011), 'Progress and challenges in translating the biology of atherosclerosis', *Nature* **473**(7347), 317–325.

Lim, C., Zhou, E. and Quek, S. (2006), 'Mechanical models for living cells—a review', *J Biomech* **39**(2), 195–216.

Liu, S., Yen, M. and Fung, Y. (1994), 'On measuring the third dimension of cultured endothelial cells in shear flow', *Proc Natl Acad Sci* **91**(19), 8782–8786.

Lo, C.-M., Wang, H.-B., Dembo, M. and Wang, Y.-l. (2000), 'Cell movement is guided by the rigidity of the substrate', *Biophys J* **79**(1), 144–152.

Lu, L., Oswald, S. J., Ngu, H. and Yin, F. C.-P. (2008), 'Mechanical properties of actin stress fibers in living cells', *Biophys J* **95**(12), 6060–6071.

Lucitti, J. L., Jones, E. A., Huang, C., Chen, J., Fraser, S. E. and Dickinson, M. E. (2007), 'Vascular remodeling of the mouse yolk sac requires hemodynamic force', *Development* **134**(18), 3317–3326.

Lum, R. M., Wiley, L. M. and Barakat, A. (2000), 'Influence of different forms of fluid shear stress on vascular endothelial tgf-beta1 mrna expression.', *International journal of molecular medicine* **5**(6), 635–641.

Malek, A. M., Alper, S. L. and Izumo, S. (1999), 'Hemodynamic shear stress and its role in atherosclerosis', *J Am Med Assoc* **282**(21), 2035–2042.

Martinac, B. (2012), 'Mechanosensitive ion channels', *Channels* **6**(4), 211–213.

Méléard, S. (2010), *Aléatoire: Introduction à la théorie et au calcul des probabilités*, Editions Ecole Polytechnique.

Millán, J., Cain, R. J., Reglero-Real, N., Bigarella, C., Marcos-Ramiro, B., Fernández-Martín, L., Correas, I. and Ridley, A. J. (2010), 'Adherens junctions connect stress fibres between adjacent endothelial cells', *BMC Biol* **8**(1), 11.

Moore, S. W., Roca-Cusachs, P. and Sheetz, M. P. (2010), 'Stretchy proteins on stretchy substrates: the important elements of integrin-mediated rigidity sensing', *Dev cell* **19**(2), 194–206.

Na, S., Collin, O., Chowdhury, F., Tay, B., Ouyang, M., Wang, Y. and Wang, N. (2008), 'Rapid signal transduction in living cells is a unique feature of mechanotransduction', *Proc Natl Acad Sci* **105**(18), 6626–6631.

Orr, A. W., Helmke, B. P., Blackman, B. R. and Schwartz, M. A. (2006), 'Mechanisms of mechanotransduction', *Dev Cell* **10**(1), 11–20.

Patwari, P. and Lee, R. T. (2008), 'Mechanical control of tissue morphogenesis', *Circ Res* **103**(3), 234–243.

Pedersen, J. A. and Swartz, M. A. (2005), 'Mechanobiology in the third dimension', *Ann Biomed Eng* **33**(11), 1469–1490.

Pelham, R. J. and Wang, Y.-l. (1997), 'Cell locomotion and focal adhesions are regulated by substrate flexibility', *Proc Natl Acad Sci* **94**(25), 13661–13665.

Petrie, R. J., Doyle, A. D. and Yamada, K. M. (2009), 'Random versus directionally persistent cell migration', *Nat Rev Mol Cell Biol* **10**(8), 538–549.

Plow, E. F., Haas, T. A., Zhang, L., Loftus, J. and Smith, J. W. (2000), 'Ligand binding to integrins', *J Biol Chem* **275**(29), 21785–21788.

Reinhart-King, C. A., Dembo, M. and Hammer, D. A. (2008), 'Cell-cell mechanical communication through compliant substrates', *Biophys J* **95**(12), 6044–6051.

Ricca, B. L., Venugopalan, G. and Fletcher, D. A. (2013), 'To pull or be pulled: parsing the multiple modes of mechanotransduction', *Curr Opin Cell Biol* **25**(5), 558–564.

Ridley, A. J., Schwartz, M. A., Burridge, K., Firtel, R. A., Ginsberg, M. H., Borisy, G., Parsons, J. T. and Horwitz, A. R. (2003), 'Cell migration: integrating signals from front to back', *Science* **302**(5651), 1704–1709.

Risau, W. and Flamme, I. (1995), 'Vasculogenesis', *Annu Rev Cell Dev Biol* **11**(1), 73–91.

Roan, E. and Waters, C. M. (2011), 'What do we know about mechanical strain in lung alveoli?', *Am J Physiol-Lung C* **301**(5), L625–L635.

Sawada, Y. and Sheetz, M. P. (2002), 'Force transduction by triton cytoskeletons', *J Cell Biol* **156**(4), 609–615.

Sawada, Y., Tamada, M., Dubin-Thaler, B. J., Cherniavskaya, O., Sakai, R., Tanaka, S. and Sheetz, M. P. (2006), 'Force sensing by mechanical extension of the src family kinase substrate p130cas', *Cell* **127**(5), 1015–1026.

Schiller, H. B. and Fässler, R. (2013), 'Mechanosensitivity and compositional dynamics of cell–matrix adhesions', *EMBO Rep* **14**(6), 509–519.

Schwarz, U. S., Erdmann, T. and Bischofs, I. B. (2006), 'Focal adhesions as mechanosensors: the two-spring model', *Biosystems* **83**(2), 225–232.

Shamloo, A., Ma, N., Poo, M.-m., Sohn, L. L. and Heilshorn, S. C. (2008), 'Endothelial cell polarization and chemotaxis in a microfluidic device', *Lab Chip* **8**(8), 1292–1299.

Shyy, J. Y.-J. and Chien, S. (2002), 'Role of integrins in endothelial mechanosensing of shear stress', *Circ Res* **91**(9), 769–775.

Sieminski, A., Hebbel, R. P. and Gooch, K. J. (2004), 'The relative magnitudes of endothelial force generation and matrix stiffness modulate capillary morphogenesis in vitro', *Exp Cell Res* **297**(2), 574–584.

Smith, M. A., Blankman, E., Gardel, M. L., Luettjohann, L., Waterman, C. M. and Beckerle, M. C. (2010), 'A zyxin-mediated mechanism for actin stress fiber maintenance and repair', *Dev cell* **19**(3), 365–376.

Song, J. W. and Munn, L. L. (2011), 'Fluid forces control endothelial sprouting', *Proc Natl Academy of Sciences* **108**(37), 15342–15347.

Spencer, A. J. M. et al. (1984), *Continuum theory of the mechanics of fibre-reinforced composites*, Vol. 282, Springer.

Sukharev, S., Betanzos, M., Chiang, C.-S. and Guy, H. R. (2001), 'The gating mechanism of the large mechanosensitive channel mscl', *Nature* **409**(6821), 720–724.

Tagawa, H., Wang, N., Narishige, T., Ingber, D. E., Zile, M. R. and Cooper, G. (1997), 'Cytoskeletal mechanics in pressure-overload cardiac hypertrophy', *Circ Res* **80**(2), 281–289.

Tamada, M., Sheetz, M. P. and Sawada, Y. (2004), 'Activation of a signaling cascade by cytoskeleton stretch', *Dev Cell* **7**(5), 709–718.

Tambe, D. T., Hardin, C. C., Angelini, T. E., Rajendran, K., Park, C. Y., Serra-Picamal, X., Zhou, E. H., Zaman, M. H., Butler, J. P., Weitz, D. A. et al. (2011), 'Collective cell guidance by cooperative intercellular forces', *Nat Mat* **10**(6), 469–475.

Tarbell, J. M. and Pahakis, M. (2006), 'Mechanotransduction and the glycocalyx', *J Intern Med* **259**(4), 339–350.

Tzima, E., Irani-Tehrani, M., Kiosses, W. B., Dejana, E., Schultz, D. A., Engelhardt, B., Cao, G., DeLisser, H. and Schwartz, M. A. (2005), 'A mechanosensory complex that mediates the endothelial cell response to fluid shear stress', *Nature* **437**(7057), 426–431.

Vogel, V. (2006), 'Mechanotransduction involving multimodular proteins: converting force into biochemical signals', *Annu Rev Biophys Biomol Struct* **35**, 459–488.

Wang, N. and Ingber, D. E. (1994), 'Control of cytoskeletal mechanics by extracellular matrix, cell shape, and mechanical tension', *Biophys J* **66**(6), 2181–2189.

Wang, N., Tolić-Nørrelykke, I. M., Chen, J., Mijailovich, S. M., Butler, J. P., Fredberg, J. J. and Stamenović, D. (2002), 'Cell prestress. i. stiffness and prestress are closely associated in adherent contractile cells', *Am J Physiol-Cell Physiol* **282**(3), C606–C616.

Wang, N., Tytell, J. D. and Ingber, D. E. (2009), 'Mechanotransduction at a distance: mechanically coupling the extracellular matrix with the nucleus', *Nat Rev Mol Cell Biol* **10**(1), 75–82.

Wang, Y., Botvinick, E. L., Zhao, Y., Berns, M. W., Usami, S., Tsien, R. Y. and Chien, S. (2005), 'Visualizing the mechanical activation of src', *Nature* **434**(7036), 1040–1045.

Weiss, J. A., Maker, B. N. and Govindjee, S. (1996), 'Finite element implementation of incompressible, transversely isotropic hyperelasticity', *Comput Method Appl Mech Eng* **135**(1), 107–128.

Whisler, J. A., Chen, M. B. and Kamm, R. D. (2012), 'Control of perfusable microvascular network morphology using a multiculture microfluidic system', *Tissue Eng Part C: Methods* .

Wirtz, H. R. and Dobbs, L. G. (2000), 'The effects of mechanical forces on lung functions', *Respir Physiol* **119**(1), 1–17.

Wolfenson, H., Bershadsky, A., Henis, Y. I. and Geiger, B. (2011), 'Actomyosin-generated tension controls the molecular kinetics of focal adhesions', *J Cell Sci* **124**(9), 1425–1432.

Wolff, J., Maquet, P. and Furlong, R. (1986), *The law of bone remodelling*, Springer-Verlag Berlin.

Wong, A. J., Pollard, T. D. and Herman, I. M. (1983), 'Actin filament stress fibers in vascular endothelial cells in vivo', *Science* **219**(4586), 867–869.

Yeung, T., Georges, P. C., Flanagan, L. A., Marg, B., Ortiz, M., Funaki, M., Zahir, N., Ming, W., Weaver, V. and Janmey, P. A. (2005), 'Effects of substrate stiffness on cell morphology, cytoskeletal structure, and adhesion', *Cell Motil Cytoskel* **60**(1), 24–34.

Yonemura, S., Wada, Y., Watanabe, T., Nagafuchi, A. and Shibata, M. (2010), 'α-catenin as a tension transducer that induces adherens junction development', *Nat Cell Biol* **12**(6), 533–542.

Yoshigi, M., Hoffman, L. M., Jensen, C. C., Yost, H. J. and Beckerle, M. C. (2005), 'Mechanical force mobilizes zyxin from focal adhesions to actin filaments and regulates cytoskeletal reinforcement', *J Cell Biol* **171**(2), 209–215.

Zaman, M. H., Trapani, L. M., Sieminski, A. L., MacKellar, D., Gong, H., Kamm, R. D., Wells, A., Lauffenburger, D. A. and Matsudaira, P. (2006), 'Migration of tumor cells in 3d matrices is governed by matrix stiffness along with cell-matrix adhesion and proteolysis', *Proc Natl Acad Sci* **103**(29), 10889–10894.